

©2018

HAIDER ADEL ABDULHAMEED

ALL RIGHTS RESERVED

**EXPERIMENTAL AND ANALYTICAL STUDY OF FIBER-
REINFORCED SELF-CONSOLIDATING CONCRETE AS A
REPAIR MATERIAL**

By

HAIDER ADEL ABDULHAMEED

A dissertation submitted to the

School of Graduate Studies

Rutgers, The State University of New Jersey

In partial fulfillment of the requirements

For the degree of

Doctor of Philosophy

Graduate Program in Civil and Environmental Engineering

Written under the direction of

Dr. Hani H. Nassif, P.E.

And approved by

New Brunswick, New Jersey

January, 2018

ABSTRACT OF THE DISSERTATION

EXPERIMENTAL AND ANALYTICAL STUDY OF FIBER-REINFORCED SELF-CONSOLIDATING CONCRETE AS A REPAIR MATERIAL

By HAIDER ADEL ABDULHAMEED

Dissertation Director:

Dr. Hani H. Nassif

Self-consolidating concrete (SCC) has been used for repairs due to its ability in overhead applications and hard to access areas such as condensed reinforcement. However, due to its high content in cementitious and supplementary materials, SCC is subjected to shrinkage cracking. To overcome this aspect, fibers were used in the SCC mixtures to form what is known as fiber-reinforced self-consolidating concrete (FR-SCC).

Experimental and analytical programs were carried out to investigate the use of the FR-SCC as a repair material. The experimental program included the flexural behavior of 10 beam specimens made of FR-SCC using different volume fractions of two types of supplementary cementitious materials (silica fume (SF) and slag (SL)) and two types of fibers (steel fiber (STF) and polypropylene fiber (PPF)). The main reinforcement for the control beams consisted of #5 reinforcing bars, while the main reinforcement for the repaired beams was either #4 or #3 reinforcing bars that were introduced to simulate 35 % and 65 % loss in rebar areas due to corrosion, respectively. The goal of the repair scheme is focused on extending the service life of the structural elements for about 5-10 years. The

analytical part of this research included the development and validation of a finite element model (FEM) that can be used for the analysis and prediction of the structural behavior at various load points. Additionally, results from the experimental program were compared with predictions of the structural properties of all the beams using various code provisions.

Results from tests on the fresh and hardened mechanical properties demonstrated that the optimized FR-SCC mixtures were efficient repair materials and can develop adequate bond strength to existing concrete. The flexural test results showed that the repaired beams have higher cracking capacities compared with the control beams. A maximum percentage increase of 29 % was achieved for the beam repaired with 10SF50S compared to the average cracking load for the two control beams. This demonstrated that the repair material markedly improves the repaired area properties, especially the tensile strength. Such improvement is vital in extending the life of the repaired structure under the service loads. The ACI 318, CSA A23.3, and AASHTO-LRFD were non-conservative in estimating the cracking load as well as the deflection in both control and repaired beams, while the ACI 544 equations were conservative and provided a safe prediction for both cracking and ultimate loads. The developed finite element models (FEMs) were effective in producing good prediction in the elastic and plastic ranges of the applied load but did not produce the ultimate deflections (i.e., ductility) exhibited during the tests. Nonetheless, FEM could be used as a tool to further investigate the behavior of repaired and unrepaired concrete beams under static loading.

DEDICATION

*This Humble Work
is Dedicated to my
Beloved Family.*

Haider

ACKNOWLEDGEMENTS

I would like to express my cordial thanks and deepest gratitude to my advisor Dr. Hani H. Nassif for his help and kind attention to complete this work. It was an honor to work with him and be exposed to his engineering and life experience.

I would also like to thank Dr. Thomas Tsakalakos and Dr. Hao Wang for being on my committee and for their valuable advice. I would also like to thank Dr. Husam S. Najm for being on my committee as well as his guidance as a graduate director.

Deepest thanks are expressed to my mother, my brother, my wife, and my kids for their love and support at all times.

My sincere thanks to the Higher Committee for Education Development in Iraq (HCED) prime minister office for awarding my Ph.D. scholarship.

I would also like to thank Dr. Chaekuk Na for his efforts on the coordination of the project. Also, my thanks extended to Dr. Adi Abu-Obeidah and Mr. Andrew Wassef for their coordination in lab work, and to my colleagues Abdulemam Abu-Saibia and Michael Salvador for their help and support.

Thanks to undergraduate student research assistances, Greg Brewer, Giuseppe Liberti, Dalexander Gonzales, Sean Kwiatec, Justinian Grant, Dominic, Francis Casimiro, and Zaina Hamdan for their assistance with the testing and tasks needed to complete the experimental work for the whole project.

I would also like to thank the laboratory manager Edward Wass for his help with the experimental work.

I would like also to thank Clayton Concrete, Euclid Chemical, and LaFarge North America for donating materials towards the completion of this study.

Special thanks to the RE-CAST Tier 1 University Transportation Center and its director, Dr. Kamal H. Khayat, for initiating and funding this joint research project and for his technical advice and input throughout the project duration.

Finally, my thanks are extended to all who encouraged me even with one kind word.

TABLE OF CONTENTS

ABSTRACT OF THE DISSERTATION	<i>ii</i>
DEDICATION	<i>iv</i>
ACKNOWLEDGEMENTS.....	<i>v</i>
TABLE OF CONTENTS.....	<i>vii</i>
LIST OF TABLES	<i>x</i>
LIST OF FIGURES.....	<i>xi</i>
Chapter 1 INTRODUCTION.....	<i>1</i>
1.1 BACKGROUND	1
1.2 PROBLEM STATEMENT	3
1.3 OBJECTIVES	4
1.4 DISSERTATION ORGANIZATION	5
Chapter 2 DETERIORATION AND REPAIR OF CONCRETE.....	<i>7</i>
2.1 INTRODUCTION	7
2.2 CAUSES AND TYPES OF DETERIORATION OF CONCRETE.....	7
2.2.1 Corrosion of Reinforcement	8
2.2.2 Chemical Attack.....	9
2.2.3 Freeze/Thaw.....	11
2.2.4 Fire/Heat	13
2.2.5 Abrasion/Erosion	14
2.2.6 Overload or Under Design	15
2.2.7 Aggregate Reactivity	15
2.2.8 Volume Changes	16
2.3 SELECTING AND TESTING OF REPAIR MATERIALS	17
2.4 TYPES OF REPAIR MATERIALS	23
2.5 WHY SCC AND FR-SCC AS A REPAIR MATERIAL?	26
Chapter 3 EXPERIMENTAL SETUP	<i>34</i>
3.1 INTRODUCTION	34
3.2 MATERIALS.....	37
3.2.1 Cement	37
3.2.2 Aggregate.....	38
3.2.3 Silica Fume	39
3.2.4 Slag 120	39
3.2.5 Fibers.....	41
3.2.6 High Range Water Reducing Admixture.....	42
3.2.7 Air Entraining Admixture.....	43
3.3 MIXING PROCEDURE AND MIX PROPORTIONS	43
3.4 TESTING OF FRESH CONCRETE	44

3.4.1	Slump Flow Test	44
3.4.2	J-Ring.....	45
3.4.3	Modified L-box	46
3.4.4	Air Content.....	47
3.5	TESTING OF HARDENED CONCRETE.....	48
3.5.1	Compressive Strength Test	48
3.5.2	Splitting Tensile Strength Test.....	48
3.5.3	Flexural Strength Test.....	49
3.5.4	Static Modulus of Elasticity Test.....	50
3.5.5	Length Change (Free Shrinkage) Test	51
3.6	COMPATIBILITY AND BOND STRENGTH TESTS	52
3.6.1	Third Point Loading Compatibility Test.....	54
3.6.2	Bond Strength Test	56
3.7	FLEXURAL STRENGTH TEST FOR FULL-SCALE BEAMS.....	57
3.7.1	Preparing the Beams	57
3.7.2	Casting and Curing of the Substrate	58
3.7.3	Repairing and Curing.....	62
3.7.4	Beam Flexural Tests Setup	64
Chapter 4 EXPERIMENTAL RESULTS		72
4.1	INTRODUCTION	72
4.2	FRESH CONCRETE RESULTS.....	72
4.3	HARDENED CONCRETE RESULTS	74
4.3.1	Compressive strength.....	74
4.3.2	Splitting Tensile Strength	76
4.3.3	Flexural Strength.....	78
4.3.4	Modulus of Elasticity	79
4.3.5	Free Shrinkage	82
4.3.6	Compatibility Test Results.....	82
4.3.7	Bond Strength Results.....	85
4.4	FLEXURAL TEST RESULTS FOR FULL-SCALE BEAMS	88
4.4.1	Cracking and Ultimate Loads	90
4.4.2	Load – Deflection Relationship	91
4.4.3	Load – Strain Relationship.....	93
4.4.4	Mode of Failure and Cracking Behavior	95
4.4.5	Neutral Axis	102
Chapter 5 FINITE ELEMENT MODELING AND CODE PREDICTIONS.....		108
5.1	INTRODUCTION	108
5.2	CODE EQUATIONS.....	109
5.2.1	Prediction of Cracking Load.....	109
5.2.2	Prediction of Ultimate Load.....	117
5.2.3	Prediction of Deflection.....	121
5.3	FINITE ELEMENT APPROACH.....	125

5.3.1	General	125
5.3.2	Building the Finite Element Model.....	126
5.3.3	Results and Model Validation.....	137
5.4	PARAMETRIC STUDY	151
5.4.1	Introduction.....	151
5.4.2	Main Steel Reinforcement (A_s)	152
5.4.3	Thickness of the Repair Layer (hr)	152
5.4.4	Concrete Compressive Strength for the Repair Layer (f'_{cr})	153
5.4.5	Main Steel Reinforcement Depth (d).....	153
5.5	SUMMARY	157
5.5.1	Code Predictions	157
5.5.2	Finite Element Model and the Parametric study.....	157
Chapter 6 CONCLUSIONS.....		159
REFERENCES		162

LIST OF TABLES

Table 2.1 Categories of Repair Materials	23
Table 2.2 Summary of the Properties of SCC used in Repairing the Parking Garage in Quebec	29
Table 3.1 Proposed Mixtures and their Abbreviations	35
Table 3.2 Chemical Composition and Physical Properties of the Cement*	37
Table 3.3 Grading of the Aggregate Used	38
Table 3.4 Silica Fume Properties*	40
Table 3.5 Chemical and Physical Properties of Slag 120*	41
Table 3.6 Technical information of PSI Crimped Steel Fiber*	42
Table 3.7 Technical information of PSI Fiberstrand 100*	42
Table 3.8 Mix Proportions for One Cubic Yard of SCC and FR-SCC Mixtures	44
Table 3.9 Mixture Design for the Substrate.....	53
Table 3.10 Class A Concrete Strength Results (Average of Three samples)	54
Table 3.11 Selected Mixtures and Number of Samples for Compatibility and Bond Tests	54
Table 4.1 Fresh Concrete Test Results	73
Table 4.2 Compressive Strength at Different Ages	75
Table 4.3 Splitting Tensile Strength at Different Ages.....	77
Table 4.4 Flexural Strength at Different Ages.....	79
Table 4.5 Modulus of Elasticity at Different Ages	81
Table 4.6 Results of Third Point Loading Composite Prism Test and Failure Location..	84
Table 4.7 Results of Slant Shear, Bond Strength Test.....	87
Table 4.8 Cracking and Ultimate Loads for the Tested Beams	91
Table 4.9 Number of Cracks and Average Crack spacing for the Tested Beams in the Constant Moment Zone.....	97
Table 5.1 Results of Predicted Cracking Load by ACI 318, CSA A23.3, AASHTO-LRFD, and ACI 544 Codes	113
Table 5.2 Results of the Statistical Analysis of the Predicted Cracking Load by ACI 318 Code	116
Table 5.3 Results of the Statistical Analysis of the Predicted Cracking Load by AASHTO-LRFD Code	116
Table 5.4 Results of the Statistical Analysis of the Predicted Cracking Load by CSA A23.3 Code	117
Table 5.5 Results of the Statistical Analysis of the Predicted Cracking Load by ACI 544 Code	117
Table 5.6 Results of Predicted Ultimate Load	120
Table 5.7 Results of Predicted Deflection for the Three Different Codes.....	124
Table 5.8 Parameters Used in the Plastic Damage Model	134
Table 5.9 Properties and Results of the Studied Beams	154

LIST OF FIGURES

Figure 1.1 Flow Chart of the Research	5
Figure 2.1 Steel Reinforcement Corrosion in a Reinforced Concrete Wall [Khayat, 2006]	9
Figure 2.2 Freezing and Thawing Deterioration to the Downstream Face of a Concrete Dam [http://civildigital.com]	13
Figure 2.3 Cracking of Concrete from ASR [Kosmatka and Panarese, 2002]	16
Figure 2.4 Flowchart Illustrating the Selection Process for a Repair Material [Emmons, 1993]	18
Figure 2.5 Compatibility Test and evaluation: 1,2-compatibility; 3,4,5-incompatibility (a) Specimen arrangement; (b) Third point loading beam test [Czarneck et al 1999].	20
Figure 2.6 Effects of Mismatching Elastic Moduli (a) Load parallel to interface	21
Figure 2.7 Pull off Test Instrument [Pattnaik, 2006]	22
Figure 2.8 Failures Modes of the Composite Slant Shear Test [Pattnaik, 2006]	23
Figure 2.9 The Behavior of Single and Multiple Cracking of the Specimens under Uniaxial Loading [Vandewalle, 2002]	28
Figure 3.1 Flow Chart for the Initial Material Testing	36
Figure 3.2 Particle Size Distribution Curve for the Aggregate Used	39
Figure 3.3 Types of Fibers Used	41
Figure 3.4 Slump Flow Test	45
Figure 3.5 J-Ring Test Setup with Inverted Cone	46
Figure 3.6 J-Ring Flow	46
Figure 3.7 Modified L-box Test	47
Figure 3.8 Vertical Air Chamber	47
Figure 3.9 1-Million lbs. Forney Testing Machine	48
Figure 3.10 Splitting Tensile Test Setup	49
Figure 3.11 Flexural Strength Test Setup.	50
Figure 3.12 Static Modulus of Elasticity Test Setup	51
Figure 3.13 Length Change Test Setup	52
Figure 3.14 Third Point Loading Compatibility Test	55
Figure 3.15 Test Setup for Compatibility Test	55
Figure 3.16 Slant Shear Bond Strength Test	56
Figure 3.17 Making the Wood Forms and Reinforcement Cages	57
Figure 3.18 Installed Strain Gauges	58
Figure 3.19 Covering the Rebars with Duct Tape Protected by M-COAT J	58
Figure 3.20 Casting the Substrate for the Eight Beams and the Two Control Beams	59
Figure 3.21 Applying the Surface Retarder	60
Figure 3.22 Stream Water for Surface Roughness to Expose the Aggregate to Ensure a Good Bond of the Substrate with the Repair Material	60
Figure 3.23 Removing the Duct Tape	61
Figure 3.24 Curing of the Substrate	61
Figure 3.25 Cleaning the Rebars from any Rust	62
Figure 3.26 Curing the Repaired Beam	63

Figure 3.27 Painting the Beam with Whitewash	63
Figure 3.28 Installing the Setup	64
Figure 3.29 Test Setup and Instrument Locations	65
Figure 3.30 LVDT Installed to Measure Crack Width	65
Figure 3.31 LVDT Type DCTH1000A (left) and DCTH400AG (right).....	67
Figure 3.32 LVDT at the Top for Measuring the Compressive Strain	68
Figure 3.33 VWSG and the LVDT for Deboning Measurement.....	68
Figure 3.34 Geokon Model 4000 VWSG Used for Deboning Measurement.....	69
Figure 3.35 Concrete Strain Gauges	69
Figure 3.36 Vishay 120 Ohm Foil Strain Gauge C2A-06-20CLW-120 (left) and C2A-06-125LW-120 (right).....	70
Figure 3.37 LVDTs Setup.....	70
Figure 3.38 CR3000 Micrologger Used.....	71
Figure 4.1 Compressive Strength at Different Ages	74
Figure 4.2 Splitting Tensile Strength at Different Age.....	76
Figure 4.3 Flexural Strength at Different Ages	78
Figure 4.4 Modulus of Elasticity at Different Ages.....	80
Figure 4.5 Modulus of Elasticity vs Concrete Strength.....	80
Figure 4.6 Free Drying Shrinkage Behavior for Various Mixtures	82
Figure 4.7 Results of Third Point Loading Composite Prism Test.....	83
Figure 4.8 Compatibility Test Failure Mode Observed.....	85
Figure 4.9 Results of Slant Shear, Bond strength Test.	86
Figure 4.10 Example of the Failure in both Substrate and Repair Material	88
Figure 4.11 Beams Cross Section Design Details and the Corresponding Mixtures Selected for Repairing:	89
Figure 4.12 Deflection at Midspan for all the Beams	93
Figure 4.13 Measuring the Deflection at Midspan after Removing the LVDTs	93
Figure 4.14 Relationship between applied Load and both Rebar Tensile Strain and Concrete Compressive strain for all Beams	94
Figure 4.15 Picture Taken Using Digital Magnifier Camera at 70x Magnification Showing Major Crack at Midspan in 35SL20P Repaired Beam at Failure	98
Figure 4.16 Crack at Failure in 10SF50S Repaired Beam.....	98
Figure 4.17 Mode of Failure of Beam Specimens	99
Figure 4.18 Crack Patterns and Width at Failure for all the Beams	101
Figure 4.18 Location of Strain Gauges and LVDT Used to Determine the NA.....	102
Figure 4.19 Concrete Strain Profile at the Section of Maximum Moment at Various Load Levels for Control Beam Contains #5 Rebars ($A_s = 0.93 \text{ in}^2$).....	103
Figure 4.20 Concrete Strain Profile at the Section of Maximum Moment at Various Load Levels for Repaired Beams Contain #4 Rebars ($A_s = 0.6 \text{ in}^2$)	105
Figure 4.21 Concrete Strain Profile at the Section of Maximum Moment at Various Load Levels for Repaired Beams Contain #3 Rebars ($A_s = 0.33 \text{ in}^2$)	107
Figure 5.1 Analytical Investigation Diagram.....	109
Figure 5.2 Comparison of Prediction of Cracking Load Using ACI 318 [2014] with the Experimental Results	114

Figure 5.3 Comparison of Prediction of Cracking Load Using CSA A23.3 [2004] with the Experimental Results	114
Figure 5.4 Comparison of Prediction of Cracking Load Using AASHTO-LRFD [2012] with the Experimental Results	115
Figure 5.5 Comparison of Prediction of Cracking Load Using ACI 544 [2011] with the Experimental Results	115
Figure 5.6 Stress and strain variation in FRC [Henager et al., 1976]	118
Figure 5.7 Comparison of Prediction of Ultimate Load Using ACI 544 [2011] with the Experimental Results	120
Figure 5.8 Loading Setup Used	121
Figure 5.9 An Example of the Correlation between the Predicted Load-deflection for the Studied Code with Experimental for a Repaired Beam	125
Figure 5.10 Finite Element Model of a Half Concrete Beam: a) Control Beam, b) Repaired Beam	127
Figure 5.11 Details of the Incrementation limits	128
Figure 5.12 Types of Element Used	129
Figure 5.13 Response of concrete to uniaxial loading in tension (a) and (b) compression [ABAQUS, 2011]	130
Figure 5.14 Post-failure Stresses Relationship: a) Post-failure Stress-displacement Curve; b) Post-failure Stress-fracture Energy Curve [ABAQUS, 2011]	132
Figure 5.15 Yield Surface in Plane Stress [ABAQUS, 2014]	133
Figure 5.16 Stress- Strain for Concrete in Compression	135
Figure 5.17 Stress- Strain for Concrete in Tension	135
Figure 5.18 Stress-Stain for Steel: a) Stress-Strain; b) Stress-Plastic Strain	136
Figure 5.19 Applied Load and Deflection Relationship for the Repaired Beams Contain #4 Rebars ($A_s = 0.6 \text{ in}^2$): Comparison between FEM and Experimental Results	139
Figure 5.20 Applied Load and Deflection Relationship for the Repaired Beams Contain #3 Rebars ($A_s = 0.33 \text{ in}^2$): Comparison between FEM and Experimental Results	141
Figure 5.21 Applied Load and Rebar Tension Strain Relationship at Middle at Center for the Repaired Beams Contain #4 Rebars ($A_s = 0.6 \text{ in}^2$): Comparison between FEM and Experimental Results	143
Figure 5.22 Applied Load and Rebar Tension Strain Relationship at Middle at Center for the Repaired Beams Contain #3 Rebars ($A_s = 0.33 \text{ in}^2$): Comparison between FEM and Experimental Results	145
Figure 5.23 Applied Load and Rebar Tension Strain Relationship at Middle at Center for Control Beam Contains #5 Rebars ($A_s = 0.93 \text{ in}^2$): Comparison between FEM and Experimental Results	146
Figure 5.24 Applied Load and Deflection Relationship for the Control Beams: Comparison between FEM and Experimental Results	146
Figure 5.25 Applied Load and Deflection Relationship: Comparison between the Best Performing Beams and the Corresponding Control One	147
Figure 5.26 Nodal Displacement (Deflection) in Y-Direction (U_y)	151
Figure 5.27 Flowchart for the Parametric Study	152
Figure 5.28 Effect of Variation of (A_s) on Cracking and Ultimate Loads	155

Figure 5.29 Effect of Variation of (h_r) on Cracking and Ultimate Loads	155
Figure 5.30 Effect of Variation of (f'_{cr}) on Cracking and Ultimate Loads.....	156
Figure 5.31 Effect of Variation of (d) on Cracking and Ultimate Loads.....	156

CHAPTER 1 INTRODUCTION

1.1 Background

When concrete was first introduced, it was hailed as a long-term and maintenance-free construction material. Structural repairs for concrete structures were never considered. With the appropriate design of the concrete, taking into account the exposure, mix design, and pre-service testing, an extended lifetime for reinforced concrete structures can be enjoyed. Reinforced concrete has shown to not be as maintenance free as once thought, and early deterioration or even failure is known to occur.

Deterioration of concrete usually leads to a decrease in performance. This leads to the understanding that engineering structures do not perform at the same level for their entire lifespan. This natural behavior is usually forgotten or not given that much attention by designers. In addition, standards for structural members have a limited set of guidelines to ensure durability at the same level during the whole service life. The poor durability designs and with the lack of periodic maintenance and repair can very easily result in expensive maintenance and even failure of the structure combined with human catastrophe.

Many infrastructures in the United States show advanced stages of deterioration. Corrosion of reinforcement or frost attack is the most common deterioration failure for exposed structures. In some environments, concrete may suffer from chemical attack by acids, sulfates, and even soft water. Another failure method occurs when concrete constituents absorb water and react or freeze which usually leads to disintegration or expansion.

Repairs should increase the lifetime of a structure by having at least the same mechanical and durability properties as the original. Repair is used to avoid or postpone demolition and reconstruction for economic purposes. Emmons [2006] found that repair, strengthening, and protection cost of concrete structures in the United States was estimated to be \$18 to \$20 billion. It is estimated in 2017 by the American Society of Civil Engineers (ASCE) report card that \$4.59 trillion would be needed by the 2025 to upgrade the infrastructure condition in the United States from Grade D (Poor) to Grade B (Good) [ASCE, 2017]. Therefore, these repairs need to be of high quality, better durability, and efficient to avoid future repairs again.

The efficiency of repair depends on both the repair material quality and the ability of the material to fill the section to be repaired and must cover the reinforcement. Repair efficiency is also a function of repair method, compatibility, and the bond between the repair material and the substrate, and the ability of repair material to entirely fill the repairing zone, especially in congested reinforcement areas. Hence, to fulfill these requirements, a repair material should be carefully selected to ensure a good repair.

The function and performance of a building, a bridge, or pavement can be improved by ensuring a good repair. However, a poor repair fails early or deteriorates the repaired concrete structure in a relatively short period. Poston et al. [2000] have shown that the choice of appropriate repair material is crucial on material properties and the composite repaired section behavior under service exposure conditions.

Present trends include the use of pozzolanic materials such as fly ash, metakaolin, slag, silica fume, and fine limestone etc. as a partial replacement of cement in concrete to lower the consumption of clinkers and also increase durability. Scrivener [2003] has

pointed out that the presence of reactive silica increases the production of strätlingite, which in controlled quantities, comes with a benefit to the minimum stable strength. Scrivener [2003] has also pointed that larger amounts added in a mix can feasibly eliminate strength regression completely, but with having a significant decrease in initial strength. Evidence does exist that shows that this research could advance rheology and permit the formulation of Self Consolidating Concrete (SCC).

1.2 Problem Statement

SCC is especially preferred for the rehabilitation and repair of reinforced concrete structures. The repair mortar or concrete applied to existing concrete is usually hard to consolidate, and in most cases, vibration is not feasible. From this point of view, the self-consolidation of repair mortar or concrete may bring considerable advantages to narrow mold systems. SCC mixtures can be designed to provide the required hardened concrete properties for an application, similar to regular concrete. If the SCC mixture is designed to have a higher paste content or fines compared to conventional concrete, an increase in shrinkage may occur. The use of fiber reinforcement in SCC enhances its tensile strength and delays the onset of tension cracks due to the heat of hydration since it contains a high percentage of fines. The studies conducted by Abdul-Hameed [2010] Hassan et al. [2010], Mansi [2010], and Pattnaik [2006] have shown that the failure of concrete repairs is mainly due to improper selection of repair material without investigating compatibility between repair material and substrate concrete. Thus, specific tests such as compatibility and bond strength between the repair material and the substrate (concrete to be repaired) were used in this research.

1.3 Objectives

The main objective of this study is to investigate the use of the fiber reinforced self-consolidating concrete (FR-SCC) for infrastructure repair and construction. This will be achieved by examining fresh and hardened properties of SCC and FR-SCC mixtures.

The second objective is to examine the bond strength and compatibility of FR-SCC as a repair material with the substrate and select the mixtures that yield the best performance.

The third objective is to study the structural behavior of full-scale repaired beams that have corrosion and concrete cover lost simulated. The effect of various parameters on the flexural behavior, such as the area of the main steel reinforcement to simulate corrosion, pozzolanic material type, fiber type, fiber volume fraction will be studied.

The fourth objective is to verify code provisions with the experimental results. In addition, develop a finite element model (FEM) that validate the tested beams' results.

Figure 1.1 shows the designed analytical and experimental programs in order to achieve the objectives above.

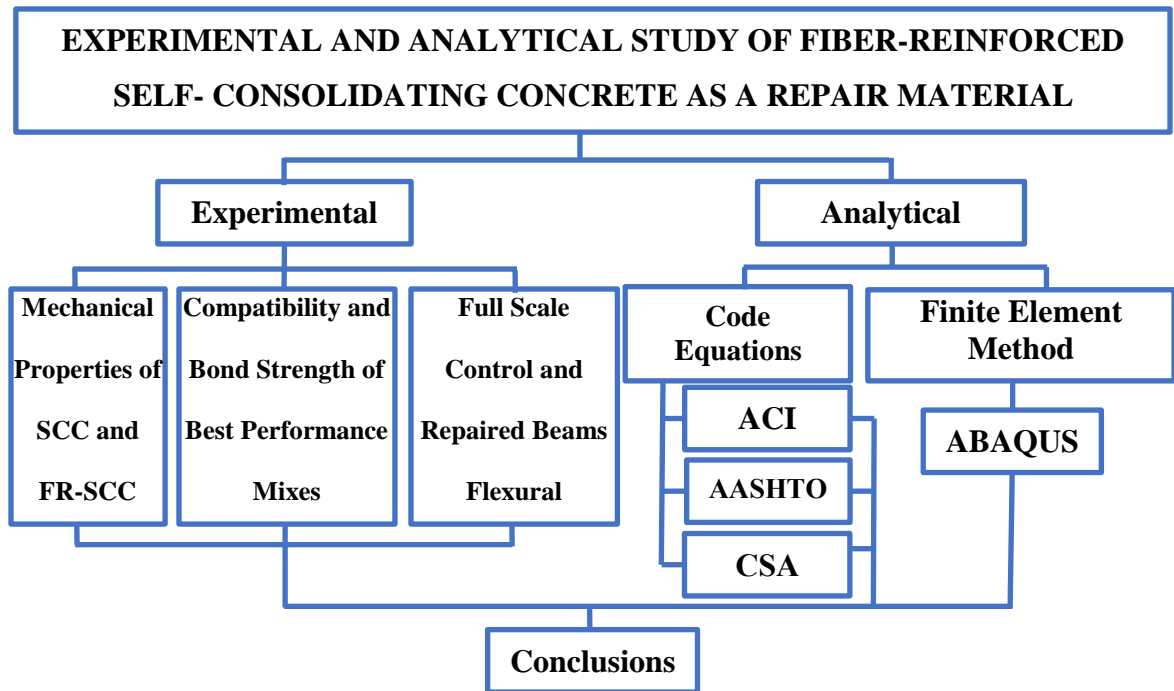


Figure 1.1 Flow Chart of the Research

1.4 Dissertation Organization

The research work presented in this dissertation is given throughout six chapters: Chapter 1 covers the introduction consisting of the background, research objectives, and dissertation organization.

Chapter 2 presents a general background. That includes the causes and types of deterioration of concrete, selecting and testing of repair materials, types of repair materials, and why SCC and FR-SCC as a repair material. Finally, concluding remarks and research needs.

Chapter 3 covers the details of the experimental program. This include types and properties of materials considered throughout this investigation, mixing procedure and mix proportions, methods of testing, and test setup and instrumentation of the flexural test.

Chapter 4 covers all experimental test results, including mechanical properties in

both fresh and hardened states, such as, compressive strength, splitting tensile strength, flexural strength, modulus of elasticity, free shrinkage, compatibility, and bond strength. In addition, the results from the flexural strength of the full-scale beams including load-deflection, load-strain, cracking and ultimate loads, mode of failure and cracking behavior, and the neutral axis.

Chapter 5 covers the code predictions and FEM and analysis. A comparison is presented among ACI 318 [2014], CSA A23.3 [2004], AASHTO-LRFD [2012], and ACI 544 [2011] codes in prediction the cracking load, ultimate load, and deflection. This is compared with the experimental results and presented in Chapter 5. The chapter also covers developing and validating FEM for both control and repaired beams. Finally, a parametric study results is also discussed in this chapter.

Chapter 6 summarizes the general conclusions and highlights the important findings.

CHAPTER 2 DETERIORATION AND REPAIR OF CONCRETE

2.1 Introduction

Concrete is the most widely used construction material for roads, dams, bridges, and buildings; the things that humans find necessary to transport their children, expand their businesses, and attain food and power. Simply put, concrete needs to work; its position in global society is too vital for it to fail or lose operation. However, although unfortunate, concrete is not impervious to deterioration over time, and its versatility is often limited to its load capacity. Therefore, it is imperative that concrete structures be thoroughly inspected and maintained over time and through changes in use.

Structures can require repair or maintenance for many reasons. The need to repair concrete can follow years of frost damage, deterioration due to weathering, improper design, fire exposure, an increase in load capacity, or even a simple change in code for the structure. This means that the need for repairs comes often, and this can be costly. According to Emmons [2006], repairs and maintenance cost the United States. \$18 to \$20 billion each year; highlighting the importance that repairs be done correctly and with the best, most effective materials available.

2.2 Causes and Types of Deterioration of Concrete

Despite the fact that concrete is used due to its durability, concrete can deteriorate due to the following factors:

- Corrosion of Reinforcement
- Chemical Attack

- Freeze/Thaw
- Fire/Heat
- Abrasion/Erosion
- Overload or Under Design
- Aggregate Reactivity
- Volume Changes

2.2.1 Corrosion of Reinforcement

Among the various issues resulting from concrete's moisture permeability is the corrosion of the concrete's reinforcement material. At this point, the factors causing the corrosion of steel reinforcement have been well identified. When an isolated steel bar has different electrochemical potentials, anode-cathode pairs can develop, causing corrosion in concentrated anodic regions. Generally, however, concrete's considerable alkaline composition (pH of 12 to 12.5) produces a thin layer of oxide on the steel reinforcement's exterior, preventing corrosion from occurring. Deterioration of the protective oxide film occurs when the concrete's pH declines below 11, allowing rust to form [Nawy, 2008].

Typically, the corrosion of steel reduces its cross-sectional area and causes degradation of the surrounding concrete, which can lead to structural collapse. The rust produced during steel corrosion expands, taking up an increased volume than the pre-corrosion steel. The result of this growth in volume is tensile stress in the concrete, which can eventually cause cracking, delamination, and spalling [Portland Cement Association, 2002]. An example of steel reinforcement corrosion in a surface wall is shown in Fig 2.1.



Figure 2.1 Steel Reinforcement Corrosion in a Reinforced Concrete Wall [Khayat, 2006]

2.2.2 Chemical Attack

Generally, concrete reacts well too many elements and conditions it is exposed to; these include moisture, soil particles, and other chemical substances. A variety of chemical conditions, however, can lead to the degradation of even the highest quality concrete. Because of their low permeability, solid, arid chemicals seldom affect concrete. Any substantial damage to concrete must be the result of harsh chemicals in solutions with a certain degree of concentration. These destructive substances are usually categorized as acids, salts, or sulfates [Newman and Choo, 2003].

The degradation of concrete caused by sulfates is identifiable by a pale whitish color most commonly appearing at the edges of the concrete. This white color is the product of the formation of calcium sulfate, or gypsum, and calcium sulfoaluminate, or ettringite. These products have larger volumes than their previous compounds, resulting in the

expansion of the surrounding hard concrete which can further create cracks and failures. Sulfates often occur naturally in soil or ground water. However, they can also be the result of fertilizers or industrial emissions [Marchand et al., 2003].

Acids can be extremely detrimental to Portland cement concrete as the cement has very poor resistance to acids. The severity of damage done to concrete by acids increases as the acid's pH value decreases; usually, damage begins at a pH lower than 6.5 and becomes severe at a pH less than 4.5. When exposed to acids with a pH value of 3 or lower, any concrete structure will face immense degradation and is not likely to resist failure for long. Acids work against concrete by reacting with the calcium hydroxide found in the concrete's hydrated regions. Generally, these reactions produce calcium compounds that are water-soluble and are then extracted out by aqueous solutions [Danish Standards Association, 2004].

The sulfurous gases emitted through the burning of various fuels may merge with moisture and produce sulfuric acid which, in turn, can cause concrete degradation. Sewers often face severe concrete deterioration due the high amounts of sulfuric acid converted from sewage by bacteria. Prevention of such deterioration usually involves surface protective remedies such coal-tar, epoxies, or rubbers [Portland Cement Association, 2002].

Salts that affect concrete structures can be the result of several occurrences such as the salting of roads during the winter or the existence of a body of salt water nearby. Among this group of salts that cause concrete degradation are the chlorides and nitrates of aluminum, iron, magnesium, and ammonium; those of the lattermost being the most destructive. Portland-cement-concrete's alkaline composition causes ammonium salts to

emit hydrogen ions and ammonia gas, which is then substituted with the calcium hydroxide in the concrete through dissolution, leaving gaps and cracks in the concrete. These salts can also cause concrete expansion due to their crystallization in the concrete's pores. Such crystallization occurs at the evaporation point of water and only when water is allowed to seep into the concrete. Therefore, concrete's resistance to permeability is important [Hilsdorf and Kropp, 2004].

2.2.3 Freeze/Thaw

When in concrete, water is not pure but rather a solution composed of a variety of salts. Therefore, water in concrete has a lower freezing point than that of exposed water out in the open. Furthermore, water's freezing point decreases proportionally to the size of the pores it is housed in; the smaller the pore, the lower the freezing point. Water also expands in volume as it freezes; generally, this expansion is approximately a 9 percent increase in volume. These characteristics of water can cause severe complications in concrete structures. Low ambient temperatures can easily cause the water in the concrete's pores to expand, thus resulting in internal tensile stress and, if not alleviated, local failure of the concrete. This sort of failure is prevalent in concrete that has saturated pores with little or no room for freezing water to expand into. Such expansion is heightened in situations with reoccurring freezing and thawing; where expanded concrete due to freezing is thawed and once again saturated. In this scenario, the concrete repeatedly expands, intensifying the tensile stresses and heightening chances of local failure [Newman and Choo, 2003].

The prevention of concrete deterioration due to freezing is usually achieved through the use of air-entraining agents. These agents, when combined with water, create minute

bubble pockets, which become part of the cement paste [Neville and Brooks, 2010]. Other preventative measures involve reducing the amount of moisture that enters the concrete, therefore ensuring that decreasing temperatures have a lessened effect on the concrete's expansion due to moisture [Kosmatka et al., 2003; Danish Standards Association, 2004].

Common methods of reducing the potential of moisture entering concrete are surface protection by hydrophobic impregnation, and by sealants and paints. In the first method's procedure, the impregnating liquid is deposited on the concrete's exterior, creating a water-resistant surface without creating a film. Although this method is effective, it does not provide complete protection during high-pressure rains or moisture contact. Typical products used for this procedure are silane and siloxane. Unlike hydrophobic impregnation methods, surface protection by sealant and paint usage creates a film on the concrete's exterior; this film is, in effect, a barrier that prevents any moisture from entering the concrete. Typically, either a sealant film with a thickness of 10 to 100 μm or a paint film of 0.1 to 5 mm is applied to the concrete's surface, to ensure surface protection. The main difference between the paint and sealant products lies in sealant's openness, and paint's impermeability to water vapor diffusion [Danish Standards Association, 2004]. Fig 2.2 illustrates an example of freeze and thaw deterioration.



Figure 2.2 Freezing and Thawing Deterioration to the Downstream Face of a Concrete Dam [<http://civildigital.com>]

2.2.4 Fire/Heat

Concrete's ability to maintain its structure and strength over a wide range of temperatures is well known; however, when it is exposed to fire or uncommonly high heat it can experience strength and rigidity loss. When concrete is heated, it expands, therefore, when in contact with fire, concrete's exterior will swell more rapidly than its interior, causing the exterior to fracture. The reverse is also possible; if concrete is heated and rapidly cooled fracturing can also occur, such as when sprinklers cool concrete structures down after fire [Buchanan, 2001].

Although all types of concrete can experience degradation when exposed to fire or severe heating, the situation each type of concrete is in can cause the effects to vary. Concrete that endures repeated heating and cooling exhibits more severe loss of strength than concrete that maintains a consistent temperature; the reason for this being the great

spatial changes that occur between the concrete's aggregate and cement paste [Portland Cement Association, 2002].

As well as temperature cycling, differences in load and composition between concrete structures can cause varied responses to concrete's response to a fire or high temperature. Loaded concrete generally performs better under these conditions than unloaded concrete due to its compressive stresses that retain its form despite the high temperatures. Also, concrete composed of calcareous aggregates has been shown to respond better to these conditions than those composed of siliceous aggregates. Concrete experiences a decreased loss in compressive strength if it has a higher aggregate to cement ratio. This should not necessarily be viewed as a solution for the prevention of failure of concrete structures undergoing high temperatures, as a higher aggregate-cement ratio can cause greater loss of elastic modulus [Newman and Choo, 2003].

2.2.5 Abrasion/Erosion

Concrete experiences abrasion damage if it is unable to endure deterioration caused by friction and grating. This process begins when the concrete's exterior layer is exposed to the sliding and scraping of hard particles, revealing its interior layers of aggregate. After this, further impact and friction result in deterioration based on the concrete's aggregate rigidity and aggregate-paste bonding strength. Such abrasion of concrete is common on concrete road surfaces including bridges, overpasses, and pathways. Here, the tough rubber tires, chain tires, or even footwear cause grating of the concrete's surface, gradually wearing it down. To prevent this sort of damage, concrete with high compressive strength should be used, as abrasion resistance of concrete is directly proportional to the concrete's compressive strength [Hilsdorf and Kropp, 2004].

Often, abrasion of concrete will involve hydraulic structures since many concrete structures contain water and other fluids traveling around them. Damage is usually the result of water carrying debris such as sand, gravel, silt or ice, rather than just friction caused by water itself. Without debris, traveling water would have little impact on concrete structures even if traveling at high speeds. In cases where there is a substantial amount of debris, abrasion erosion can span from a few inches to several feet, depending on the water's flow conditions. Just as with concrete road surfaces, prevention of abrasion of hydraulic structures can be achieved by selecting high strength concrete with hard aggregates [Portland Cement Association, 2002].

2.2.6 Overload or Under Design

Overloading occurs when concrete members do not have the strength needed to bear the load they are carrying, resulting in failure. This kind of failure can arise in numerous situations, both naturally occurring and as a result of poor design or planning. Unnaturally occurring causes of overloading include premature removal of the temporary framework, change in structural usage without proper upgrading, and improper support of members during transportation and construction. The impact is also a major factor in structural overloading; this commonly happens when vehicles travel on slab edges on road or bridge surfaces [Nawy, 2008].

2.2.7 Aggregate Reactivity

The aggregates used in concrete are ordinarily considered as chemically inert. Despite this, certain aggregates can react with the alkali hydroxides housed in the concrete, potentially resulting in expansion and cracking over a period of time. Such reactivity is categorized as either Alkali-Silica Reaction, or ASR, and Alkali-Carbonate Reaction, or

ACR. ASR reactions are usually viewed with more concern, as aggregates containing reactive silica-based materials are more prevalent [Portland Cement Association, 2002].

Figure 2.3 shows the deterioration of concrete due to ASR reaction.



Figure 2.3 Cracking of Concrete from ASR [Kosmatka and Panarese, 2002]

2.2.8 Volume Changes

Changes in concrete's volume may occur for several different and often unrelated reasons. If a concrete structure was unrestrained, volume changes would seldom be a problem. However, reinforcements, foundations, connecting members, and many other elements bind most concrete structures. As concrete shrinks or expands these restraints can cause tensile stresses that further produce cracking in the concrete. Although the most common causes for this expansion and retraction are temperature fluctuation and changes in moisture content, chemical effects including sulfate attack and carbonation can also disrupt concrete's volume [Kosmatka and Panarese, 2002].

Concrete has a coefficient of thermal expansion of 5.5 millionths per degree Fahrenheit, equaling a change in length of 0.66 inches for 100 feet when exposed to a temperature change of 100 degrees Fahrenheit. Therefore, great changes in temperature

can produce destructive volume changes to large concrete structures such as bridges, dams, or buildings [Nawy, 2008].

2.3 Selecting and Testing of Repair Materials

Concrete's versatility and variable properties have made it the most widely used construction material. Being a construction material whose physical properties can change over time, due to chemical or physical reasons, concrete requires regular evaluation and, oftentimes, repair. Nawy [2008] stated that the American Association of State Highway and Transportation Officials (AASHTO) evaluates that 40% of U.S. highways have below minimum standards of engineering, and due to the ages of many of these structures; these weaknesses are likely the result of poor repair methods and materials [Nawy, 2008]. Not only do inadequate repairs render structures unsafe, but they also create economic costs that could be avoided had appropriate repair materials and methods been utilized. In industrially developed countries, around 40 percent of the construction industry's entire resources are applied to repair and maintenance of existing structures and only 60 percent of new projects, this suggests that a significant portion of repairs are ineffective or short-lasting [Mehta and Monteiro, 2006].

Figure 2.4 shows the selection process of a repair material, which accounts for all applicable parameters and their impacts on the choice between alternatives [Emmons, 1993; Cusson and Mailvaganam, 1996; ACPA, 1998]. Generally, the effectiveness of concrete repair is based upon adequate material use and application [Poston et al., 2001]. Before these materials and methods are chosen to be implemented on an existing structure, their physical and mechanical interactions with the substrate they will be applied to must

be established in a lab setting in order to ensure maximum effectiveness [Mangat and Limbachiya, 1995]. Studies of such repair materials and methods have pointed to weaknesses in compressive strength, stiffness, flexural strength, creep coefficient, etc., as being strong indicators of the durability of a concrete repair. These weaknesses may produce the initial tensile strains that cause de-bonding between the repair and substrate or cracking in the repair material itself [Mangat and Limbachiya, 1995; Poston et al., 2001; Pattnaik, 2006; Mehta, 2006; Nawy, 2008]

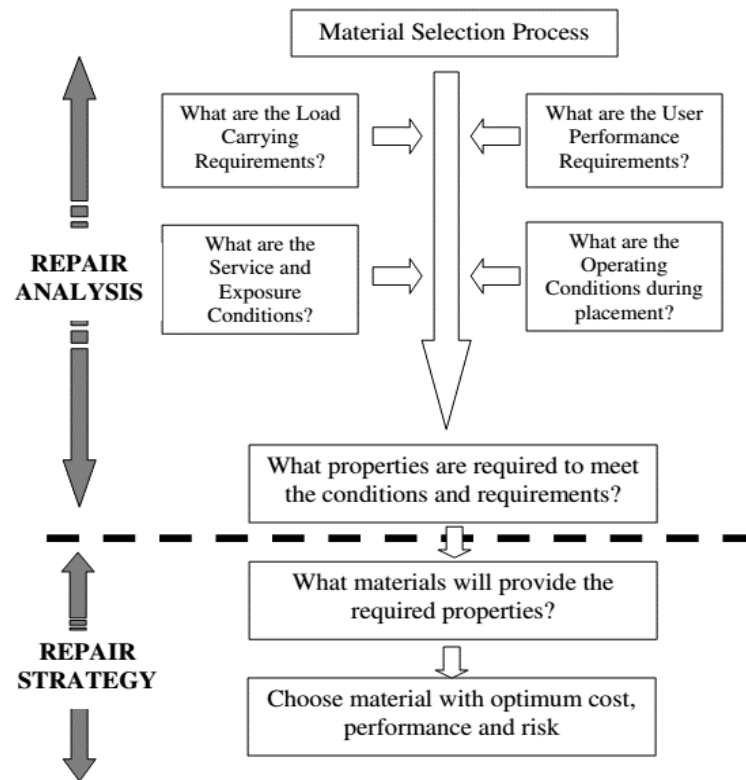


Figure 2.4 Flowchart Illustrating the Selection Process for a Repair Material

[Emmons, 1993]

2.3.1 Compressive Strength

Compressive strength is not regarded as an entirely important factor when

considering repair materials. When concrete requires repair, its regions of cracking or fracture are generally areas under tensile stress, which is an entirely different factor than compressive strength. However, to ensure that the repair material retains its stability under a load, a repair material with strength qualities equal to or surpassing those of the substrate are usually used [Pattnaik, 2006]. This test is performed with the use of a loading machine, which applies an increasing load to the substrate repair sample until failure. The results of this failure determine the load capacity of the repair material.

2.3.2 Flexural Strength (Compatibility)

Flexural strength of concrete is often analyzed through a third-point loading test in which a rectangular concrete prism is subjected to three points of force—causing tensile stresses at its bottom side and compressive stresses at its top. Depending on the point of failure determined through the three-point flexural test, a concrete sample's compatibility with a repair material is determined. If a failure crack appears through the repair material and the substrate, or through only the substrate, the two materials are compatible. If, however, a failure crack appears through the bonded area between the substrate and repair, the two materials are incompatible as shown in Figure 2.5. This test a good indicator of how a repair material will perform under tensile stresses when in a real setting.

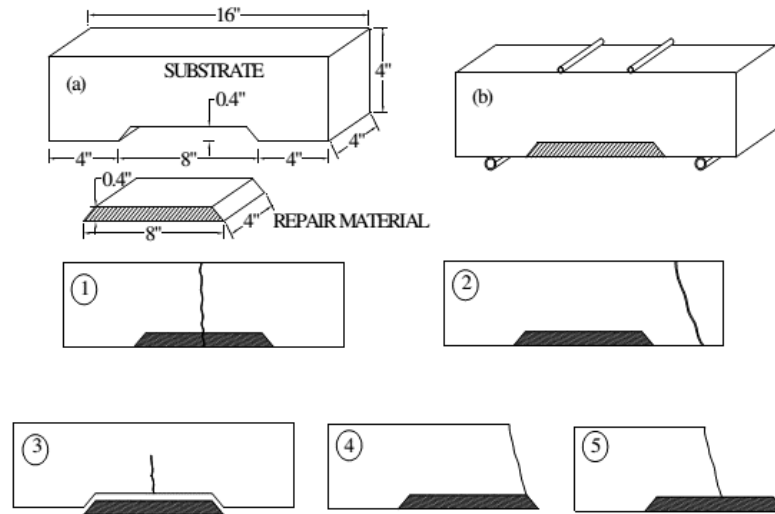


Figure 2.5 Compatibility Test and evaluation: 1,2-compatibility; 3,4,5-incompatibility (a) Specimen arrangement; (b) Third point loading beam test [Czarneck et al 1999].

2.3.3 Modulus of Elasticity

The test for modulus of elasticity of concrete is usually performed on concrete cylinder molds. Longitudinal stresses are applied to the cylinder while a device around the cylinder measures its deformation. The full process of this test can be found in ASTM C469.

Because concrete with a high modulus value deforms less than that with a low modulus value, concrete with a lower modulus transfers its stresses to the higher modulus concrete potentially causing cracking (Figure 2.6). Therefore, it is imperative that repair materials have a similar modulus value to that of the substrate [Pattnaik, 2006].

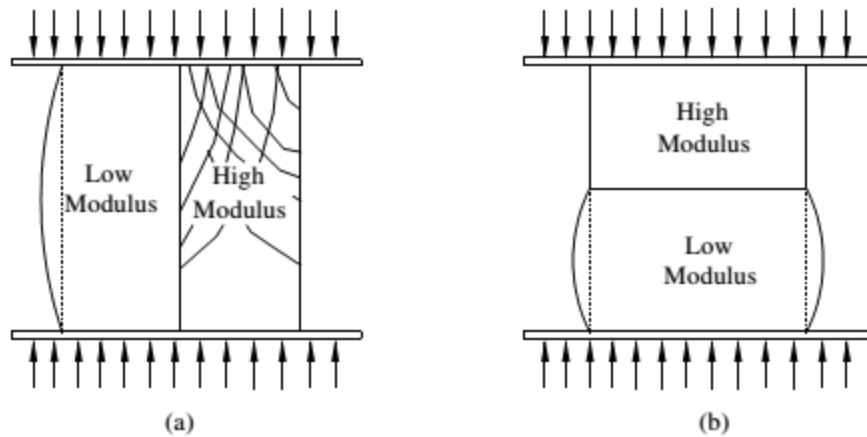


Figure 2.6 Effects of Mismatching Elastic Moduli (a) Load parallel to interface

(b) Load perpendicular to interface [Cusson and Mailvaganam 1996]

2.3.4 Bond Strength by Pull-off Test

This method of testing is a strong indicator of the durability of repair materials on a concrete substrate, as it tests the tensile strength required to de-bond a portion of the repair material from the original concrete [Czarnecki et al., 1999]. This is helpful for predicting how a repair material will behave in a real repair situation.

In this procedure, a core-cutout is made through the repair material slightly into the substrate. The repair material is then glued to a piston which pulls the repair away from the substrate. The value at which the repair is de-bonded from the original concrete is equal to the maximum tensile stress the repair can manage before its failure to hold [Czarnecki et al., 1999; Robins and Austin, S. A., 1995]. The test setup is shown in Figure 2.7

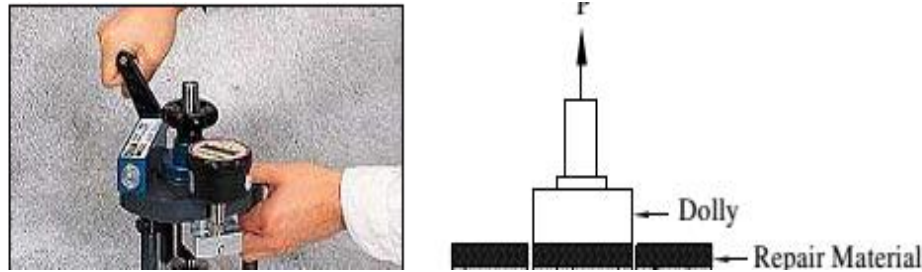
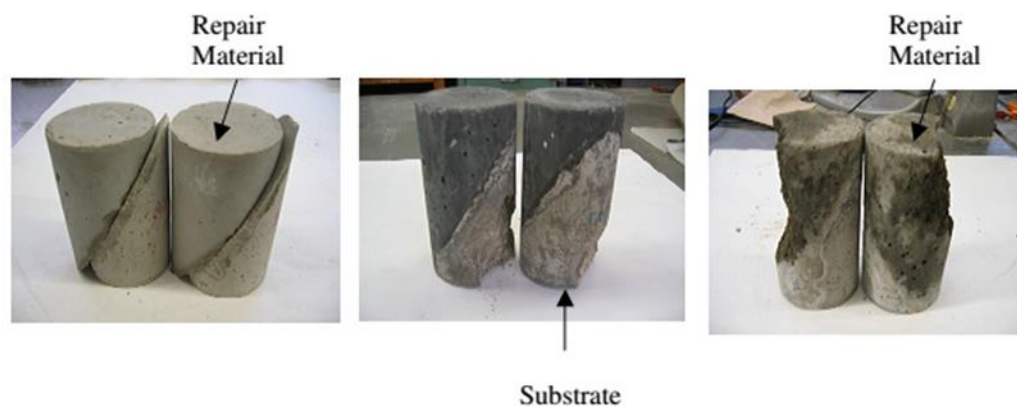


Figure 2.7 Pull off Test Instrument [Pattnaik, 2006]

2.3.5 Slant Shear Bond Strength Test

This method tests the bond strength between the substrate concrete and repair material by simultaneously exposing a cylindrical sample to compressive and shear stresses. The cylinder being tested is half-composed of the substrate and half-composed of the repair material, divided in the middle at a 60-degree cut angle, which produces an elliptical-shaped contact surface between the materials. The bond strength between the substrate and repair is dependent on several factors: friction, the adhesive strength of the bonding substance, compaction of the substance, cleanliness of the substrate's surface, etc. This procedure is explained in ASTM C882. According to Pattnaik [2006], three possible failure modes can happen as shown in Fig 2.8. If the failure occurred in the bond, then the failure mode will be interface failure. The second failure mode is substrate failure, and that's when the failure takes place in the substrate. While the last failure mode is repair material failure and that failure happens when the repair material fails before the substrate.



(a) Interface Failure (b) Substrate Failure (c) Repair Material Failure

Figure 2.8 Failures Modes of the Composite Slant Shear Test [Pattnaik, 2006].

2.4 Types of Repair Materials

There are many types of commercially and custom mix repair materials available in the markets. Back between 1994 and 1995, over 120 manufactures of concrete repair materials were listed by Aberdeen's sourcebook. Each manufacturer produces more than one type of repair materials and that Leads to hundreds of repair materials in the markets since that time. Despite the fact that there are a lot of commercially repair materials available, they can be categorized into a small number of groups. Emberson and Mays, [1990] classified the repair materials into categories as shown in Table 2.1.

Table 2.1 Categories of Repair Materials

Cementitious Materials	Polymer-Modified Cementitious Materials	Resinous Materials
Ordinary Portland cement/mortar	Styrene butadiene modified rubber	Epoxy mortar
High Alumina cement/mortar	Vinyl Acetate modified	Polyester mortar
Flowing concrete	Magnesium phosphate modified	Acrylic mortar

The most distinguishing factor among different types of repair material is the type of binder used. Given that the type of binder primarily determines the properties of the repair material, repair materials generally are formulated with one of two different types of binders. The first is hydraulic cement, which is predominantly composed of Portland cement and magnesium phosphate-based binders. The second type of binder is a polymer, the majority of polymer binders are either epoxy or acrylic. The other primary constituent found in repair materials is the filler. Fillers (such as natural aggregate) are normally used in all repair materials and serve a variety of purposes [Brain et al., 2009].

Cementations materials are more economic than resin mortars and have compatible thermal expansions and movement characteristics with the concrete substrate, easier to mix, can be used in large volumes and have lower exotherms during curing than the resin materials. The low tensile strength and extensibility and the stress induced by drying shrinkage may lead to the cracking or de-bonding of the cementations repair materials [Alsayed, 2005].

Conventional concrete remains as one of the most reliable patching materials if properly designed, placed, and cured. In an attempt to reduce the time required for repairs, the construction industry has seen a significant increase in the use of “rapid-set” concrete patching materials [Swathi, 2004].

Rapid-hardening cements are defined as those that can develop a minimum compressive strength of 3,000 psi within eight hours or less [James, 2009]. The primary purpose of using this type of repair material is to minimize the out-of-service time for repairing pavements and bridge decks. These materials include concretes made with Type

III Portland cement, concretes containing regulated-set Portland cement, gypsum-based concrete, magnesium phosphate concrete [Pattnaik, 2008].

Polymer modified cement mortar is a modified mortar in which part (10 to 15% by weight) of the cement binder is replaced by a synthetic organic polymer [Blaga, 2005]. Polymer-modified cement mortar has an excellent durability, high bond characteristics to the substrate, good workability, and high resistance to abrasion and is easy to apply. However, it is expensive, has a high tendency toward plastic shrinkage, slightly, sensitive to high and low temperature at the time of application [Alsayed, 2005]. A great variety of latexes are now available for use in polymer-modified cement concrete products and mortars. The most common latexes are based on polymethyl methacrylate (also called acrylic latex), polyvinyl acetate, and vinyl chloride copolymers [Blaga, 2005].

Epoxy materials are well known and accepted materials for repair. However, there are many problems associated with the use of epoxy materials. First, they do not allow moisture to evaporate. This may cause some internal pressure which may cause de-bonding between the substrate and the epoxy. This is particularly the case in humid areas where moisture can reach the bond line from within the old concrete. Second, the pot life for epoxy materials is critical, and in a hot climate, as is the case of the Gulf Region, this may not be more than a few minutes [Alsayed, 2005]. Therefore, there will always be a great chance that they harden before the overlay could be placed. In such cases, the epoxy materials will act as a barrier between substrate and repair materials and significantly reduces the bond. The seriousness of such problem may be more pronounced when repairing upright surfaces. In general, resin-based materials are preferred where thin sections have to be applied to benefit from the low permeability of resin materials together

with good adhesion and lack of special curing requirements. For large repairs, however, it is preferable to use cement-based materials [Alsayed, 2005]. Recent researches, James, [2009] and Blaga [2005] has also studied the applicability of high strength and high-performance concrete as a potential repair material for rehabilitation and repair. The possible benefits of using these materials include reduced construction times, rapid repairs, improved durability, reduced wear, and increased the life of the facility [Zia, 1991; Ehlen, 1997].

2.5 Why SCC and FR-SCC as a Repair Material?

Since its advent in 1986 at the Koche University of Technology in Japan, SCC has been extremely popular in construction due to its ease of flow and ability to consolidate under its own weight. The initial purpose of SCC was to combat the decreasing quality of construction work due to reducing numbers of skilled workers in the construction industry. Despite the significantly reduced levels of strength the early SCC mixtures had, the concrete has since been well developed, incorporating several materials such as Blast Furnace Slag (GGBS), Condensed Silica Fume (CSF), and a series of admixtures. These additives which have allowed it to maintain significant levels of strength [Nawy, 2008]. Although SCC is successful in compensating for reductions in skilled labor, it also has several other benefits, including [Newman, 2003]:

- Increased productivity levels are resulting in reduced construction time.
- A decrease in construction costs.
- Improved structural quality in tough casting situations.
- Improved working environments.
- Greater surface-finish quality.

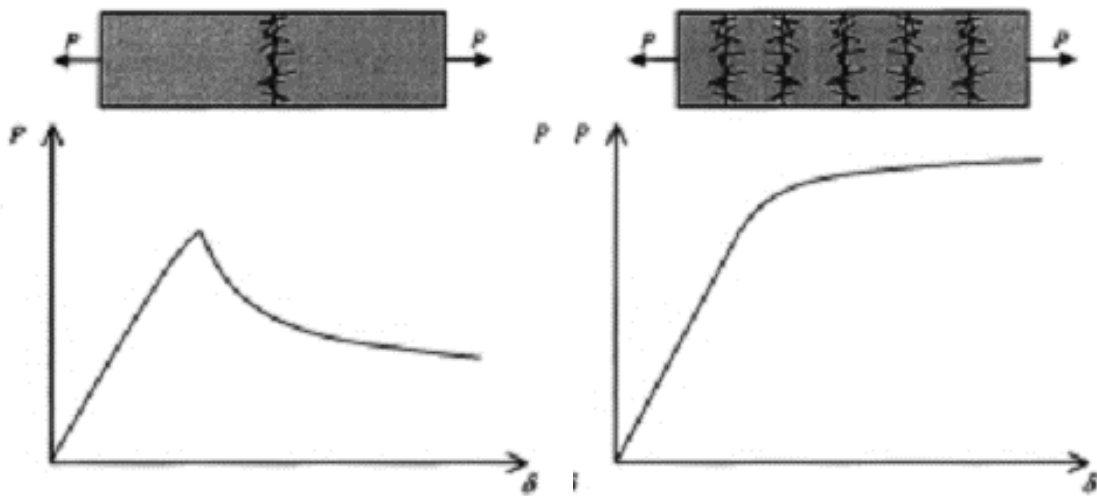
- Enhance environmental loadings.

SCC has been defined as a highly flowable, yet stable concrete that can spread readily into place and fill the formwork without any consolidation and without undergoing any significant separation. This means that SCC is extremely useful even in conditions that involve heavily reinforced members or intricate formwork. Conventional concretes with much lower flowability would require careful and arduous vibration in order to fill the entire form's volume while avoiding any segregation. This ability of SCC to conform to any mold or formwork without vibration has proven its versatility in the field and has given constructors confidence that their work will be quick, quiet and clean [Khayat, 1999; Nawy, 2008; Brown and Duke, 2010].

Self-consolidating concrete's ability to flow is achieved due to its increased amount of fine material, such as fly ash or slag, without varying the amount of water in comparison to general concrete. This method alters the concrete's rheological qualities, allowing its coarse aggregate to sit in its mortar without any segregation. Because of this ability to hold aggregate without segregation, it has been recognized that the addition of fibers to SCC markedly improves its structural properties including its compressive and static strengths, impact strength and tensile strength [Kamal et al., 2014].

In addition to the enhancement in the flowability and engineering properties, including the fiber in the SCC will change the crack formation and propagation mechanism significantly. When unreinforced concrete fails in uniaxial tension, the failure is governed by the formation of a single crack. When a crack is formed in fiber reinforced concrete, the fibers will typically stay unbroken. The fibers crossing a crack will resist further crack opening and impose what is called crack closing or crack bridging effect on the crack

surfaces. Different failure modes can result, depending on the effectiveness of the fibers in providing crack bridging, see Figure 2.9. If the fibers break or are pulled out during crack initiation, or if the fibers cannot carry more load after the formation of the first through crack, then the first cracking strength is the ultimate strength. Further deformation is governed by the opening of a single crack and fibers pulling out and/or breaking along the edges of the crack as shown in Figure 2.9(a). This behavior is also known as tension softening behavior. If-on the other hand-the fibers can sustain more load after the formation of the first crack, more cracks will be formed and what is known as multiple cracking as show in Figure 2.9(b). This behavior is also known as strain (or pseudo-strain) hardening behavior [Vandewalle, 2002].



a) Single cracking under uniaxial loading b) Multiple cracking under uniaxial loading

Figure 2.9 The Behavior of Single and Multiple Cracking of the Specimens under Uniaxial Loading [Vandewalle, 2002]

The SCC initial case study was performed at a parking garage in Quebec, in 1996 [Khayat, K. H. and Aïtcin], 1998. The SCC was used to repair the underneath and sides of a 20-foot beam. The beam under repair had substantial corrosion damage surrounding a joint at the entrance of the lot. The area to be repaired housed lateral-bar-reinforcement and stirrups connected to the substrate concrete which proved to be a problem for the application of repair concrete. The decided method for applying the SCC was to bore two 4” holes through the beam’s deck between the present substrate and formwork. The SCC successfully flowed to fit the placed formwork despite the reinforcement obstacles; it exhibited the following properties that summarized in Table 2.2.

Table 2.2 Summary of the Properties of SCC used in Repairing the Parking Garage in Quebec

Slump flow	25 in. (612mm)
Flow time	4.0s
Filling capacity	61%
Surface Settlement	0.39%
Compressive strength – 28 days	5100psi. 91 days: 6000 psi.
Drying shrinkage	600 $\mu\text{m}/\text{m}$ after 180 days. (Moderate)
Air void spacing factor	40 μin (200 μm)
Frost durability coefficient	90% (Excellent)

The Quebec Department of Transportation’s primary specifications for SCC based on performance were written in 1997 and have since been used in many reparation projects. Since the onset of its use, SCC has exhibited not only ease in application but also strength

in durability and substrate bonding [Khayat, K.H. and Aïtcin, 1998; Khayat et al., 2010]. These positive performances have caught the attention of several other construction companies and transportation firms in both Canada and the United States. Examples of such repair efforts using SCC are visible in Figs 2.10 through 2.13.



Figure 2.10. Application of SCC for Repair of Bridge Pier Caps and Columns in Quebec [Khayat et al, 2010].



Figure 2.12. Repair of Bridge Pile Damaged by a Barge in Virginia, repaired pile on the right picture [Ozyildirim, 2013].



Figure 2.13. Repair of Damaged Column and Pier Cap in Virginia on the Left, Completed Repair on the Right) [Ozyildirim, 2013].

It is well known that repairs done using concrete are especially susceptible to cracking as a result of shrinkage. To combat this frequent occurrence, fiber reinforcement has been increasingly used to improve tensile and flexural strength while reducing cracking. Not only does FR-SCC have an easy application, just as with standard SCC, it also has increased performance in its hardened form in comparison to conventional concrete; as a direct result of the fiber reinforcement. FR-SCC requires lower amounts of steel reinforcement and ties, lower maintenance, and a smaller labor force. The benefits of using FR-SCC as a repair material were exemplified in 2003, during the repair of the 860 ft Jarry/Querbes Underpass as shown in Figure 2.14. Due to repeated exposure to frost, the underpass experienced harsh deterioration. The repairs needed included sidewalk, pavement and side wall reconstruction. Of the 32 panels cast for the retaining walls, 29 were cast with FR-SCC. In its finality, the underpass was both visually pleasing and effectively repaired, with no cracking due to shrinkage. Because synthetic fibers were used to reinforce the repair concrete, the fresh repair was able to fill voids while maintaining a high level of strength effectively.

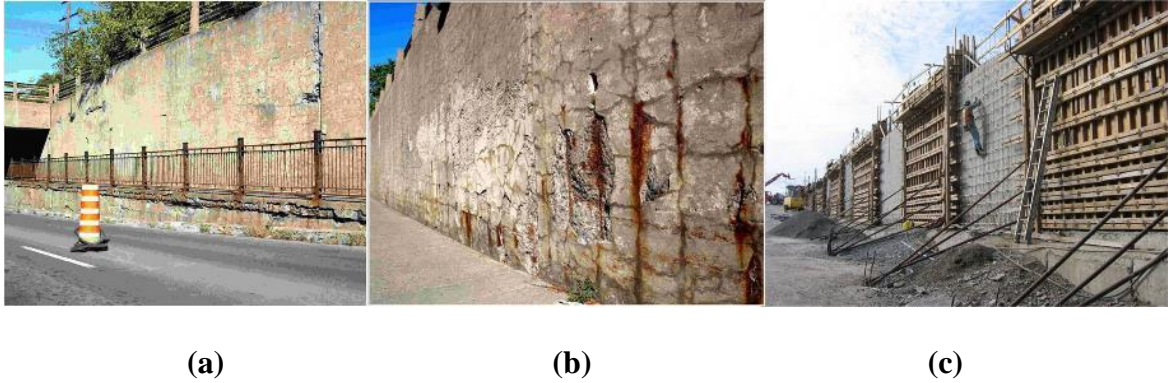


Figure 2.14. Application of FR-SCC in Jarry/Querbes Underpass in Montreal [Khayat et al, 2005].

The performance of fiber-reinforced self-consolidating concrete for repair of reinforced concrete beams was studied by Kassimi et al. [2014]. The study aimed to evaluate the influence of different types of fibers on the flexural response and durability and to develop fiber-reinforced mixtures targeted for the use in repair applications. Ten repaired beams were tested under four-point bending over a simply supported span. Two mixture types Self Consolidating Concrete (SCC) and Self Consolidating Mortar (SCM), and four fiber types were used as a repair material in this study. The types were two synthetics, one hybrid, and one steel fiber type. Fiber volume fractions, V_f were: 0, 0.3%, 0.5%, for concrete mixtures, and 1.4% for FR-SCM.

The results showed that the use of optimized FR-SCC mixtures enabled the replacement of 50% of the tension steel reinforcement in repair sections; i.e., the number of bars in the tension zone decreased from three bars to two bars with the addition of fibers in the SCC without mitigating structural performance.

2.6 Research Need

Considerable research studies were undertaken to investigate the engineering properties of SCC and FR-SCC containing various types of mineral admixtures such as fly ash, slag, silica fume and other mineral by product. Further, very limited amount of work has been carried out concerning the use of SCC and FR-SCC in repair and strengthening of concrete structures.

Dimensional compatibility and bond strength between the repair and the substrate are important factors in repair and yet there is no research have examined the compatibility and bond of SCC or FR-SCC as a repair material with the substrate concrete.

CHAPTER 3 EXPERIMENTAL SETUP

3.1 Introduction

Despite much experimental research on the mechanical properties of FR-SCC, there is limited experimental work conducted on examining these materials for repair purposes. In addition, the studies conducted by Abdul-Hameed [2010] Hassan et al. [2010], and Mansi [2010] have proven that good engineering properties do not guarantee a successful repair. Hence, an experimental program is necessary to evaluate the viability of using the FR-SCC as a repair and construction material. For this objective, the work have been conducted to design the SCC and FR-SCC mixtures, select and test mixtures for compatibility and bond strength, and to study the flexural behavior of repaired beams. This chapter provides information about materials used, mix proportions, mixing procedure, and methods of testing

The experimental program was initiated by testing the fresh and hardened concrete properties of SCC and FR-SCC mixtures. A control mixture and 13 FR-SCC mixtures with two types of pozzolanic admixtures (Silica Fume (SF) and Slag Grade 120 (SL)) were prepared. Two types of fibers (steel and polypropylene) with different percentages were used. Table 3.1 shows the mixtures considered in the initial testing. Figure 3.1 shows the material testing of various mixtures.

Table 3.1 Proposed Mixtures and their Abbreviations

	Mixture	Abbreviation
1	Class A(control) (without fibers)	Control
2	10% Silica fume (without fibers)	10SF
3	10% Silica fume + 0.25% Steel fibers	10SF25S
4	10% Silica fume + 0.5% Steel fibers	10SF50S
5	10% Silica fume + 0.10% Polypropylene fibers	10SF10P
6	10% Silica fume + 0.15% Polypropylene fibers	10SF15P
7	10% Silica fume + 0.20% Polypropylene fibers	10SF20P
8	35% Slag (without fibers)	35SL
9	35% Slag + 0.25% Steel fiber fibers	35SL25S
10	35% Slag + 0.5% Steel fibers	35SL50S
11	35% Slag + 0.15% Polypropylene fibers	35SL15P
12	35% Slag + 0.2% Polypropylene fibers	35SL20P
13	35% Slag + 0.25% Polypropylene fibers	35SL25P

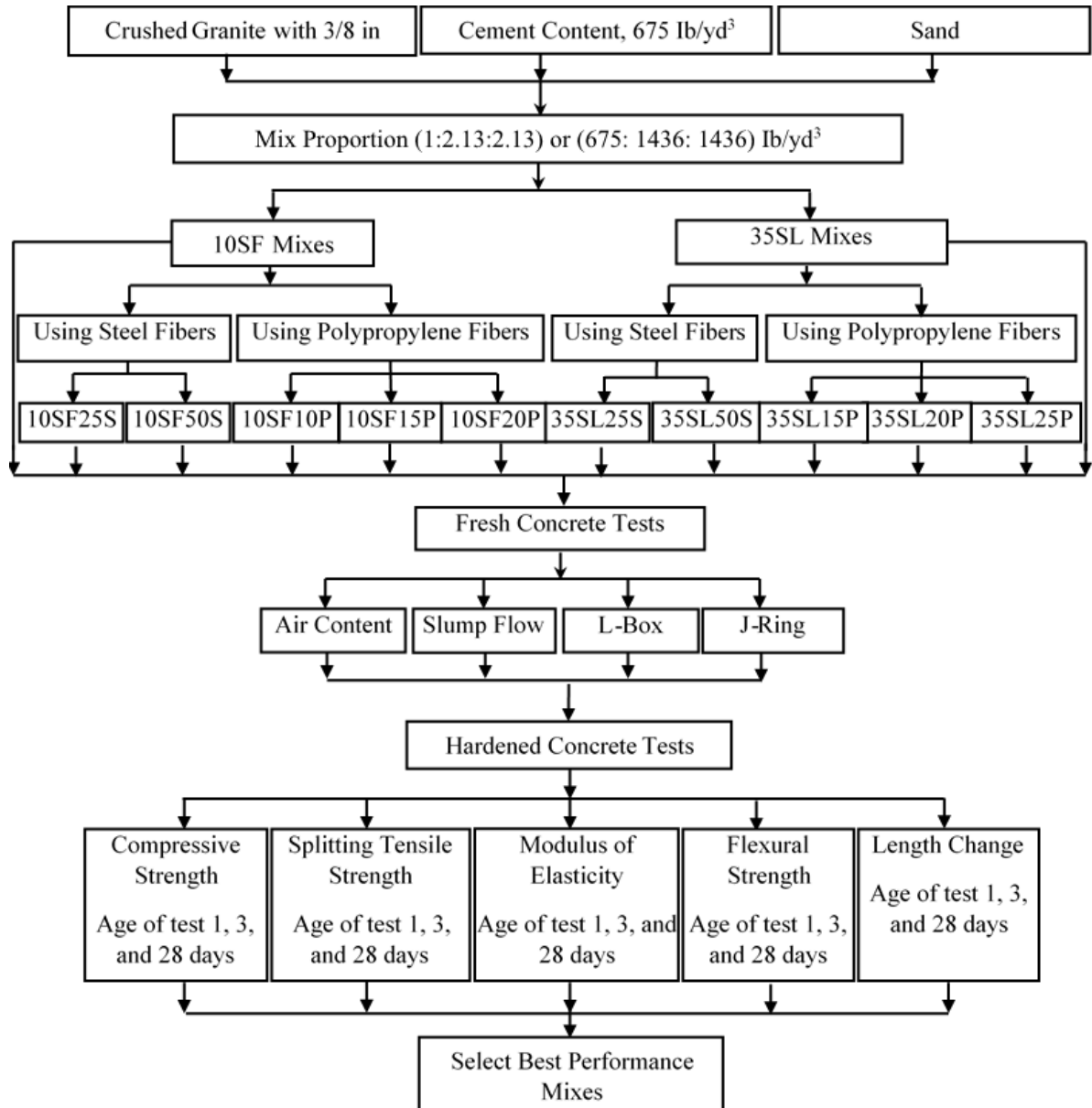


Figure 3.1 Flow Chart for the Initial Material Testing

3.2 Materials

3.2.1 Cement

Ordinary Portland cement (OPC) manufactured by Buzzi Unicem USA was used in this investigation. It was stored inside the laboratory on a pallet to avoid any effect of atmospheric conditions and to maintain constant quality. The chemical composition and physical properties of the cement are shown in Tables 3.2. The cement conforms to ASTM C150 Type I cement.

Table 3.2 Chemical Composition and Physical Properties of the Cement*

Chemical property	Result	Physical property	Result
SiO ₂ (%)	20.0	Time of Set (Vicat)	
Al ₂ O ₃ (%)	4.7	Initial Set (min.)	114
Fe ₂ O ₃ (%)	3.2	Final Set (min.)	216
CaO (%)	61.7	Compressive Strength (psi)	
MgO (%)	3.3	1 Day	2734
SO ₃ (%)	3.8	3 Day	3842
Total Alkali (Na ₂ O + 0.658K ₂ O)	1.02	7 Day 28 Day	4656 –
Ignition Loss	0.9		
Insoluble Residue (%)	0.55	Cube Flow	
C ₃ S (%)	52.1	Fineness, Blaine (cm ² /g)	3820
C ₂ S (%)	18.1	325 Mesh (%)	91.5
C ₃ A (%)	7.0	Air Content (%)	7.7
C ₄ AF (%)	9.7	Normal Consistency (%)	26.3
C ₃ S + 4.75C ₃ A	85.1	False Set (%)	65
CO ₂ (%)	1.6	Autoclave Expansion (%)	0.09
Limestone (%)	0.7	ASTM C563 (%)	4.50

*Chemical composition and physical properties of the cement were carried out by Buzzi Unicem USA.

3.2.2 Aggregate

Both fine and coarse aggregates were obtained from the Clayton Company located in Edison, NJ. The maximum coarse aggregate size was 3/4 in (#57) for Class A substrate concrete and 3/8 in (#88) for SCC and FR-SCC. The sieve analysis for all three types of aggregate was done according to ASTM C136. Table 3.3 shows the results of the sieve analysis. The results showed that all aggregates are conform to ASTM C33 recommendations. Figure 3.2 shows the particle size distribution. It observed that all of the aggregates used are well graded.

Table 3.3 Grading of the Aggregate Used

Sieve No.	Sieve Size (inch)	Percent Passing (Fine)	Percent Passing (Coarse #8)	Percent Passing (Coarse #57)
1.5"	1.5	100.00	100.00	100.00
1"	1	100.00	100.00	100.00
3/4"	0.75	100.00	99.96	80.08
1/2"	0.5	100.00	99.98	20.28
3/8"	0.375	100.00	88.96	3.03
#4	0.187	99.23	10.00	0.50
#8	0.0937	95.37	0.82	0.50
#16	0.0469	82.65	0.70	0.50
#30	0.0234	55.95	0.70	0.50
#50	0.0117	15.73	0.70	0.50
#100	0.0059	1.75	0.70	0.50
#200	0.0029	0.17	0.70	0.50

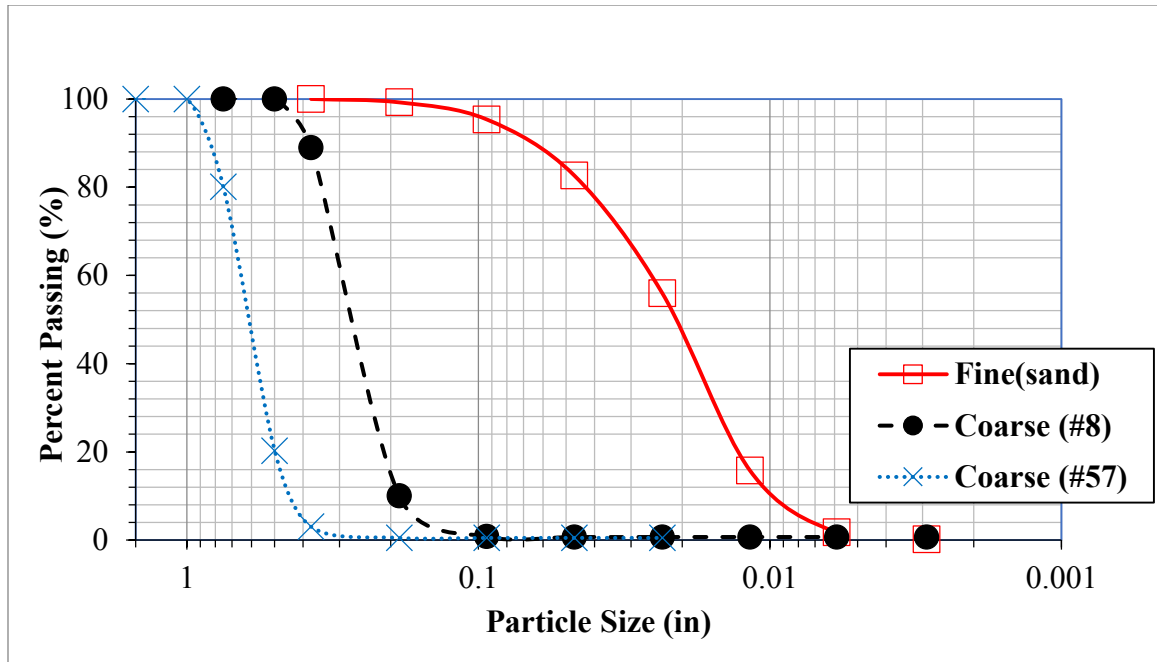


Figure 3.2 Particle Size Distribution Curve for the Aggregate Used

3.2.3 Silica Fume

SF is a very fine pozzolanic material, composed of amorphous silica produced by electric arc furnaces as a byproduct of the production of elemental silicon or ferro silicon alloys. The densified silica fume used throughout this work is from Norchem Company North America, and its properties are summarized in Table 3.4.

3.2.4 Slag 120

The SL was brought from Lafarge North America. The chemical and physical properties are shown in Table 3.5.

Table 3.4 Silica Fume Properties*

Properties		
	Result	Specification
State	Amorphous - Sub-micron powder	
Color	Gray to medium gray powder	
Specific Gravity	2.10 to 2.40	
Solubility	Insoluble	
Bulk Density - Densified	42 to 48 lb/ft ³ (674 to 770 kg/m ³)	
Bulk Density - Undensified “as produced”	12 to 20 lb/ft ³ (192 to 320 kg/m ³)	
Chemical Properties		
Silicon Dioxide (SiO ₂), %	93.47	85.0 Min
Moisture Content, %	0.27	3.0 Max
Loss on Ignition (LOI), %	3.82	6.0 Max
Physical Properties		
Oversize percent retained on 45- µm (325 sieve), %	2.54	10.0 Max
Accelerated Pozzolanic Strength Activity Index with Portland cement (7-day), %	126.07	105.0 Min
Specific Surface, m ² /g	22.28	15 Min

*Silica fume properties tests were carried out by Norchem Company North America.

Table 3.5 Chemical and Physical Properties of Slag 120*

Chemical Properties		
	Result	Specification
Sulfide Sulfur (S), %	1.0	2.5 max
Sulfate Ion (as SO₃), %	-0.5	4.0 max
Physical Properties		
Slag Activity Index, %		
7-day	109	95
28-day	142	115
Fineness		
Blain, cm ² /g	5940	n/a
45 microns	1	20 max
Air Content, %	2	12 max

*Properties results of slag 120 were provided by Lafarge North America.

3.2.5 Fibers

The steel fiber (STF) used is macro crimped with a length of 1.5 in. known commercially as PSI Crimped Steel Fiber, while the polypropylene fiber (PPF) is micro 1/4 in. long known commercially as PSI Fiberstrand 100. Both fibers were made and donated for the project by Euclid Chemical Company. Tables 3.6 and 3.7 indicate the technical information of PSI Crimped Steel Fiber and Fiberstrand 100 respectively. Fig 3.3 shows the both type of fiber.



a) PSI Crimped Steel Fiber



b) PSI Fiberstrand 100 Polypropylene Fiber

Figure 3.3 Types of Fibers Used

Table 3.6 Technical information of PSI Crimped Steel Fiber*

Material	low carbon cold drawn steel wire
Deformation	continuously deformed circular segment
Typical Dosage Rates	25 - 100 lb/yd ³ (15 - 60 kg/m ³)
Length	1 ½" (38 mm)
Aspect Ratio	34
Tensile Strength	140 - 180 ksi (966 - 1242 MPa)
Appearance	bright, clean wire

* Technical information of PSI Crimped Steel Fiber was provided by Euclid Chemical Company.

Table 3.7 Technical information of PSI Fiberstrand 100*

Material	100% monofilament polypropylene
Specific Gravity	0.91
Typical dosage rate	1.0 lb/yd ³
length	½ in (12 mm)
Melt point	325°F (160°C)
Electrical Conductivity	low
Water absorption	negligible
Acid and Alkali Resistance	Excellent

* Technical information of PSI Fiberstrand 100 were provided by Euclid Chemical Company.

3.2.6 High Range Water Reducing Admixture

A superplasticizer based on sulfonated melamine formaldehyde condensates, which is known commercially as Plastol 5000 was used throughout this investigation as a high range water-reducing admixture; conforming to ASTM C 494, Type F admixture and AASHTO M 194 Type F admixture specifications. The superplasticizer used throughout

this study brought from Euclid Chemical Company. The HRWRA was used to produce SCC by increasing the workability and strength while maintaining a constant w/c.

3.2.7 Air Entraining Admixture

The air entrains admixture was used in the research is known commercially as Eucon AEA 92-S from Euclid Chemical Company.

3.3 Mixing Procedure and Mix Proportions

For SCC control mixtures, both fine and coarse aggregates were placed in the mixer and mixed for 30 seconds and then stopped. After that, 1/3 of the mixing water, which was well mixed with AEA were added to the aggregate and mixed for another 30 seconds. The mixer was again stopped, and the cementitious materials were added. Next, the mixer was restarted, and the remaining 2/3 of water was slowly added. After three minutes, the mixer was stopped and the batch left to rest for three minutes. The mixer was restarted, the estimated HRWRA was added and the concrete was mixed for approximately three minutes. For mixing FR-SCC mixtures, the same procedure was used except that the measured fibers were added at the end and additional HRWRA was added to achieve the required fresh properties. Once this had been achieved, the fresh properties tests were conducted.

The proportions of the SCC mixtures were based on a mixture design that was carried out by Brown et al., [2010] with modifications. The water to cement ratio (w/c) was 0.425 for all SCC and FR-SCC for comparison purposes. The details of mixture design and proportions are listed in Table 3.8.

Table 3.8 Mix Proportions for One Cubic Yard of SCC and FR-SCC Mixtures

Mixture	Composition								
	Cement, lb	SL or SF, lb	Total Binder Weight, lb	Water, lb	w/c	Coarse Aggregate (#8), lb	Fine Aggregate (Sand), lb	AEA, oz./cwt	HRWRA, oz./cwt
35SL	439	236	675	287	0.425	1436	1436	0.5	7.0
35SL25S									7.5
35SL50S									8.5
35SL15P									10.0
35SL20P									11.0
10SF	608	68	675	287	0.425	1436	1436	0.5	8.5
10SF25S									12.3
10SF50S									22.0
10SF10P									17.2
10SF15P									26.5

3.4 Testing of Fresh Concrete

3.4.1 Slump Flow Test

The Slump flow test was conducted in accordance with ASTM C1611. A sample of freshly mixed concrete is placed in a mold either in the upright or inverted position as shown in Figure 3.4. The concrete was placed in one lift without tamping or vibration. The mold was raised, and the concrete is allowed to spread. After spreading ceases, two diameters of the concrete mass were measured in approximately orthogonal directions. Slump flow is the average of the two diameters.



Figure 3.4 Slump Flow Test

3.4.2 J-Ring

The J-Ring test was carried out in accordance with ASTM C1621. A sample of freshly mixed concrete was placed in a mold, either in the upright or inverted position that is concentric with the J-Ring (Figure 3.5). The concrete then was placed in one lift without tamping or vibration. The mold was raised, and the concrete was allowed to spread through the J-Ring (Figure 3.6). After spreading ceases, two diameters of the concrete mass were measured in approximately orthogonal directions. J-Ring flow is the average of the two diameters. The test is repeated without the J-Ring to obtain the slump flow. The difference between the slump flow and J-Ring flow is an indicator of the passing ability of the concrete.



**Figure 3.5 J-Ring Test Setup with
Inverted Cone**



Figure 3.6 J-Ring Flow

3.4.3 Modified L-box

A modified L-box was used by inserting single rebar in the middle instead of three rebars as shown in Figure 3.7. With the gate closed, the vertical column of the L-box was filled in one lift (no rodding or other consolidation). The gate was lifted and the SCC flows through the rebar obstructions and into the horizontal portion of the L-box. The filling ability is described by the ratio of the concrete height at the end of the horizontal section (h_2) to the height at the beginning of the horizontal section (h_1). Passing ability was indicated by visual inspection of the area around the bars – with an even distribution of aggregate indicating good passing ability.

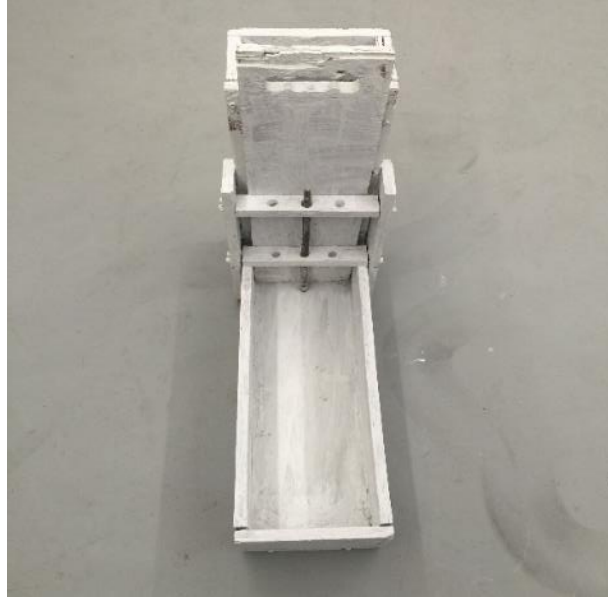


Figure 3.7 Modified L-box Test

3.4.4 Air Content

The air content test was carried out in accordance with ASTM C231 using Type – B pressure meter. This method is for normal concrete and it was used for SCC and FR-SCC. The designed air content was 6%. The used pressure meter is shown in Figure 3.8.\



Figure 3.8 Vertical Air Chamber

3.5 Testing of Hardened Concrete

3.5.1 Compressive Strength Test

The compressive strength test was made according to ASTM C 39, using 4X8 in cylinders. The compressive strength cylinders were tested using a standard testing machine with a capacity of 1 Million pounds as shown in Figure 3.9. The loading was applied at a rate of 4000 lbs each 9 seconds. The average of three specimens was recorded for each testing age.



Figure 3.9 1-Million lbs. Forney Testing Machine.

3.5.2 Splitting Tensile Strength Test

The splitting tensile strength test was carried out in accordance with ASTM C496. Cylinders of 4 in diameter and 8 in height were used and tests were performed using a standard testing machine at a rate of 100 lbs per second. Figure 3.10 shows the placement of the test cylinder in the machine. The average of three cylinders was taken at each test. The following equation gives the splitting tensile strength:

$$f_t = \frac{2P}{\pi dL} \quad \text{ASTM C496 [2011]} \quad (3.1)$$

Where

f_t = splitting tensile strength, (psi)

P = maximum applied load, (lbs)

d = diameter of the specimen, (in)

L = length of the specimen (in)



Figure 3.10 Splitting Tensile Test Setup.

3.5.3 Flexural Strength Test

This test was carried out on 4×4×16 in prism specimens in accordance with ASTM C78, using MTS flexural strength test machine and the setup shown in Figure 3.11. The theoretical maximum tensile stress reached in the bottom fiber of the test beam is known as the modulus of rupture. The fracture occurs within the central one-third of the beam for all specimens; therefore, the modulus of rupture was calculated using the following formula:

$$f_r = \frac{PL}{bd^2} \quad \text{ASTM C78 [2015]} \quad (3.2)$$

Where

f_r = modulus of rupture, (psi)

P = maximum applied load, (lbs)

L = span length, (in)

d = depth of the specimen, (in)

b = width of the specimen, (in)

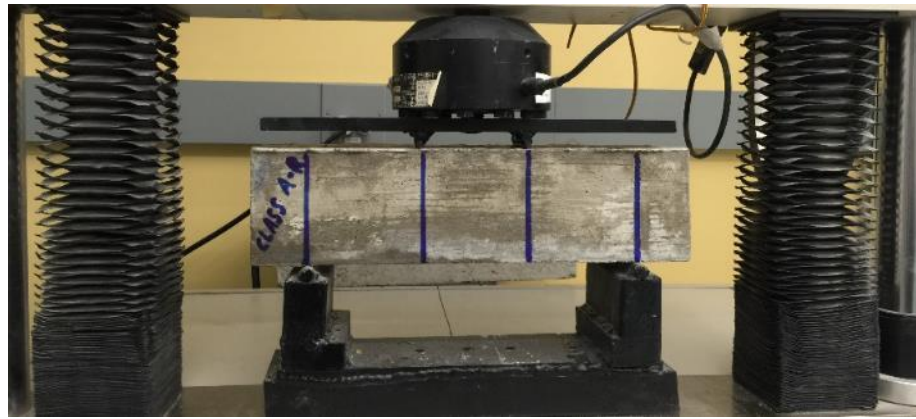


Figure 3.11 Flexural Strength Test Setup.

3.5.4 Static Modulus of Elasticity Test

Based on ASTM C469, the static modulus of elasticity was conducted on 4x8 inch cylinder specimens. In this test, the specimen is loaded up to 40 percent of the ultimate compressive strength. Hence, the compressive strength was required before starting with the test. The load and deformation were recorded manually at regular intervals. The modulus of elasticity can be determined by plotting the strains against the stresses where the slope represents the modulus of elasticity. Figure 3.12 shows the setup of the test.



Figure 3.12 Static Modulus of Elasticity Test Setup

3.5.5 Length Change (Free Shrinkage) Test

This test was conducted according to ASTM C157. According to the standard, three concrete specimens measured 3x3x10 in. were needed to be sampled. Prior to cast the specimens, steel gauge studs were screwed into the plates at each end of the mold. After demolding the specimens, they were moist cured for 14 days and then moved to an environmental chamber. At each age of test, the length of the reference bar, as well as the distance between two gage studs, is measured using a length comparator as shown in Figure 3.13. The free shrinkage strain can be obtained by dividing the change in length by the original length.



Figure 3.13 Length Change Test Setup.

3.6 Compatibility and Bond Strength Tests

These two tests were performed to investigate the compatibility and bond strength of FR-SCC best performance mixtures with the substrate concrete. The samples of these tests were casted into two parts. The first part was casting the concrete substrate using Class A concrete. Class A concrete mixture designed by a local concrete supplier (Clayton Company) and modified by the author. The mixture design is shown in Table 3.9, while the engineering properties are shown in Table 3.10. The concrete mixture was designed to give the 28-day characteristic compressive strength of 4500 psi. The purpose of choosing Class A in order to simulate the existing structures' concrete. The second part was applying the repair and then testing the samples at 1, 3, and 28 days after applying the repair. The selected mixtures and the number of samples are shown in Table 3.11

Table 3.9 Mixture Design for the Substrate

Material	Details	Standards
Cement	Essorce	Type I ASTM C150
Aggregate	Clayton Sand as a fine aggregate Weldon #57 as a course aggregate	ASTM C33 ASTM C33
Admixture 1	Setcon 6A, Air-Entraining Admixture made by Great Eastern Technologies	ASTM C260
Admixture 2	Polystrong HP, Mid-Range Water Reducer Admixture made by Great Eastern Technologies	Type A & F ASTM C494
Admixture 3	Chestrong R, Mid-Range Water Reducing Retarding Admixture made by Great Eastern Technologies	Type D ASTM C494
Mix Proportions		
Cement (lbs)	611	
Sand (lbs)	1275	
Stone (lbs)	1800	
Water (gal)	31	
W/C	0.42	
Admix (ozs)	4.9	
Admix (ozs)	24.4	
Admix (ozs)	***	
Slump (in)	5-7	
Air (%)	6 +/- 1.5	
*** When retarder is required, add (Admix 3) at a rate of 2 to 5 oz per 100 lbs. of cementitious as required.		

Table 3.10 Class A Concrete Strength Results (Average of Three samples)

Property \ Age (Day)	1	3	28
Compressive Strength (psi)	3718	4498	5653
Splitting Tensile Strength (psi)	362	434	459
Modulus of Rupture (psi)	334	411	603
Modulus of Elasticity (ksi)	4121	4276	4591

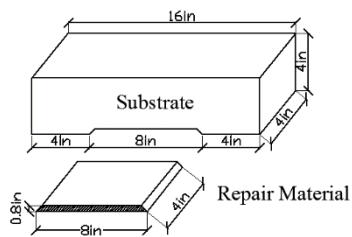
Table 3.11 Selected Mixtures and Number of Samples for Compatibility and Bond Tests

Concrete Mixtures \ Tests	Third Point Loading Composite Prism 1, 3, and 28 days after repair	Bond Strength Test 1, 3, and 28 days after repair
Class A(control)	9	9
10SF25S	9	9
10SF50S	9	9
10SF10P	9	9
10SF15P	9	9
35SL25S	9	9
35SL50S	9	9
35SL15P	9	9
35SL20P	9	9
No. of samples	162	

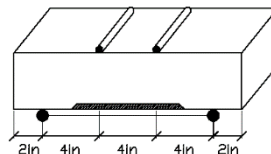
3.6.1 Third Point Loading Compatibility Test

The concrete prisms 16 in. length with a cross-section of 4 in. by 4 in. was casted in accordance with ASTM C 78. The composite prism was fabricated for evaluation of the compatibility of repair material with substrate concrete to compare to the same dimensional

prisms as the control specimen with the exception of a wide-mouthed notch 4 in. length x 4 in. width x 0.8 in. thick casting into the bottom of the composite prism (Figure 3.14a). After demolding specimens, the prisms were moist cured for 28 days (Figure 3.14b), and then the wide-mouthed notch areas were textured using a dry brushing. The rough surface textured substrate specimens were air-dry cured for 7 days before batching the notched area with the repair FR-SCC materials. The composite sections were demolded after 24 hours and cured in water for additional 28 days. After completion of the curing, the composite sections were tested in a set up for the third point loading test in accordance with ASTM C78 as shown in Figure 3.15.



a) Dimensions



b) Curing of Substrate samples

Figure 3.14 Third Point Loading Compatibility Test

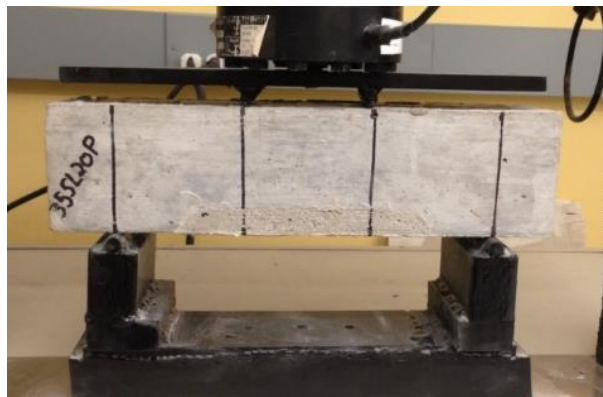
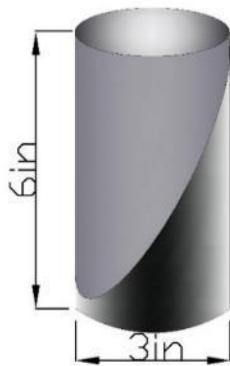


Figure 3.15 Test Setup for Compatibility Test

3.6.2 Bond Strength Test

The bond strength of the repair materials was determined in accordance with ASTM C882. The repair material was bonded to a substrate concrete specimen on a slanted elliptical plane inclined at 30° angle from vertical to form a 3 in. by 6 in. composite cylinder in Figure 3.16. In order to get that elliptical shape, 3 in. by 6 in. full cylinders were casted then cut by the saw. Before bonding the repair material to the substrate concrete, the slanted surface of the substrate concrete specimen was cleaned and dried. The curing procedure used was according to ASTM C882 and as explained in the third point loading composite prism test. The test is performed by determining the compressive load required to fail the composite cylinder and the bond strength was calculated by the maximum applied load divided by the area of slant surface.



a) Dimensions



b) Test Setup for Bond Test

Figure 3.16 Slant Shear Bond Strength Test

3.7 Flexural Strength Test for Full-Scale Beams

Ten full-scale beams were cast to study the flexural behavior of the FR-SCC repaired beam. Eight of these beams were partially casted and repaired with the selected FR-SCC mixtures, while the other two beams were cast as control beams.

3.7.1 Preparing the Beams

Ten wood formworks and steel cages were made as shown in Figure 3.17. Formworks were constructed using $\frac{3}{4}$ in thick plywood forming a rectangular section with 132 in long. The formwork was coated with three layers of polyurethane to protect the surface from water in concrete and to achieve a smooth finish to spot during the test easily. Before pouring concrete, the formwork was thoroughly cleaned with an air compressor to avoid any dust or particles on the surface. The sensors installation has been done according to the strain gauges' manufacturer procedure as demonstrated in Figure 3.18. The duct tape was applied to keep the main reinforcement rebar and apart from shear stirrups clean and ready for the repair process as shown in Figure 3.19.



a) Wood Forms



b) Reinforcement Cages

Figure 3.17 Making the Wood Forms and Reinforcement Cages



Figure 3.18 Installed Strain Gauges



**Figure 3.19 Covering the Rebars with
Duct Tape Protected by M-COAT J**

3.7.2 Casting and Curing of the Substrate

Two control beams and the substrate of the eight other beams were cast using a Class A concrete mixture provided by the Clayton Company as shown in Figure 3.20. The mix design and the strength test results of Class A concrete were presented previously in Table 3.9 and Table 3.10, respectively. Immediately after pouring and vibrating the substrate concrete, a surface retarder was applied to delay the setting of the surface of the substrate as shown in Figure 3.21. Beams were covered with a plastic sheet till the next day, and then a water stream was applied to remove some of the mortar and expose the aggregate to ensure a good bond of the substrate with the repair material as shown in Figure 3.22. The duct tape was removed as shown in Figure 3.23 and the beams were cured using wet burlaps for 7 days (Figure 3.24) and then continued to be air cured inside the lab until the day of repair.



a) Pouring the Concrete



b) Clayton Concrete Truck Delivering the Concrete

Figure 3.20 Casting the Substrate for the Eight Beams and the Two Control Beams



Figure 3.21 Applying the Surface Retarder



**Figure 3.22 Stream Water for Surface Roughness to Expose the Aggregate to
Ensure a Good Bond of the Substrate with the Repair Material**



Figure 3.23 Removing the Duct Tape



Figure 3.24 Curing of the Substrate

3.7.3 Repairing and Curing

The day before repairing, the rebars were cleaned from any rust as illustrated in Figure 3.25 and then the substrate surfaces were cleaned from any dust and wet to get a saturated surface dry surface. After applying the repair, samples were covered with plastic sheet immediately in order to avoid any plastic shrinkage. After 24 hours, samples were carefully demolded and wet burlap cured for 1 day as shown in Figure 3.26.

After 48 hours from the day of the repair, the beam was loaded in the machine, painted with whitewash, side divided into grids, and setup installed as shown in Figs. 3.27 and 3.28. After that, the beams were tested with an age of 3 days from applying the repair.



Figure 3.25 Cleaning the Rebars from any Rust



Figure 3.26 Curing the Repaired Beam

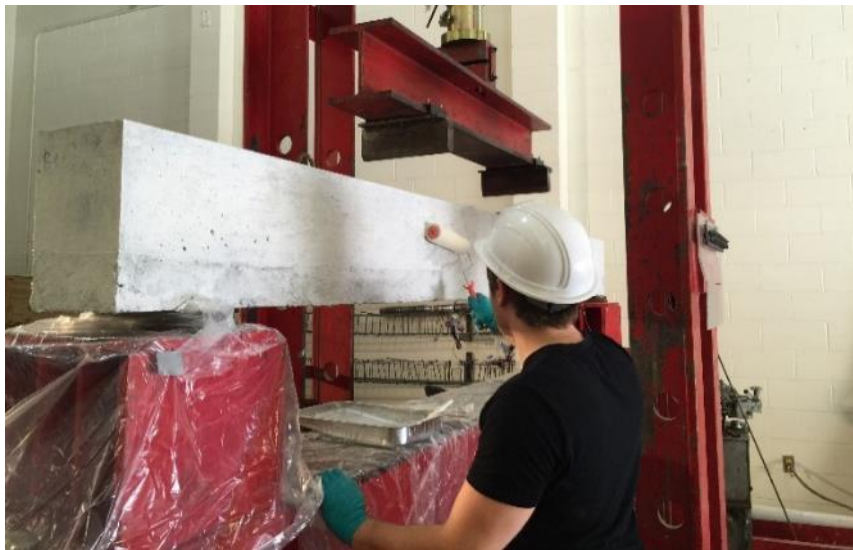


Figure 3.27 Painting the Beam with Whitewash

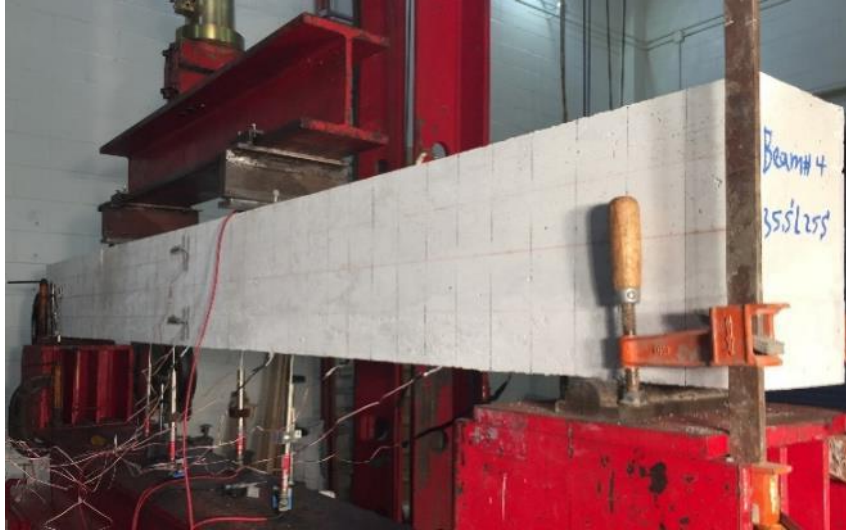
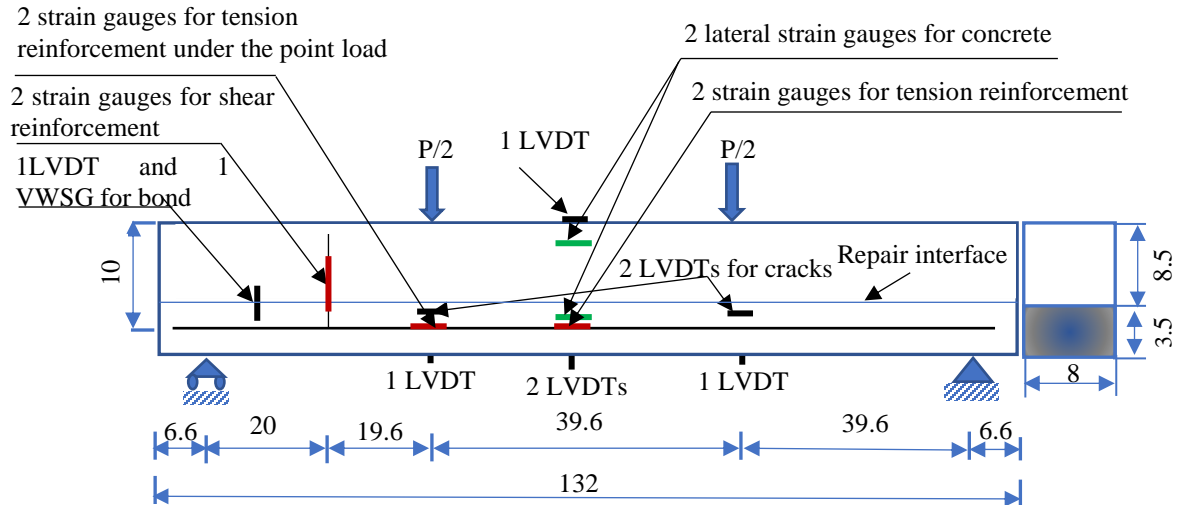


Figure 3.28 Installing the Setup

3.7.4 Beam Flexural Tests Setup

Various types of sensors, such as foil strain gauge and linear variable differential transformer (LVDT), were instrumented to record the structural behavior using a simple beam with third-point loading. Foil strain gauges for steel and concrete and the LVDTs were installed at different selected locations. The test setup and instrument locations are shown in Figure 3.29 while the details are as follows:

- 1- Two LVDTs at mid-span and at each side of the beam to monitor the maximum deflection. These LVDTs manufactured by RDP Group, type DCTH1000A.
- 2- Two high-accuracy LVDTs type DCTH400AG (linearity error $< \pm 0.5$ based on full scale) to control the crack width of the 2 first (supposed major) cracks at mid-span of the beam as shown in Figure 3.30.



*All dimensions are in inches.

Figure 3.29 Test Setup and Instrument Locations

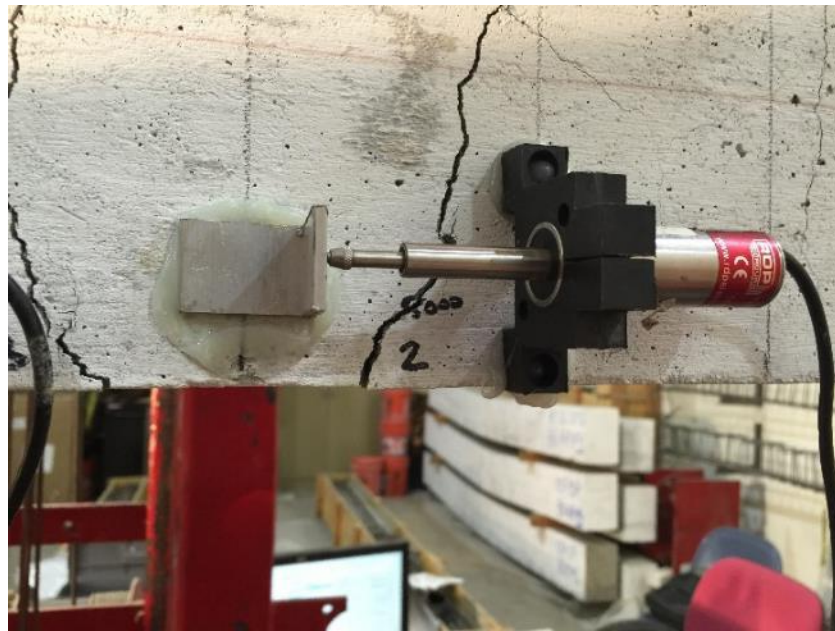


Figure 3.30 LVDT Installed to Measure Crack Width

3- Two LVDTs type DCTH1000A at each third span to control the deflection profile along the beam (for quality control). Figure 3.31 shows the types of the LVDTs used throughout this work.

4- One LVDT type DCTH1000A fixed on the top surface of the beam at mid-span to measure the concrete compressive strains as shown in Fig 3.32.

5- One small LVDT and one Vibrating Wire Strain Gauge (VWSG) to control a possible de-bond between the repair material and the substrate near the support as shown in Figure 3.33. The VWSG used is a Geokon Model 4000, shown in Fig 3.34, while the LVDT is type DCTH400AG. The VWSG is basically consist of a metal tube attached between two mounting blocks. Inside the tube, a vibrating steel wire. When the sensor encounters a small compression or tension, the frequency changes. The resonant frequency is measured by plucking the wire using an electromagnetic coil connected through a signal cable to Data Acquisition System (DAS) which measures the frequency and convert it to microstrains. The VWSG attached to the concrete by bonding the mounting blocks using high strength epoxy structural adhesive known as Devcon.

6- Two electrical strain gauges glued to the longitudinal tensile reinforcing bars at mid-span to measure the tensile strains (using C2A-06-125LW-120 made by Micro-Measurements).

7- Two electrical strain gauges glued to the longitudinal tensile reinforcing bars at third-span under one of the point loads to measure the tensile strains (using C2A-06-125LW-120 from Micro-Measurements).

8- Two electrical concrete strain gauges glued to different depths of the beam at mid-span for quality control (strain distribution along the depth of the beam); (using C2A-06-

20CLW-120 from Micro-Measurements) as shown in Figure 3.35. The C2A-06-125LW-120 and C2A-06-20CLW-120 strain gauges are shown in Fig 3.36.

9- One load cell manufactured by Geokon Company with a maximum capacity of 400K lbs to measure the applied load.

10- One CR3000 micrologger made by Campbell Scientific Inc. was used to collect the data during a test at an interval of 40 milliseconds. The micrologger consists of Twenty-eight single-ended (14 differential) channels. It was programmed to collect the data from all the strain gauges, LVDTs, and the load cell. A view of the CR3000 micrologger is shown in Figure 3.38.



Figure 3.31 LVDT Type DCTH1000A (left) and DCTH400AG (right)



Figure 3.32 LVDT at the Top for Measuring the Compressive Strain



Figure 3.33 VWSG and the LVDT for Deboning Measurement

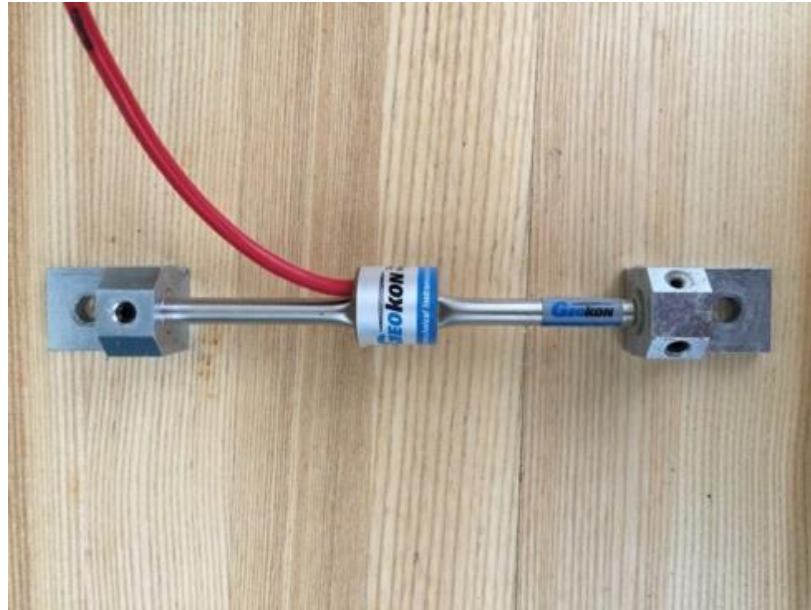


Figure 3.34 Geokon Model 4000 VWSG Used for Deboning Measurement

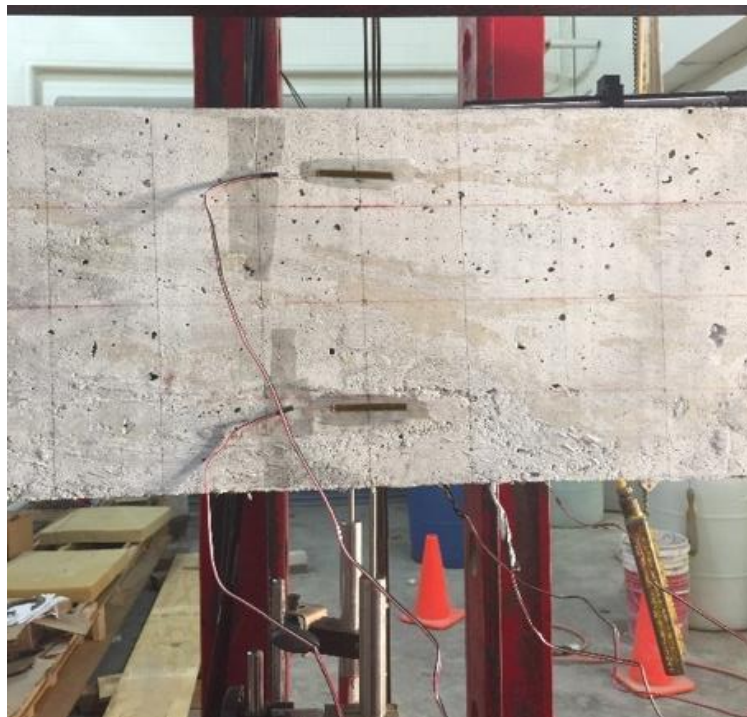


Figure 3.35 Concrete Strain Gauges



Figure 3.36 Vishay 120 Ohm Foil Strain Gauge C2A-06-20CLW-120 (left) and C2A-06-125LW-120 (right)



Figure 3.37 LVDTs Setup

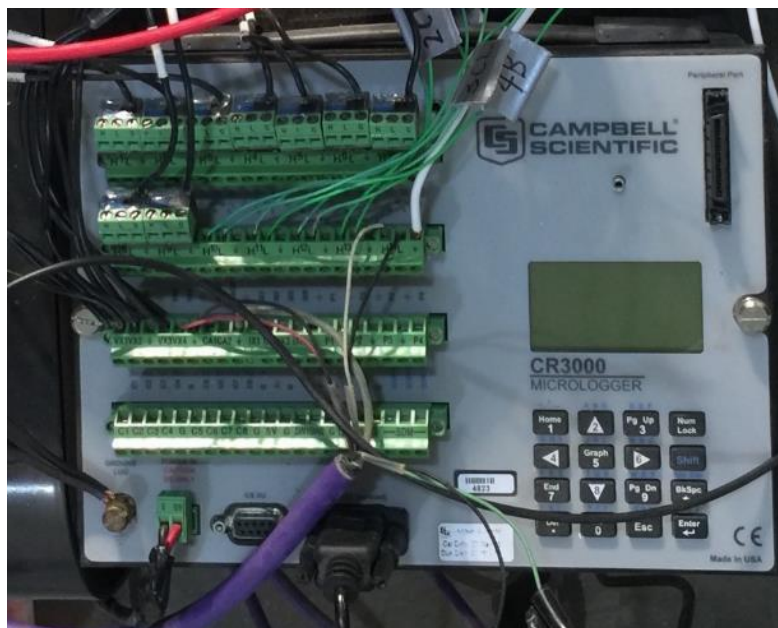


Figure 3.38 CR3000 Micrologger Used

CHAPTER 4 EXPERIMENTAL RESULTS

4.1 Introduction

This chapter presents the experimental results including fresh and hardened properties results of SCC and FR-SCC mixtures at the beginning. The fresh properties include the slump flow test, T 20, Visual Stability Index (VSI), J-ring, modified L-box, and air content. While the hardened properties are compressive strength, splitting tensile strength, flexural strength, modulus of elasticity, and free shrinkage. Bond strength and compatibility results will be presented next, followed by the results of the full-scale beams flexural strength test. The last includes the load versus deflection, load versus strain, cracking and ultimate loads, and the mode of failure and cracking behavior.

4.2 Fresh Concrete Results

The fresh test properties of the optimize mixtures are shown in Table 4.1. The PPF exhibited problems in the passing ability of the fresh concrete requirements at higher volumes of 0.2 and 0.25, and especially with SF. The minimum slump flow value was 21 inches; whereas, the maximum obtained was 25 inches. During the slump flow test, the T20 was measured. The results ranged between 4 and 8 seconds. It is well known that the viscosity increases with the increase of fiber content. For repair purposes, a low viscosity (high workability) is desired with a T20 value around 5 seconds. After measuring the slump flow test, the VSI was reported. Most of the mixtures have shown high stability with no sign of bleeding or segregation (VSI=0). For 35SL25S and 35SL50S mixtures, a halo of mortar was seen on the outer edge of the concrete slump flow (VSI=1). A value for VSI equal to 1, is considered a high-quality SCC or FR-SCC. The J-Ring test is a good indicator

for passing ability of SCC or FR-SCC. The difference between the slump flow and the J-ring readings is another indicator for passing ability. For SCC, a difference of 1 inch refers to no visible blocking and adequate passing ability. The difference in flow has increased with the increase in fiber content, and hence, it is not recommended to use the mixtures with high fiber volume content in repairing the very congested reinforcement areas unless a partial compaction will be applied. Khayat et al. [2014] recommended using a modified J-ring of 8 bars instead of 16 for FR-SCC. Regarding the air content test results, all mixtures have shown an air content equal or greater the designed air content which is 6%. It is well known that air entraining in concrete is important for its durability against freeze and thaw and a value of 6% or greater is desired. The modified L-box test results showed blocking ratio values greater than 0.8 which is excellent passing ability.

Table 4.1 Fresh Concrete Test Results

Mixture	Fresh Properties						
	Slump Flow, inch	T20, s	VSI	J-Ring, inch	Modified L-Box, h2/h1	Air Content, %	Difference in Flows*
35SL	23.5	4.0	0	22.5	1.00	7.0	1.0
35SL25S	21.5	5.5	1	20.0	1.00	6.5	1.5
35SL50S	22.0	6.5	1	19.0	0.90	6.5	3.0
35SL15P	23.5	4.5	0	19.0	0.90	6.5	3.5
35SL20P	23.0	4.5	0	18.0	0.80	6.0	5.0
10SF	25.0	5.0	0	21.5	1.00	6.5	3.5
10SF25S	25.0	5.3	0	21.0	0.95	6.5	4.0
10SF50S	24.0	6.0	0	19.0	0.93	6.0	5.0
10SF10P	23.0	5.0	0	18.0	0.90	6.5	5.0
10SF15P	21.0	8.0	0	17.0	0.80	6.0	4.0

*Difference in flow= Slump flow – J-Ring

4.3 Hardened Concrete Results

4.3.1 Compressive strength

The compressive strength development at various curing ages for all types of concrete are presented in Figure 4.1 and Table 4.2. At 28 days, the compressive strength values for the SCC and FR-SCC were between 5316 and 9130 which is greater than the designed compressive strength (5000 psi). Results demonstrated that, in general, all concretes exhibited a continuous increase in compressive strength with the increase in the age. Results also showed that the addition and increase of fiber content slightly increase the compressive strength. Mixtures with SF showed higher compressive strength compared to mixtures contain SL.

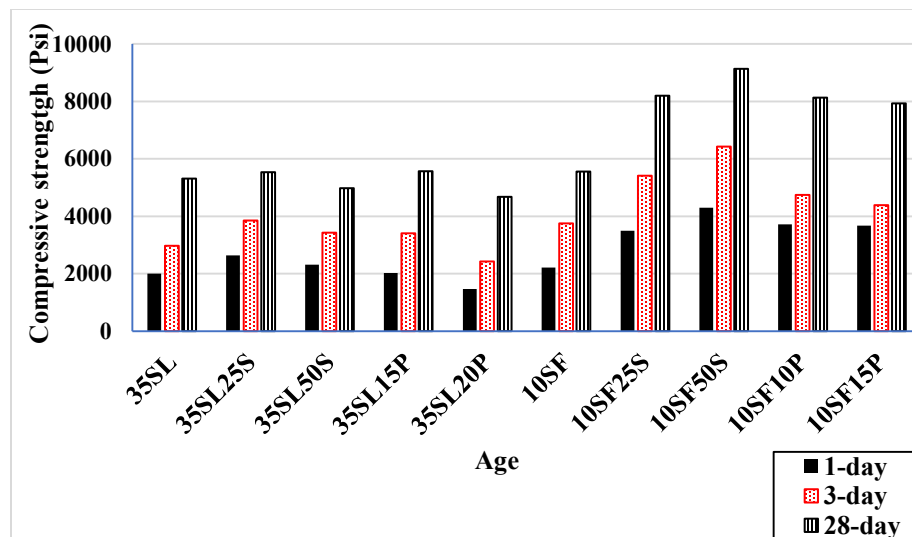


Figure 4.1 Compressive Strength at Different Ages

Table 4.2 Compressive Strength at Different Ages

Age-day	Repair Material	Compressive Strength, psi	COV (%)	Ratio $f'_c(t)/f'_c(28)$	μ	SD
1	35SL	2006	2.9	0.38	0.42	0.06
	35SL25S	2633	2.6	0.48		
	35SL50S	2309	2.8	0.46		
	35SL15P	2020	1.6	0.36		
	35SL20P	1468	3.8	0.31		
	10SF	2216	0.6	0.40		
	10SF25S	3490	2.9	0.43		
	10SF50S	4300	2.1	0.47		
	10SF10P	3722	0.7	0.46		
	10SF15P	3676	1.7	0.46		
3	35SL	2972	4.5	0.56	0.62	0.07
	35SL25S	3848	2.9	0.69		
	35SL50S	3424	3.1	0.69		
	35SL15P	3410	0.8	0.61		
	35SL20P	2426	3.1	0.52		
	10SF	3750	1.5	0.68		
	10SF25S	5414	1.8	0.66		
	10SF50S	6430	3.3	0.70		
	10SF10P	4748	2.1	0.58		
	10SF15P	4390	2.3	0.55		
28	35SL	5316	0.6	1.00	-	-
	35SL25S	5537	6.8	1.00		
	35SL50S	4976	2.8	1.00		
	35SL15P	5573	5.2	1.00		
	35SL20P	4671	2.4	1.00		
	10SF	5553	2.2	1.00		
	10SF25S	8201	0.8	1.00		
	10SF50S	9130	1.5	1.00		
	10SF10P	8134	2.9	1.00		
	10SF15P	7935	2.1	1.00		

4.3.2 Splitting Tensile Strength

The effect of the curing ages on the splitting tensile strength for all types of concrete is presented in Figure 4.2 and Table 4.3. The results indicated that, in general, all types of concrete exhibited continuous increase in splitting tensile strength with time. The addition of steel fibers to concrete increases the splitting tensile strength of concrete significantly. The percentage increase in splitting tensile strength was found to be increased with the increase in fiber content. This behavior is attributed to the mechanism of steel fibers in arresting crack progression. Where the presence of fibers in concrete restrains the development of internal microcracks and thus contributes to an increased tensile strength [Kumar et al., 1993]. Thus, the increase in fiber content leads to increase the tensile strength of concrete.

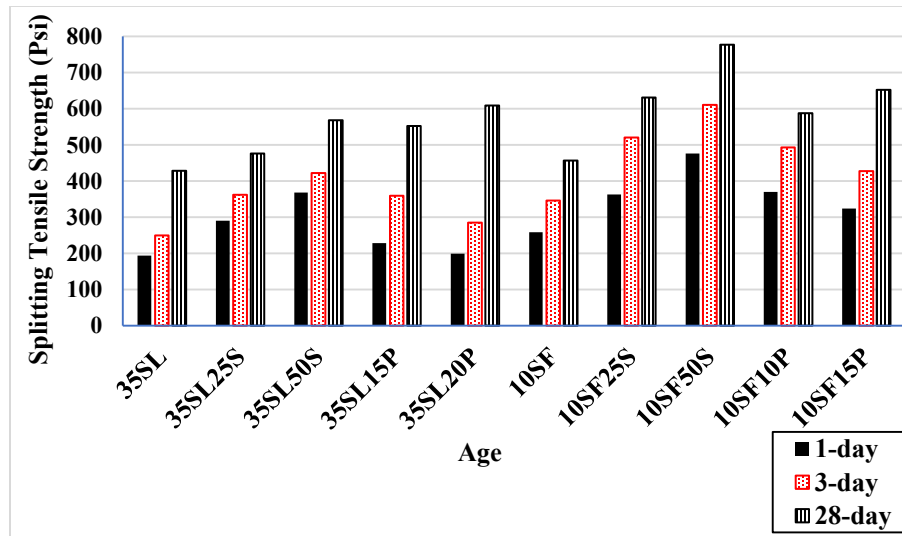


Figure 4.2 Splitting Tensile Strength at Different Age

Table 4.3 Splitting Tensile Strength at Different Ages

Age-day	Repair Material	Splitting Tensile Strength (T), psi	COV (%)	T(t)/T(28)	μ	SD
1	35SL	194	2.6	0.45	0.53	0.11
	35SL25S	290	3.2	0.61		
	35SL50S	368	2.3	0.65		
	35SL15P	228	6.5	0.41		
	35SL20P	199	4.3	0.33		
	10SF	258	3.1	0.57		
	10SF25S	363	9.8	0.58		
	10SF50S	476	3.9	0.61		
	10SF10P	370	2.3	0.63		
	10SF15P	324	2.2	0.50		
3	35SL	249	1.3	0.58	0.71	0.12
	35SL25S	362	3.2	0.76		
	35SL50S	422	3.1	0.74		
	35SL15P	359	2.6	0.65		
	35SL20P	285	6.1	0.47		
	10SF	346	3.7	0.76		
	10SF25S	520	6.3	0.82		
	10SF50S	610	4.1	0.79		
	10SF10P	493	5.1	0.84		
	10SF15P	427	4.6	0.65		
28	35SL	428	2.0	1.00	-	-
	35SL25S	476	6.8	1.00		
	35SL50S	568	2.5	1.00		
	35SL15P	552	3.2	1.00		
	35SL20P	609	6.1	1.00		
	10SF	456	5.1	1.00		
	10SF25S	631	1.4	1.00		
	10SF50S	777	3.7	1.00		
	10SF10P	587	4.1	1.00		
	10SF15P	652	2.6	1.00		

4.3.3 Flexural Strength

The results of the flexural strength for various types of concrete specimens are presented in Figure 4.3 and Table 4.4. The results indicated that with the progress of curing ages all concrete specimens showed a continuous gain in flexural strength. The modulus of rupture increases with the increase of fiber percentage. This behavior is mainly attributed to the role of steel fibers in releasing fracture energy around crack tips which is required to extent crack growing by transferring it from one side to another side [Teng and Shah, 1986]. The results also showed that mixtures with SF showed better flexural strength than mixtures with SL.

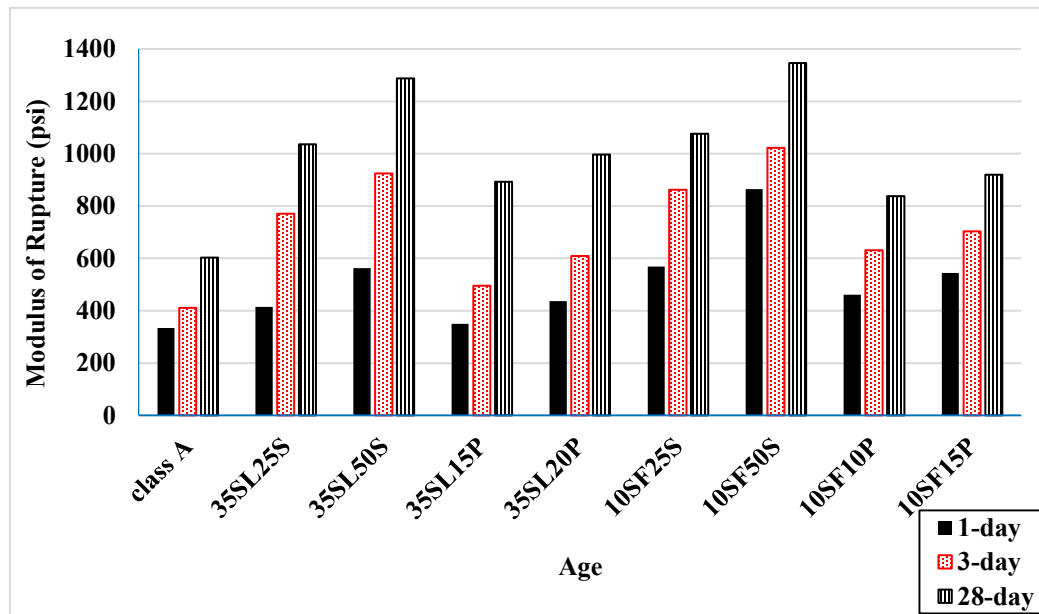


Figure 4.3 Flexural Strength at Different Ages

Table 4.4 Flexural Strength at Different Ages

Age-day	Repair Material	Modulus of Rupture, psi	COV (%)	R(t)/R(28)	μ	SD
1	Class A	334	2.7	0.55	0.50	0.09
	35SL25S	415	3.1	0.40		
	35SL50S	563	3.0	0.44		
	35SL15P	350	2.9	0.39		
	35SL20P	436	1.1	0.44		
	10SF25S	569	2.0	0.53		
	10SF50S	865	2.9	0.64		
	10SF10P	461	3.4	0.55		
	10SF15P	544	1.3	0.59		
3	Class A	411	2.4	0.68	0.71	0.08
	35SL25S	770	2.9	0.74		
	35SL50S	924	6.0	0.72		
	35SL15P	495	8.4	0.55		
	35SL20P	609	1.0	0.61		
	10SF25S	862	1.7	0.80		
	10SF50S	1022	2.8	0.76		
	10SF10P	631	3.1	0.75		
	10SF15P	703	3.7	0.76		
28	Class A	603	1.9	1.00	-	-
	35SL25S	1036	1.0	1.00		
	35SL50S	1288	3.2	1.00		
	35SL15P	892	0.6	1.00		
	35SL20P	977	0.2	1.00		
	10SF25S	1076	7.9	1.00		
	10SF50S	1346	0.6	1.00		
	10SF10P	837	4.1	1.00		
	10SF15P	919	1.5	1.00		

4.3.4 Modulus of Elasticity

The values of modulus of elasticity for various types of concrete at different ages are presented in Figure 4.4 and Table 4.5. Results indicated that all concrete specimens exhibited a continuous increase in the modulus of elasticity values with the development of the ages. The addition of fiber resulted in a slight increase in the modulus of elasticity. SF mixtures showed slightly higher results than SL mixtures. The results also showed that

the elastic modulus has a lower increase than the concrete strength as illustrated in Figure 4.5.

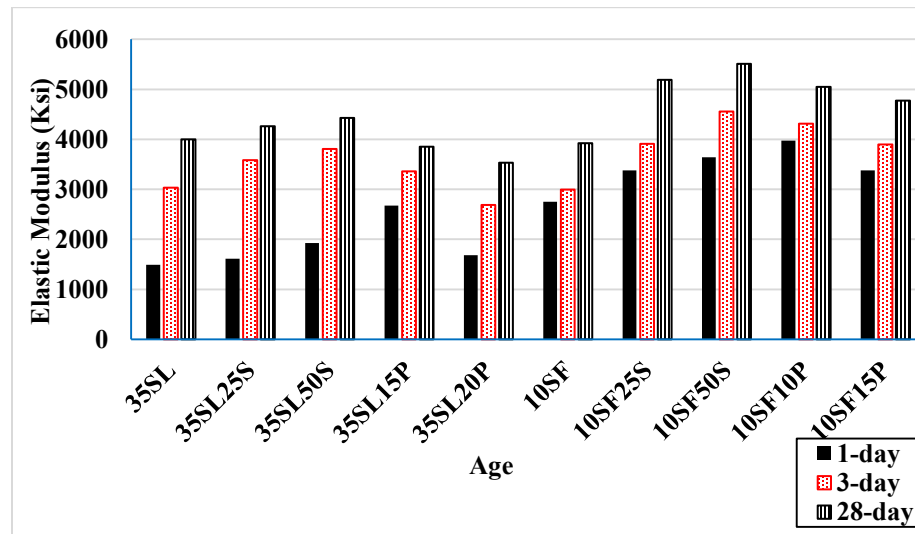


Figure 4.4 Modulus of Elasticity at Different Ages

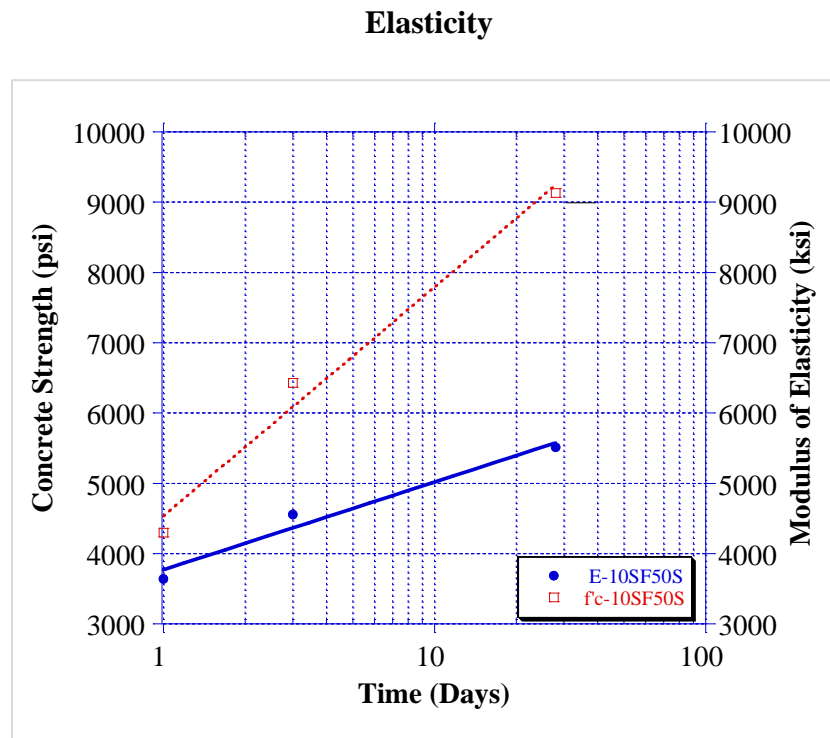


Figure 4.5 Modulus of Elasticity vs Concrete Strength

Table 4.5 Modulus of Elasticity at Different Ages

Age-day	Repair Material	Elastic Modulus, ksi	COV (%)	E(t)/E(28)	μ	SD
1	35SL	1491	0.8	0.37	0.59	0.16
	35SL25S	1614	1.5	0.37		
	35SL50S	1928	0.9	0.44		
	35SL15P	2674	1.4	0.69		
	35SL20P	1683	0.2	0.48		
	10SF	2751	0.7	0.7		
	10SF25S	3377	4.2	0.65		
	10SF50S	3638	0.9	0.66		
	10SF10P	3971	4.8	0.79		
	10SF15P	3376	1.5	0.71		
3	35SL	3034	0.3	0.76	0.81	0.05
	35SL25S	3584	5.7	0.84		
	35SL50S	3809	0.2	0.86		
	35SL15P	3357	1.9	0.87		
	35SL20P	2690	1.2	0.76		
	10SF	2995	1.8	0.76		
	10SF25S	3912	4.6	0.75		
	10SF50S	4558	1.8	0.83		
	10SF10P	4310	3.9	0.85		
	10SF15P	3894	1.2	0.82		
28	35SL	4000	3.2	1.00	-	-
	35SL25S	4258	0.8	1.00		
	35SL50S	4427	0.0	1.00		
	35SL15P	3850	2.6	1.00		
	35SL20P	3534	1.4	1.00		
	10SF	3920	0.2	1.00		
	10SF25S	5192	1.0	1.00		
	10SF50S	5512	3.0	1.00		
	10SF10P	5047	0.9	1.00		
	10SF15P	4776	0.1	1.00		

4.3.5 Free Shrinkage

Figure 4.6 illustrates the free shrinkage test results. Mixtures included SL showed lower shrinkage than mixtures included SF in it. This is mainly attributed to the high fineness of the SF material. The results also demonstrated that the incorporation of both types of fiber reduced the shrinkage significantly comparing with mixtures without fibers. It is good to mention that 35SL50S mixture showed the lowest shrinkage with 37 % reduction comparing to 35SL at 56 days. Emmons et al., 1993 has pointed that if the repair material shows a drying shrinkage exceed of 0.05 and 0.1 % for moderate and high level respectively, an early failure will happen. The drying shrinkage results for the mixtures under study were ranged between 0.0131 and 0.032 % at 28 days which is below the moderate level.

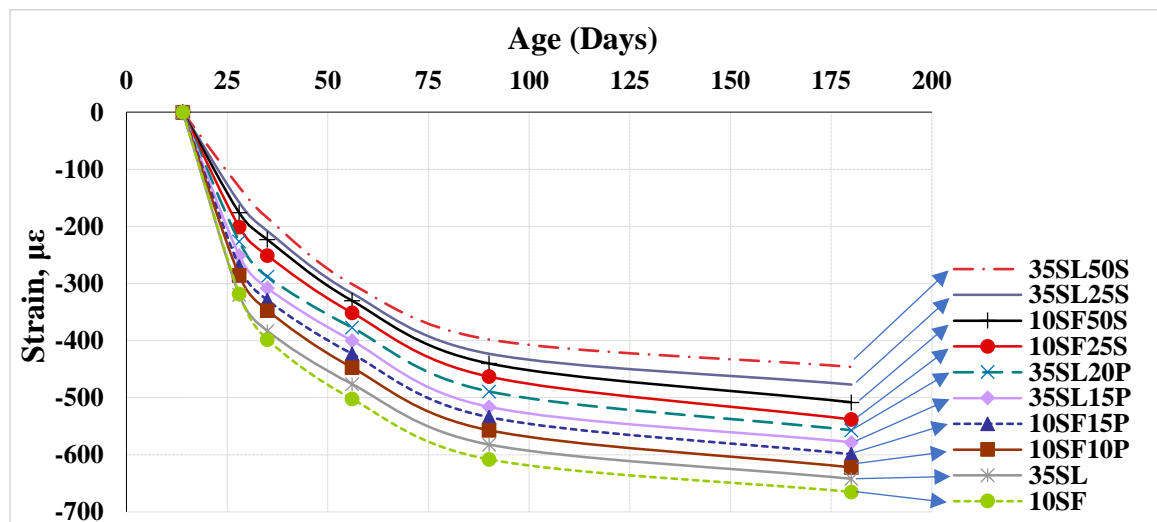


Figure 4.6 Free Drying Shrinkage Behavior for Various Mixtures

4.3.6 Compatibility Test Results

Despite the fact that flexural compatibility is not a standard test, it gives a good indication of how the composite small scale repaired beam behave under flexural loads by

inducing tensile stresses in the repair material. The values of flexural strength compatibility for the various types of concrete at different curing ages are presented in Figure 4.7 and Table 4.6. The substrate which is Class A concrete flexural strength results were 334, 411, and 603 psi for 1, 3, and 28 days, respectively. Results indicate that all composite prisms exhibited higher flexure strength compared with the substrate with a maximum increase of 147, 128, and 104 % at 1, 3, and 28 days, respectively. In general, the failure location was in the middle which indicates a good compatibility. Depending on the point of failure determined through this test, a concrete sample's compatibility with a repair material is determined. Czarnecki et al., 1999 has found that if a failure crack appears through the repair material and the substrate, or through only the substrate, the two materials are compatible. If, however, a failure crack appears through the bonded area between the substrate and repair, the two materials are incompatible Figure 4.8 shows the two types of failure mode observed. The good compatibility of the optimized repair mixtures during this study is mainly due to the low drying shrinkage of these materials.

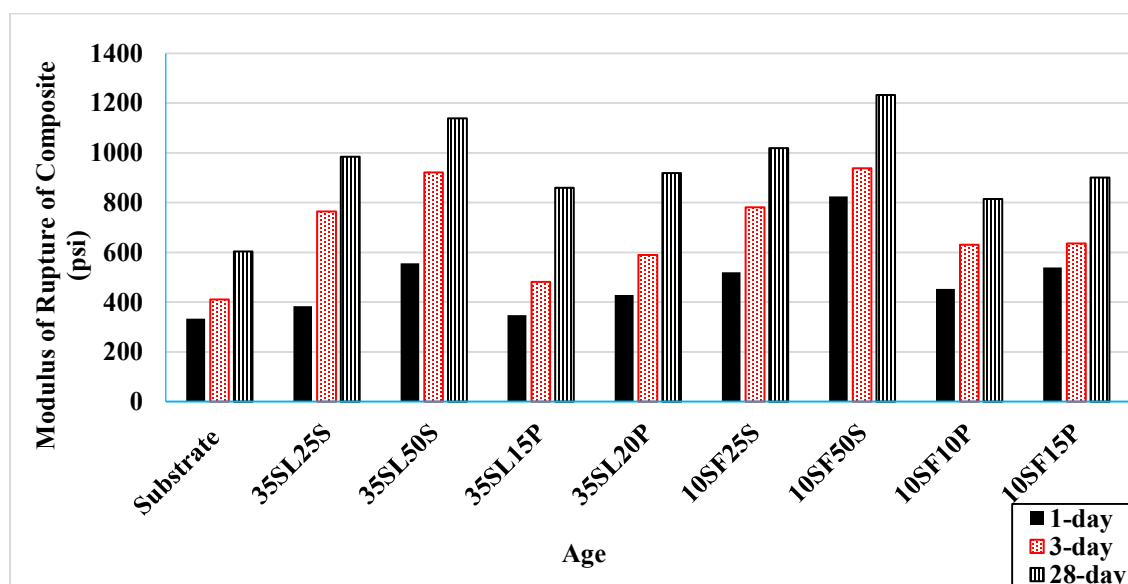
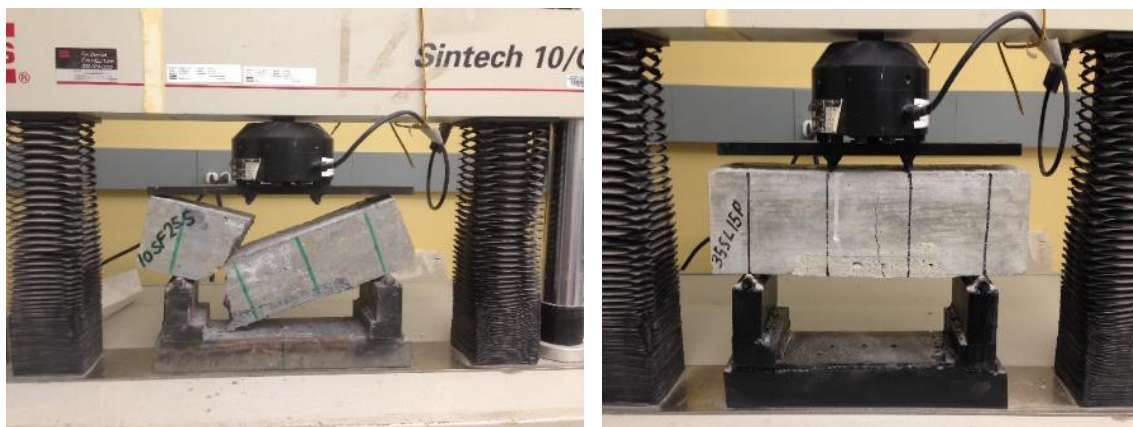


Figure 4.7 Results of Third Point Loading Composite Prism Test

Table 4.6 Results of Third Point Loading Composite Prism Test and Failure**Location**

Age-day	Repair Material	Flexure Strength, psi			Difference, %*	Failure location
		Control (Class A)	Repair Material	Composite		
1	35SL25S	334	415	383	15	Center
	35SL50S		563	556	66	Center
	35SL15P		350	348	4	Center
	35SL20P		436	429	28	Center
	10SF25S		569	520	56	2 Center and 1 Edge
	10SF50S		865	825	147	Center
	10SF10P		461	453	36	Center
	10SF15P		544	539	61	Center
3	35SL25S	411	770	764	86	Center
	35SL50S		924	921	124	Center
	35SL15P		495	481	17	Center
	35SL20P		609	590	44	Center
	10SF25S		862	781	90	2 Center and 1 Edge
	10SF50S		1022	938	128	Center
	10SF10P		631	631	54	Center
	10SF15P		703	636	55	Center
28	35SL25S	603	1036	984	63	Center
	35SL50S		1288	1138	89	Center
	35SL15P		892	860	43	Center
	35SL20P		997	918	52	Center
	10SF25S		1076	1019	69	2 Center and 1 Edge
	10SF50S		1346	1232	104	Center
	10SF10P		837	814	35	Center
	10SF15P		919	901	49	Center

* Difference = $\frac{\text{Composite flexural strength} - \text{substrate flexural strength}}{\text{substrate flexural strength}} \times 100\%$



a) Failure at the Edge

b) Failure at the Center

Figure 4.8 Compatibility Test Failure Mode Observed

4.3.7 Bond Strength Results

The results of the bond test in terms of the slant shear strength for the various types of concrete at 1, 3, and 28 days curing are presented in Figure 4.9 and Table 4.7. Results demonstrated that the increase in the fiber content increased the bond strength for the percentages of fibers under this study. Pattnaik [2006], has proven that the strength ratios governed the mode of failure of the ready mixture repair materials that studied. These ratios are compressive strength ratio and split tensile strength ratio (i.e. strength of repair material/strength of substrate mortar). According to Pattnaik [2006], there are two classes of bond strength depending on the failure mode. If the mode of failure is an interface, an actual bond strength can be determined. Otherwise, a minimum bond strength can be calculated according to ASTM C882.

The strength ratios and the failure modes are also shown in Table 4.7. It was observed that most of the mixtures failed with the substrate and repair mode with compressive strength ratio greater or equal to 0.71. This behavior is mainly due to the high bond strength than the composite materials strength. The second noticed failure mode was

the repair material failure when compressive strength ratio is less or equal 0.62 and splitting strength ratio is relatively high. The last observed failure mode was the interface and repair as in mixture 35SL20P with compressive and splitting tensile strength ratios of 0.39 and 0.61, respectively. In this case, the low compressive strength and splitting tensile for the repair material compared with the substrate led to such failure. Figure 4.10 shows the observed failure mode for the most of the samples were in the substrate and repair which refers a good bond strength.

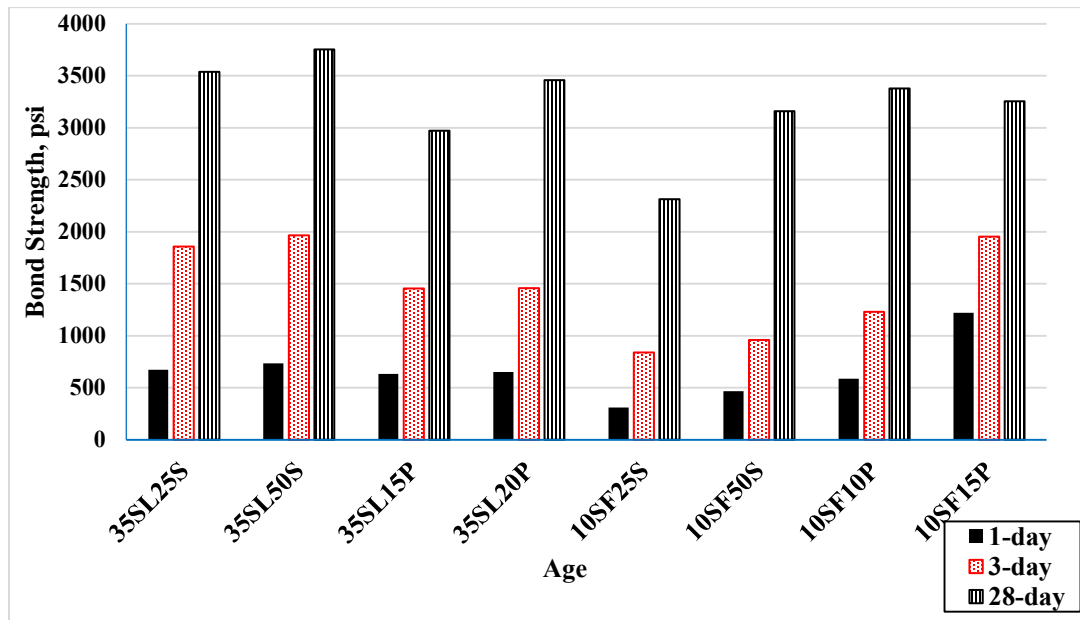


Figure 4.9 Results of Slant Shear, Bond strength Test.

Table 4.7 Results of Slant Shear, Bond Strength Test

Age day	Repair Material	Bond Strength, psi	Compressive Strength Ratio	Splitting Tensile Strength Ratio	Failure Mode
1	35SL25S	672	0.71	0.95	Substrate and repair
	35SL50S	734	0.62	1.20	Repair
	35SL15P	632	0.54	0.75	Repair
	35SL20P	651	0.39	0.61	Interface and repair
	10SF25S	309	0.94	1.11	Substrate and repair
	10SF50S	467	1.16	1.46	Substrate and repair
	10SF10P	587	1.00	1.02	Substrate and repair
	10SF15P	826	0.99	0.90	Substrate and repair
3	35SL25S	1857	0.86	0.84	Substrate and repair
	35SL50S	1964	0.76	1.10	Substrate and repair
	35SL15P	1456	0.76	0.85	Substrate and repair
	35SL20P	1458	0.54	0.75	Repair
	10SF25S	840	1.20	0.84	Substrate and repair
	10SF50S	958	1.43	1.10	Substrate and repair
	10SF10P	1229	1.06	0.85	Substrate and repair
	10SF15P	1953	0.98	0.75	Substrate and repair
28	35SL25S	3539	0.98	0.79	Substrate and repair
	35SL50S	3753	0.88	1.04	Substrate and repair
	35SL15P	2972	0.99	0.86	Substrate and repair
	35SL20P	3458	0.83	0.71	Substrate and repair
	10SF25S	2312	1.45	1.38	Substrate and repair
	10SF50S	3159	1.62	1.69	Substrate and repair
	10SF10P	3378	1.44	1.28	Substrate and repair
	10SF15P	3560	1.40	1.42	Substrate and repair

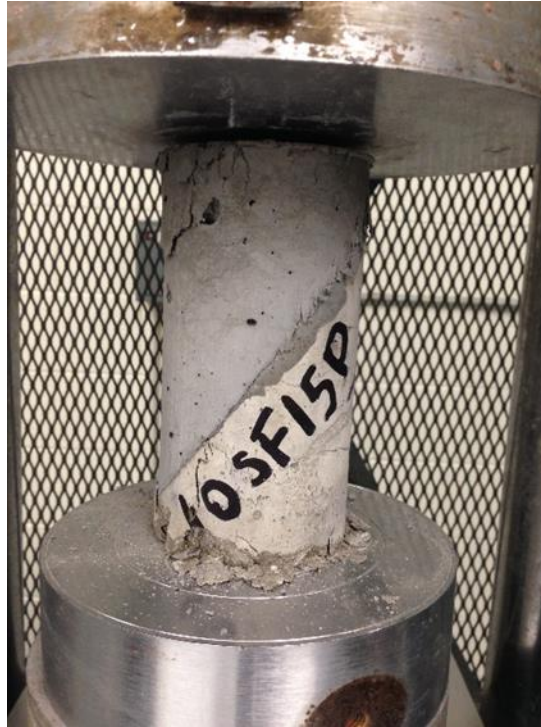
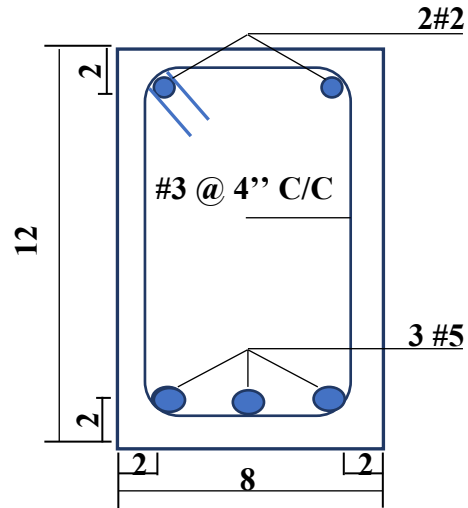


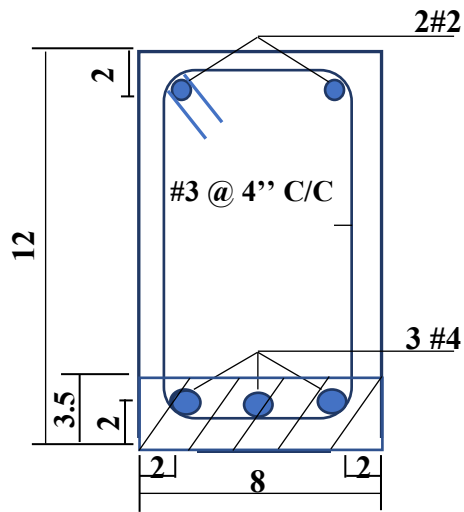
Figure 4.10 Example of the Failure in both Substrate and Repair Material

4.4 Flexural Test Results for Full-Scale Beams

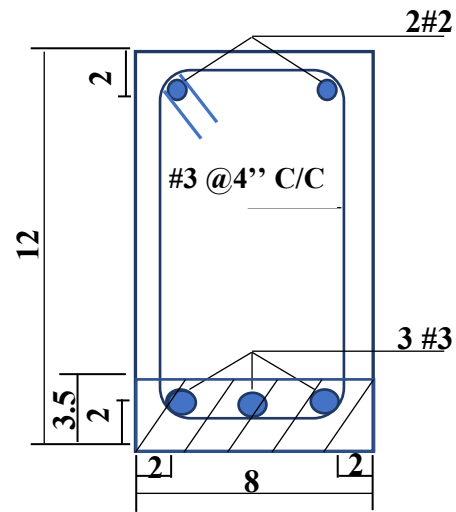
Figure 4.11 shows the beams cross section design details and the corresponding mixtures selected for repair. The main reinforcement for the control beams is #5 while the main reinforcement for the repaired beams were #4 and #3. The reason why the author selected a smaller cross section rebars is to simulate corrosion of 35 % and 65 % for the #4 and #3 rebars respectively.



(a)



(b)



(c)

*All dimensions are in inches

Figure 4.11 Beams Cross Section Design Details and the Corresponding Mixtures

Selected for Repairing:

(a) Class A (control)

(b) 10SF25S, 10SF10P, 35SL25S, and 35SL15P

(c) 10SF50S, 10SF15P, 35SL50S, and 35SL20P

4.4.1 Cracking and Ultimate Loads

Table 4.8 summarizes the crack and ultimate loads for all the tested beams. The flexural cracking load ranged between 4900 and 6000 lbs for repaired, and 4600 and 4700 lbs for the reference control beams. The percent increase in the cracking load compared with the average cracking load for the two control beams is also listed in Table 4.8. Such increase in the cracking load is due to using the FR-SCC that increased the tensile strength supported by the fibers in repaired zone (i.e. tension zone). The beams repaired with STF has shown higher cracking loads than those repaired with PPF. A maximum percentage increase of 29 % was achieved for the beam repaired with 10SF50S. A slight increase in the cracking load was also observed for beams repaired with mixtures containing SF compared with SL. Such increase in the cracking load is mainly due to the higher compressive strength for those repair materials.

The ultimate load ranged between 15,492 and 26,200 lbs for repaired, and 30,000 and 32,000 lbs for the reference control beams. For all tested beams, the flexural crack loads represented 15 % to 37 % of the ultimate load. The reinforcing steel bars continued in irreversible prolongation up to ultimate load level. Depending on their tensile and bond strength (pull out action), fibers contribute to resist tensile stress and arrest the enlargement of the cracks up to the ultimate load. Beams repaired with STF showed higher ultimate load than those repaired with PPF. For example, the ultimate load of the beam repaired with 10SF50S is greater than the ultimate load of the beam repaired with 10SF15P by 22.6 %. The longer length, crimped shape, and higher volume fraction of STF has mainly contributed to such performance. Swamy and Mangat [1974], Swamy and Jojaha [1982],

have proven that fiber type, volume, and geometry significantly affect the compaction and the ultimate load as a result.

Table 4.8 Cracking and Ultimate Loads for the Tested Beams

Beam	Main reinforcement rebar #	Cracking load, lbs	Increase in Cracking Load, %	Ultimate load, lbs
Control 1	5	4700	-	32000
Control 2	5	4600	-	30000
35SL25S	4	5500	18.3	24000
35SL15P	4	4900	5.4	22700
10SF25S	4	5500	18.3	26200
10SF10P	4	5500	18.3	23000
35SL50S	3	5700	22.6	16000
35SL20P	3	5100	9.7	15492
10SF50S	3	6000	29.0	19000
10SF15P	3	5700	22.6	15500

4.4.2 Load – Deflection Relationship

The applied load versus midspan deflection as an average of two LVDTs will be discussed in this section. A tri-linear load-deflection relationship has been observed for all tested beams as shown in Figure 4.12. The first linear part of the curve up to cracking represents the uncracked section which was similar for all the beams and it depends on the gross moment of inertia. This gross moment of inertia is well known as the property of the concrete cross-section. The second part is the post-cracking of the concrete up to steel yielding. At this part, a reduction in the beam stiffness occurs due to the decrease in the moment of inertia as it can be seen as a decrease in the slope of the load-deflection graphs.

The third and last part of the load-deflection curve represents the start of yielding of steel up to failure. The yielding of the steel results in a dramatic degradation in the stiffness of the beams. The LVDTs were removed prior to the failure to protect them from damage; hence, the last portion of this part was measured using the movement of the side grids through the taken videos as demonstrated in Figure 4.13.

In general, the beams repaired with STF mixtures have shown a better flexural strength behavior than the one repaired with PPF mixtures. Naaman [1996], has proven that the flexural behavior is a function of fibers length and their bond strength. Hence, the better behavior of the beams repaired with STF mixtures comparing to the one repaired with PP mixtures is mainly attributed to the longer fibers length, higher bond and stiffness. Also, the shape of the STF providing an additional increase in bond. The longer fibers will provide bridging stresses across the crack resulted in coalesce of the microcracks [Shah et al., 1996]. Therefore, the toughness of the concrete mixtures was increased as shown in Figure 4.12.

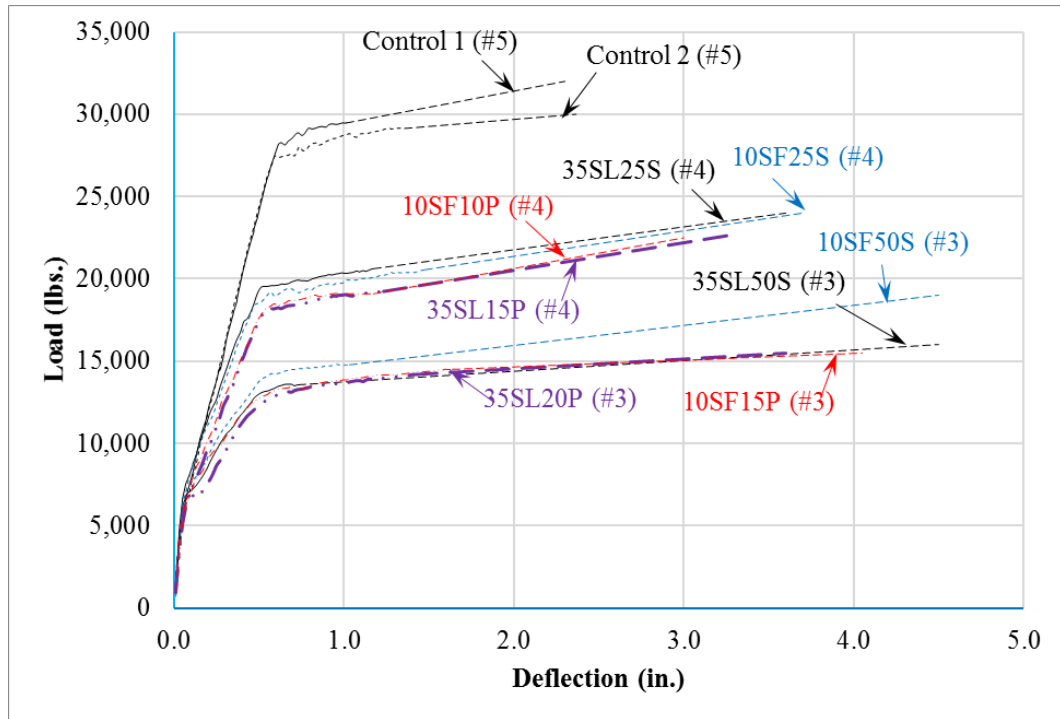


Figure 4.12 Deflection at Midspan for all the Beams



Figure 4.13 Measuring the Deflection at Midspan after Removing the LVDTs

4.4.3 Load – Strain Relationship

Figure 4.14 demonstrates the relationship between load and both steel reinforcement and concrete strains at the mid span for both control and repaired beams.

The strain in the main steel reinforcement was measured by using foil strain gauge; while, the strain on the concrete top fiber was measured using LVDT as explained in Chapter 3. The LVDT initial gauge length was recorded before starting the test, and the strain is measured by dividing the change in the LVDT reading to the initial gauge length. It can be seen from Figure 4.14 that when the load increases, both steel reinforcement and concrete strain are increased. It can be also seen that the main steel reinforcement exceeded its yield strain and also reached its hardening portion in both control and repaired beams. The maximum service strain in the main steel reinforcement were 3500 and 3900 microstrains for control and repaired beams, respectively. In general, beams repaired with STF showed higher service strain than the other beams for the same rebar size. Such increase in the strain value is mainly attributed to the higher concrete strength for the repair mixtures containing STF in it. In addition, to the high-volume fraction of the STF used comparing to PPF.

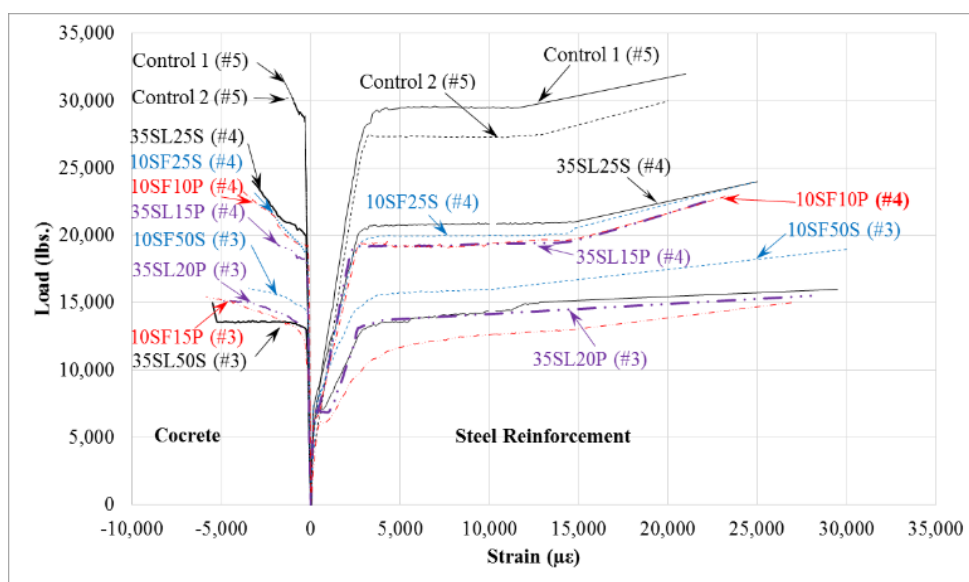


Figure 4.14 Relationship between applied Load and both Rebar Tensile Strain and Concrete Compressive strain for all Beams

4.4.4 Mode of Failure and Cracking Behavior

The failure mode observed for all the beams was due to the crushing of concrete. The cracks first initiated at flexural zone in the mid third of the beam between the two points load. These cracks were propagated vertically due to the pure bending at the beginning stage of the loading. Then, due to the increase in the load, shear stresses were increased, and the crack direction became inclined towards the nearest point load. When the load increased and the beams reached their yield capacity, the concrete at the compression zone crushed and the beams failed. It is good to mention that there was no visible horizontal crack at the interface layer between the concrete substrate and the repair layer for all of the repaired beams. At failure, it was noticed a very thin horizontal crack at the interface layer. The LVDT and VWSG at the interface layer were constant. Thus, there was no de-bonding. Figures 4.15 and 4.16 show fibers in the cracks at failure for beams repaired with PPF mixture and STF, respectively. These two figures show how the fibers randomly distributed and how they are bridging the crack. The mode of failure of beam specimens and crack patterns are shown in Figures 4.17 and 4.18, respectively.

Table 4.9 shows the number of cracks and the average crack spacing for all the beams. The average crack spacing is taken as the average spacing of flexure cracks between two loading points (i.e. constant moment zone). It was observed that the average crack spacing decreases with increased fiber content when comparing the repaired beams having the same rebar size. For beams contain #3 rebar size, the average crack spacing decrease in the following order (10SF15P, 35SL20P, 35SL50S, and 10SF50S) as shown in Figures 4.18-g through 4.18-j. While for the beams contain #4 rebar size, the decreasing in the average crack spacing is in the following order (10SF10P, 35SL15P, 35SL25S, and

10SF25S) as shown in Figures 4.18-c through 4.18-f. It was also observed that the number of cracks also increases when increasing the rebar size, and more flexural crack initiated beyond the maximum moment region. Figures 4.18-a through 4.18-b for beams contain #5 rebar have shown 8 cracks, while Figures 4.18-c through 4.18-f for beams contain #4 rebars and Figures 4.18-g through 4.18-j for beams contain #3 rebars have shown number of cracks of 7 and 6, respectively. Table 4.9 also illustrates the percentage of crack density at the cracking load for each beam. It was calculated by using Equation 4.1.

$$\text{Crack Density} = \frac{\sum_{i=1}^{i=n} (w.L)}{A} \cdot 100\% \quad (4.1)$$

Where

n = number of cracks between the two-point loading

W = crack width

L = crack length or depth

A= Area of the side of the beam between the two-point loading.

The results showed that the percentage of crack density increased with the increase of the fiber content when comparing between the beams having the same rebar size. This reflects how the fibers were able to bridge the cracks and reduce the crack width. It can also be concluded that there is no effect for the both SF and SL on the mode of failure and cracking behavior.

**Table 4.9 Number of Cracks and Average Crack spacing for the Tested Beams in
the Constant Moment Zone**

Beam	Rebar size number	Number of Cracks	Average Crack Spacing (in)	Crack Density at the cracking load ($\times 10^{-3}$ %)
Control 1	5	8	5.31	0.90
Control 2			5.03	0.92
35SL25S	4	7	6.08	1.07
35SL15P			6.13	1.04
10SF25S			5.88	2.50
10SF10P			6.42	0.82
35SL50S	3	6	6.71	1.52
35SL20P			7.48	0.85
10SF50S			6.57	1.61
10SF15P			7.63	0.52



**Figure 4.15 Picture Taken Using Digital Magnifier Camera at 70x Magnification
Showing Major Crack at Midspan in 35SL20P Repaired Beam at Failure**



Figure 4.16 Crack at Failure in 10SF50S Repaired Beam

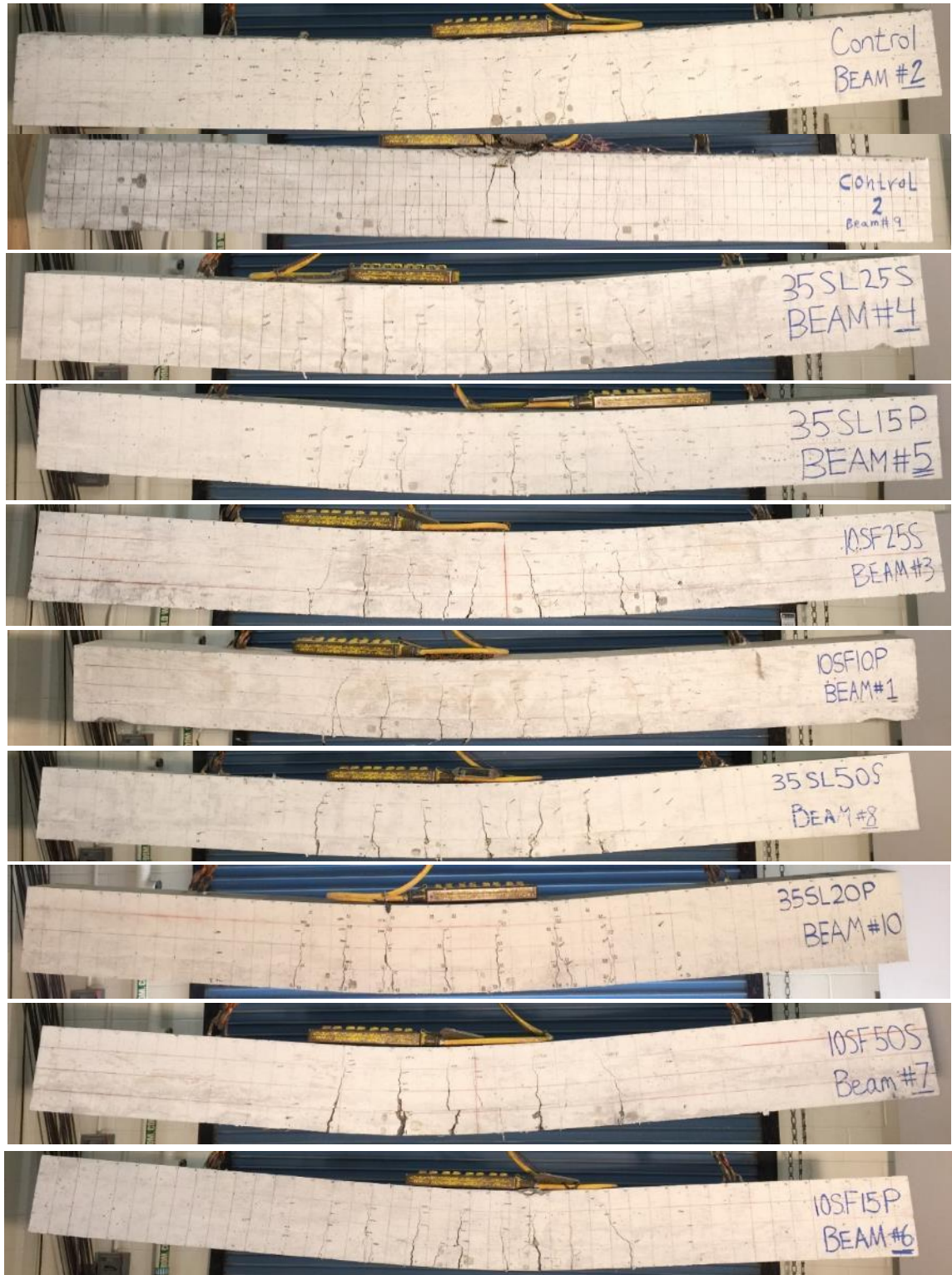
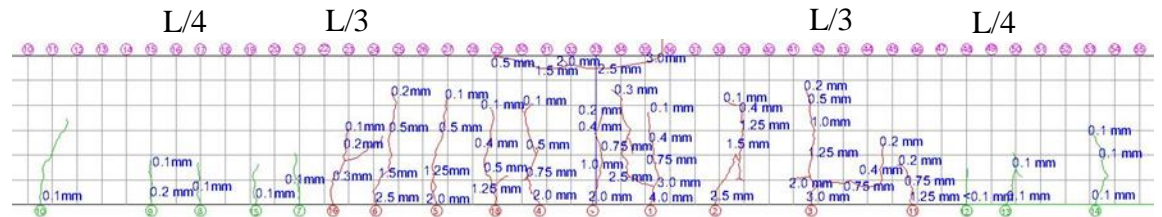


Figure 4.17 Mode of Failure of Beam Specimens



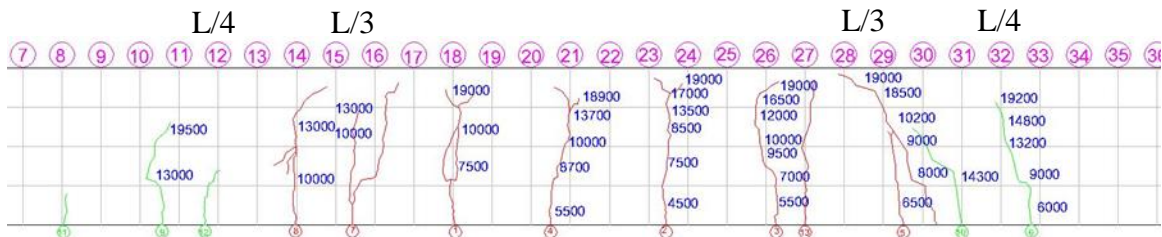
a) Control 1 (#5 rebar)



b) Control 2 (#5 rebar)



c) 35SL25S (#4 rebar)



d) 35SL15P (#4 rebar)



e) 10SF25S (#4 rebar)



f) 10SF10P (#4 rebar)



g) 35SL50S (#3 rebar)



h) 35SL20P (#3 rebar)



i) 10SF50S (#3 rebar)



j) 10SF15P (#3 rebar)

Figure 4.18 Crack Patterns and Width at Failure for all the Beams

4.4.5 Neutral Axis

In order to find the change in strain profile during the loading, strain results from different measurements along the section of the maximum moment were used. As illustrated in Figure 4.18, the compressive strain in concrete top fiber was measured using LVDT, while the strain in the main reinforcement was measured using strain gauges. In addition, the two lateral concrete strain gauges were also used to verify the strain reading along the section profile. The strain values at various loading stages such as cracking, yielding of rebar, and ultimate loads were plotted as shown in Figures 4.19 through 4.21. The results showed that as soon as the beam cracks, the beam stiffness reduces and the depth of neutral axis moves up to maintain the equilibrium of the section. The results also showed that the neutral axis shifted up for the repaired beams comparing to the control one.

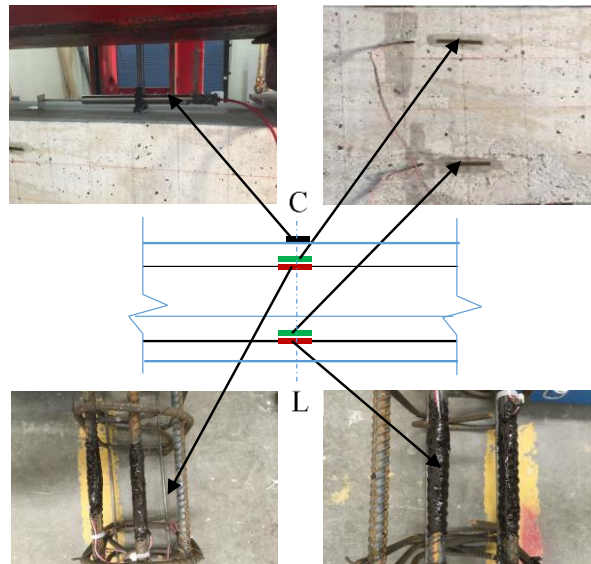
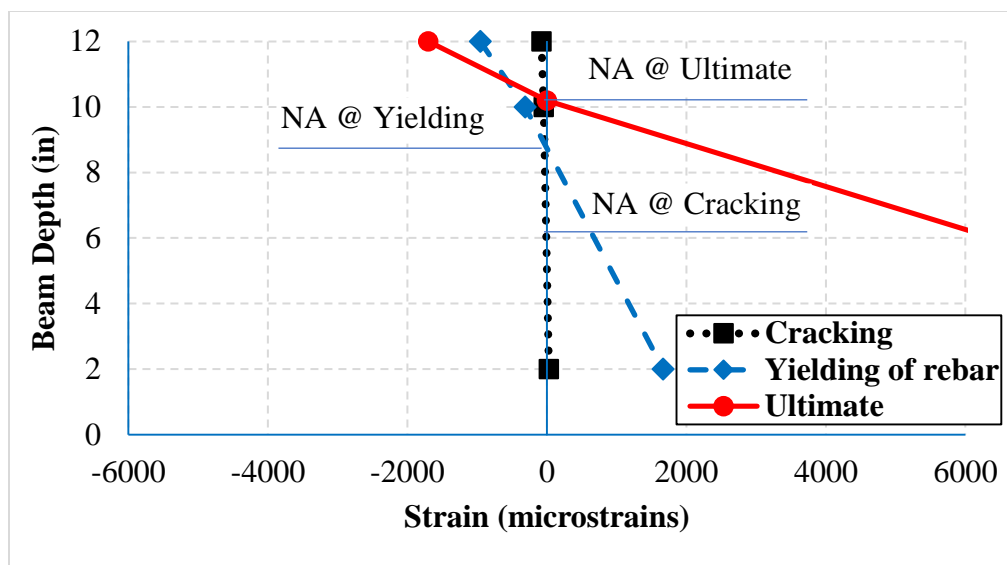
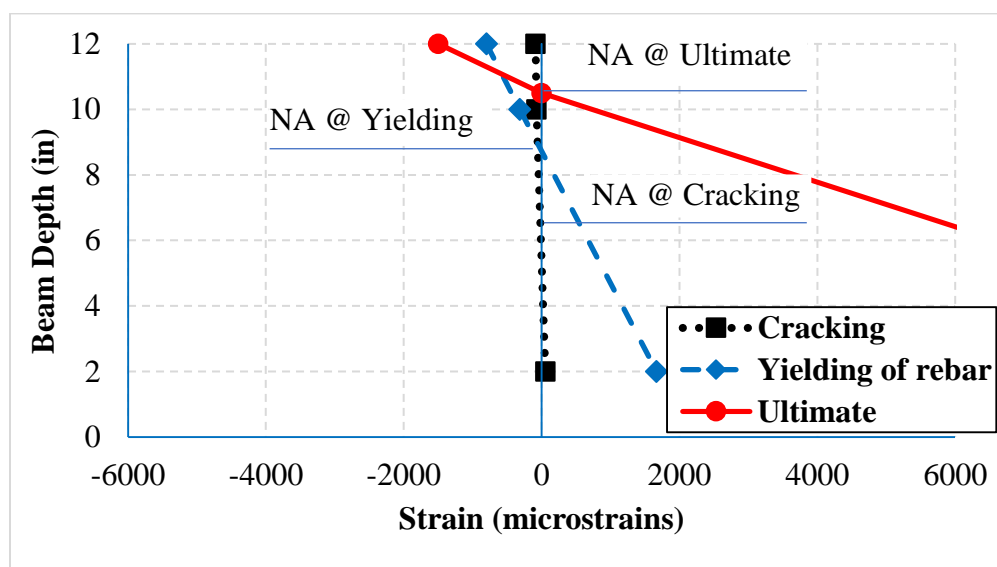


Figure 4.19 Location of Strain Gauges and LVDT Used to Determine the NA

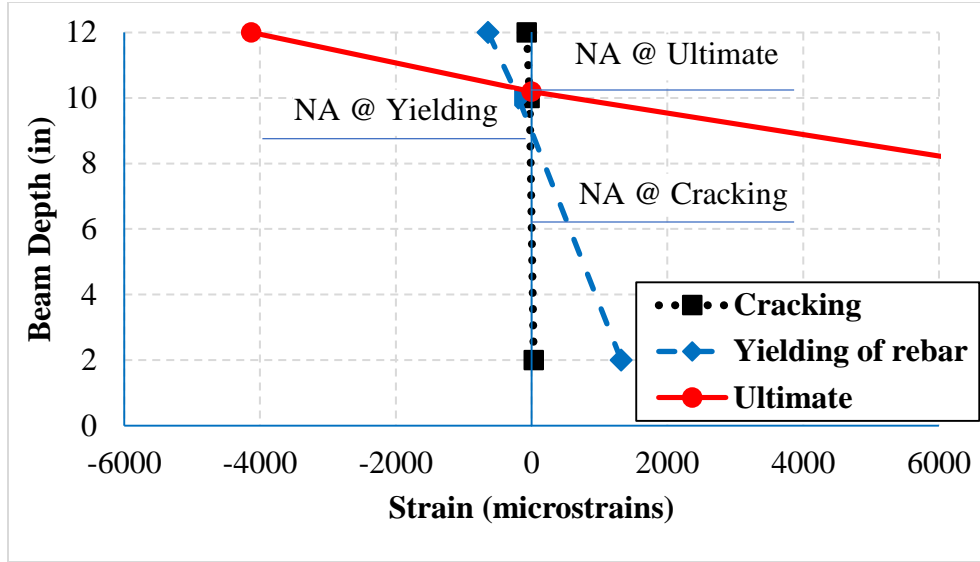


a) Control 1

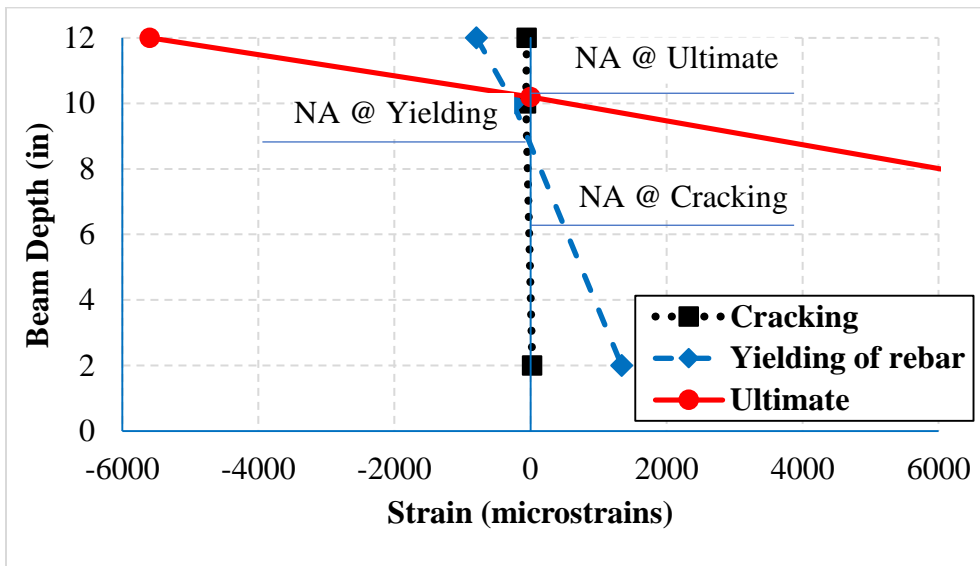


b) Control 2

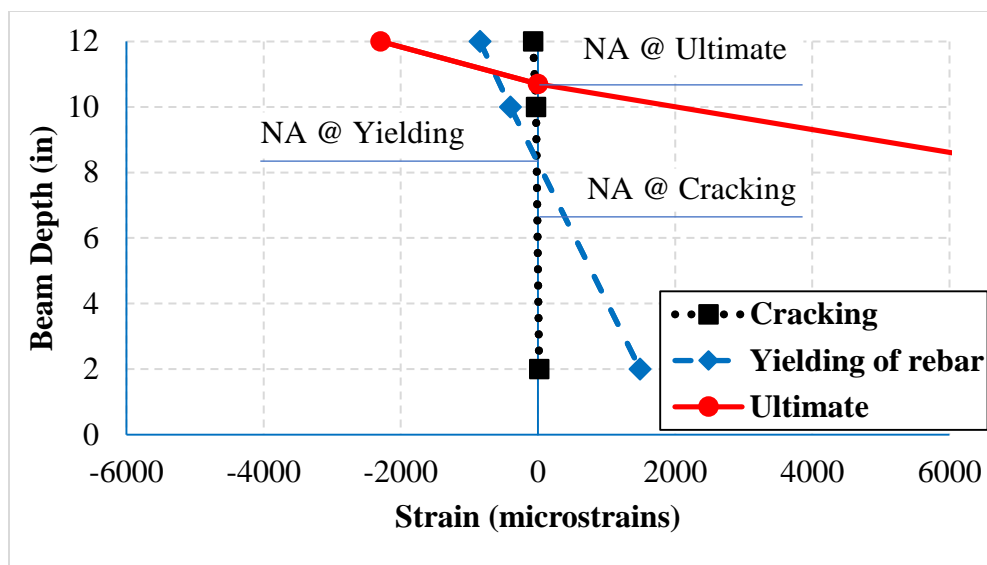
Figure 4.20 Concrete Strain Profile at the Section of Maximum Moment at Various Load Levels for Control Beam Contains #5 Rebars ($A_s = 0.93 \text{ in}^2$)



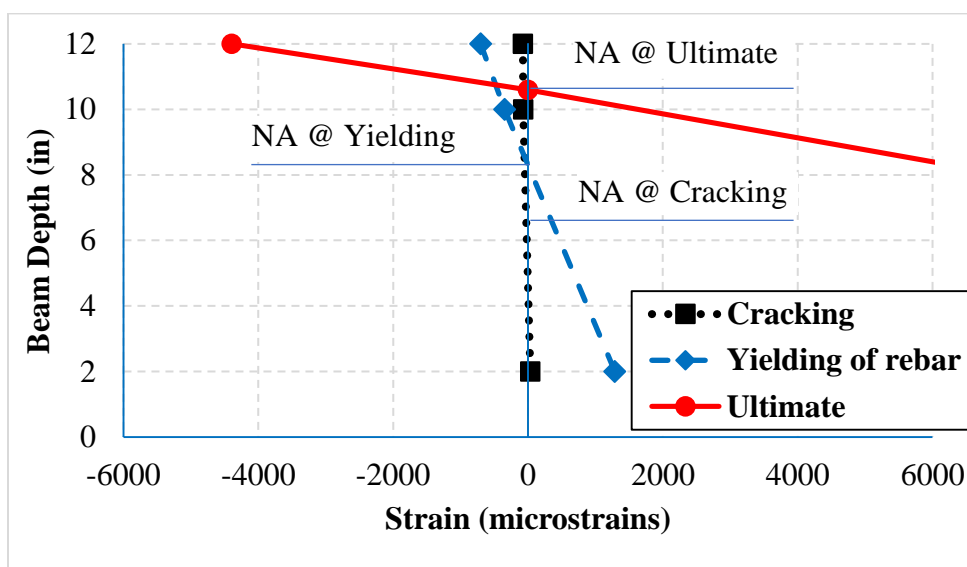
35SL25S



35SL15P

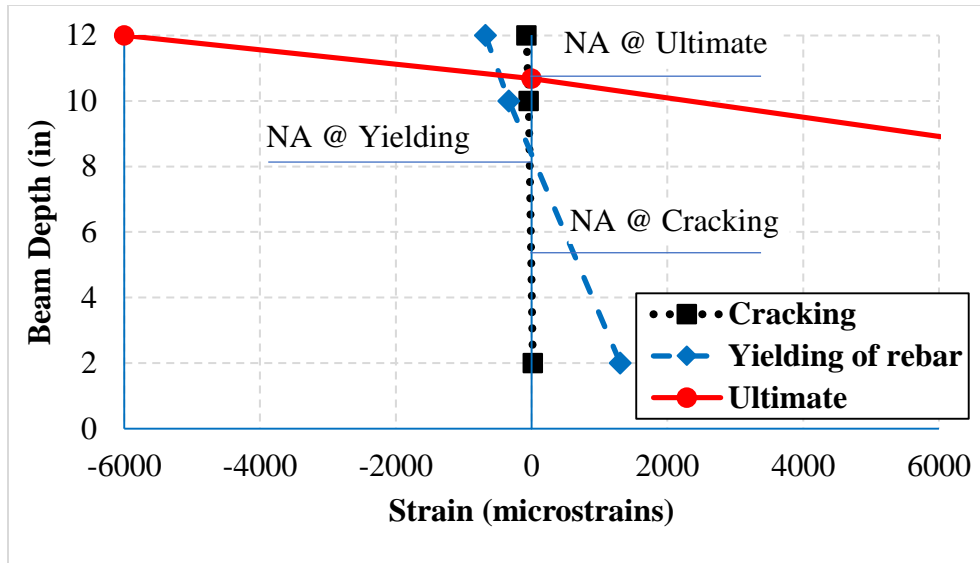


10SF25S

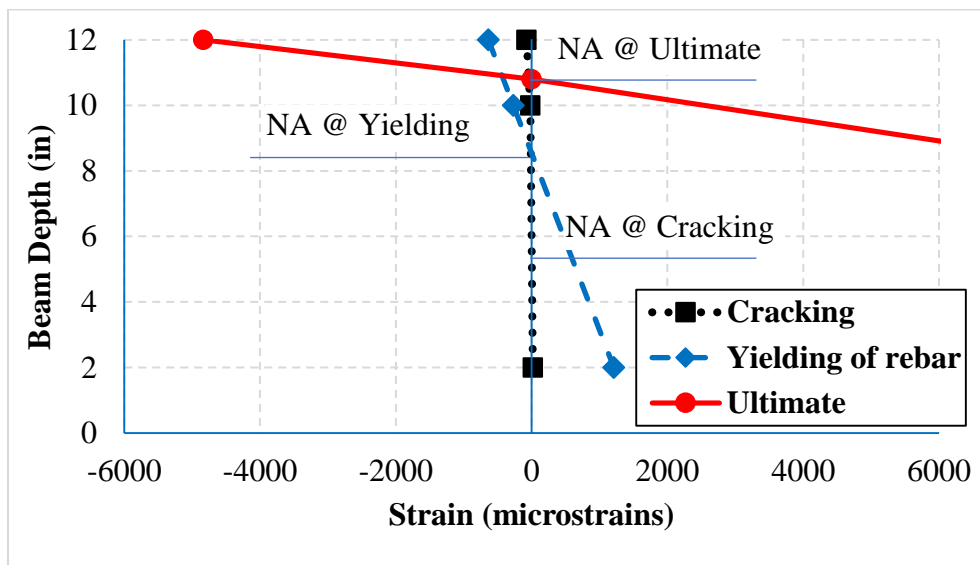


10SF10P

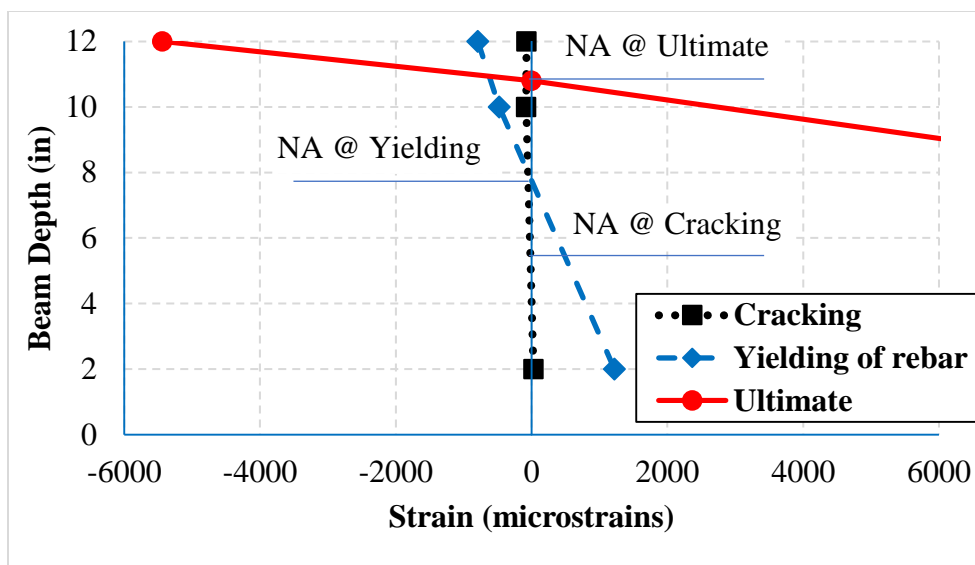
Figure 4.21 Concrete Strain Profile at the Section of Maximum Moment at Various Load Levels for Repaired Beams Contain #4 Rebars ($A_s = 0.6 \text{ in}^2$)



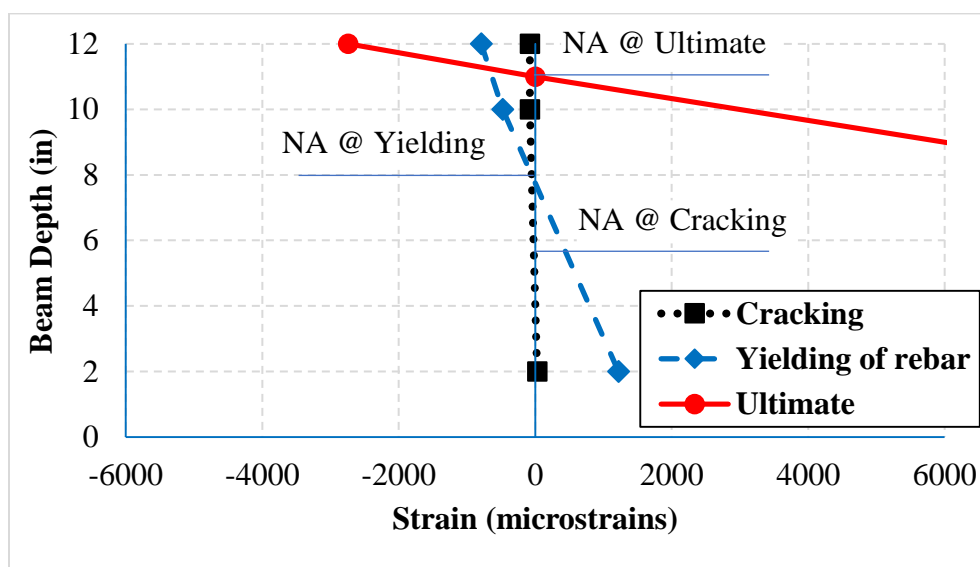
35SL50S



35SL20P



10SF50S



10SF15P

Figure 4.22 Concrete Strain Profile at the Section of Maximum Moment at Various Load Levels for Repaired Beams Contain #3 Rebars ($A_s = 0.33 \text{ in}^2$)

CHAPTER 5 FINITE ELEMENT MODELING AND CODE PREDICTIONS

5.1 Introduction

The prediction of the structural properties of all the beams was undertaken based on the results that were obtained from the experimental work. The structural properties include cracking load, ultimate load, and deflection. In this chapter, the codes' equations for these properties will be compared with the experimental results. Also, a rational, simple, accurate and user-friendly analytical model was developed using ABAQUS, which can be solved using nonlinear analysis at various load levels. The repaired and tested beams were simulated using the developed model, and then, validated to check the accuracy of the model.

A validated FEM has many advantages compared to the experimentally measured data in many aspects. The output of the experimental test is usually limited to that recorded by a discrete number of strain gauges and LVDTs at few selected points within the beam, while the FEM provides predicted full deformation and stress results throughout the beam for the entire loading history. The validated models can be used as an attractive numerical tool for researchers and engineers to study the flexural behavior of repaired beams with FR-SCC with different setting and parameters that can save time, money, and effort. The analytical investigation diagram is shown in Figure 5.1.

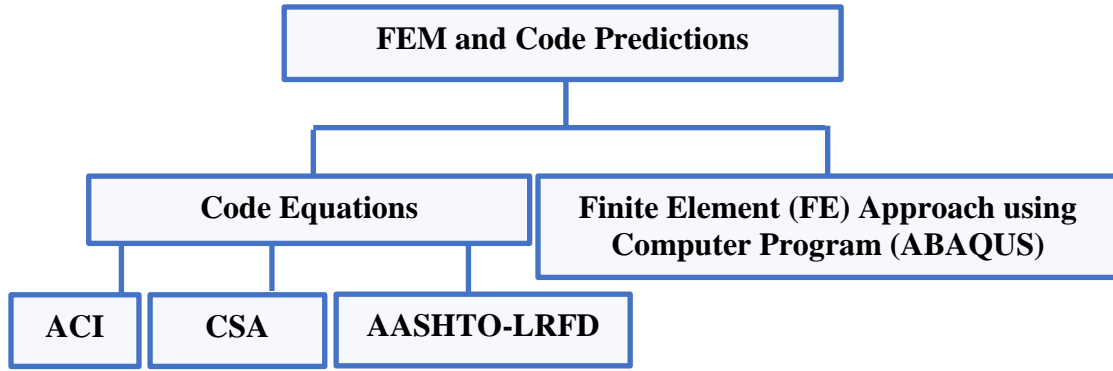


Figure 5.1 Analytical Investigation Diagram

5.2 Code Equations

To check the applicability of the code equations in prediction the flexural behavior of the repaired beams with FR-SCC, the results from the code equations were compared with the experimental data. Some of the code equations were designed for non-fibrous concrete, therefore, they might need to be modified.

5.2.1 Prediction of Cracking Load

The cracking load can be predicted by the ACI 318 [2014], CSA A23.3 [2004], AASHTO-LRFD [2012], and ACI 544 [2011] codes through different theoretical calculations that can be used to determine the crack load of concrete made with and without fibers.

5.2.1.1 ACI 318 [2014] Code

The following expressions can be used to predict the cracking load,

$$f_r = 7.5\sqrt{f'_c} \quad (\text{Psi}) \quad \text{ACI 318[2014]} \quad (5-1)$$

$$f_{cr} = \frac{M_{cr}}{I} Y \quad \text{therefore} \quad M_{cr} = \frac{I f_{cr}}{Y} \quad (5-2)$$

$$I = \frac{b \cdot h^3}{12} \quad (\text{for a rectangular section}) \quad (5-3)$$

$$Y = \frac{h}{2} \quad (5-4)$$

From the moment equilibrium ($\sum M = 0$):

$$M_{cr} = a \frac{P_{cr}}{2}, \quad \text{hence,} \quad P = \frac{2M_{cr}}{a} \quad (5-5)$$

Where:

f_{cr} : cracking strength in the tensioned part of the beam (modulus of rupture);

f'_c : compressive strength in the tensioned part of the beam at flexural test age (compressive strength of the repair concrete in the case of the repair beams);

P_{cr} and M_{cr} : crack load and crack moment, respectively; and

a : shear span

5.2.1.2 CSA A23.3 [2004] and AASHTO-LRFD [2012] Codes

The CSA A23.3 [2004] and AASHTO-LRFD [2012] codes are similar to the ACI 318 [2014] code except for the modulus of rupture (f_{cr}) which can be calculated as follow:

$$f_{cr} = 0.6\sqrt{f'_c} \quad (\text{MPa}) \quad \text{CSA A23.3 [2004]} \quad (5-6)$$

$$f_{cr} = 0.23\sqrt{f'_c} \quad (\text{Ksi}) \quad \text{AASHTO-LRFD [2012]} \quad (5-7)$$

5.2.1.3 ACI 544 [2011] Code

The cracking load can be calculated according to the ACI 544 [2011] using Equation (5-8).

$$f_{cr} = 0.843 f_r V_m + 425 V_f L_f / d_f \quad \text{ACI 544 [2011]} \quad (5-8)$$

$$V_m = 1 - V_f \quad (5-9)$$

Where:

f_{cr} : first-crack composite strength, psi;

f_r : stress in the matrix (modulus of rupture of the plain mortar or concrete, psi, obtained from the ASTM C 78 test on 4×4×16 in beams);

V_m : volume fraction of the matrix;

V_f : volume fraction of the fibers; and

L_f / d_f : is the ratio of the length to diameter of the fibers (aspect ratio).

Table 5.1 and Figs. 5.2 through 5.5 show the f_{cr} value of the cracking load is compared to the experimental value obtained from the load-deflection curve, or from direct observation. It can be seen that the ACI 318 [2014], CSA A23.3 [2004], and AASHTO-LRFD [2012] overestimate the cracking load in both control and repaired beams. The average of the experimental to predicted cracking load for both control and repaired beams ($P_{cr \text{ exp}}/P_{cr \text{ pred}}$) for the ACI 318 [2014], CSA A23.3 [2004], and AASHTO-LRFD [2012] were 0.93, 0.96, and 0.91, respectively. While the ACI 544 [2011] underestimates the

cracking loads for both control and repaired beams with a mean of 1.12. Such results are mainly attributed to that the ACI 544 [2011] code considers the effect of fibers. Tables 5.2 through 5.5 show the percentage error in predictions, mean (μ), and Standard Deviation (SD) for the ACI 318 [2014], CSA A23.3 [2004], AASHTO-LRFD [2012], and ACI 544 [2011] codes, respectively. The CSA A23.3 [2004] code was more accurate in predicting the cracking load for both control and repaired beams than the other aforementioned codes with μ and SD equal to 10 % and 5 %, respectively. The mean of percent error (μ) for the ACI 544 [2011] is 18 % with an SD of 8 % considering both control and repaired beams. The corresponding percentages for the ACI 318 [2014], CSA A23.3 [2004], and AASHTO-LRFD [2012] codes are 11, 11, and 10 with SD of 7, 8, and 5, respectively. This show that there is a need to modify the ACI 544 [2011] to increase its accuracy in predicting the cracking load for the FR-SCC.

Table 5.1 Results of Predicted Cracking Load by ACI 318, CSA A23.3, AASHTO-LRFD, and ACI 544 Codes

Results Beam	Pcr (lbs)					Pcr _{exp} /Pcr _{Pred.}			
	ACI 318	CSA A23.3	AASH- TO	ACI 544	Exp.	ACI 318	CSA A23.3	AASH- TO	ACI 544
Control 1	5417	5219	5482	3360	4700	0.87	0.90	0.86	1.40
Control 2	5418	5219	5482	3360	4600	0.85	0.88	0.84	1.37
35SL25S	5412	5213	5476	4036	5500	1.02	1.06	1.00	1.36
35SL15P	5130	4942	5191	5544	4900	0.96	0.99	0.94	0.88
10SF25S	6586	6345	6665	4974	5500	0.84	0.87	0.83	1.11
10SF10P	6559	6319	6637	5867	5500	0.84	0.87	0.83	0.94
35SL50S	5130	4942	5191	4377	5700	1.12	1.15	1.10	1.30
35SL20P	4971	4788	5030	6160	5100	1.03	1.07	1.01	0.83
10SF50S	6949	6695	7032	5312	6000	0.87	0.90	0.85	1.13
10SF15P	6478	6241	6556	6483	5700	0.88	0.91	0.87	0.88
Ave. Pcr _{Exp} /Pcr _{Pred.}	Control					0.86	0.89	0.85	1.38
	Repaired					0.95	0.98	0.93	1.05
	Mean of both control and repaired					0.93	0.96	0.91	1.12

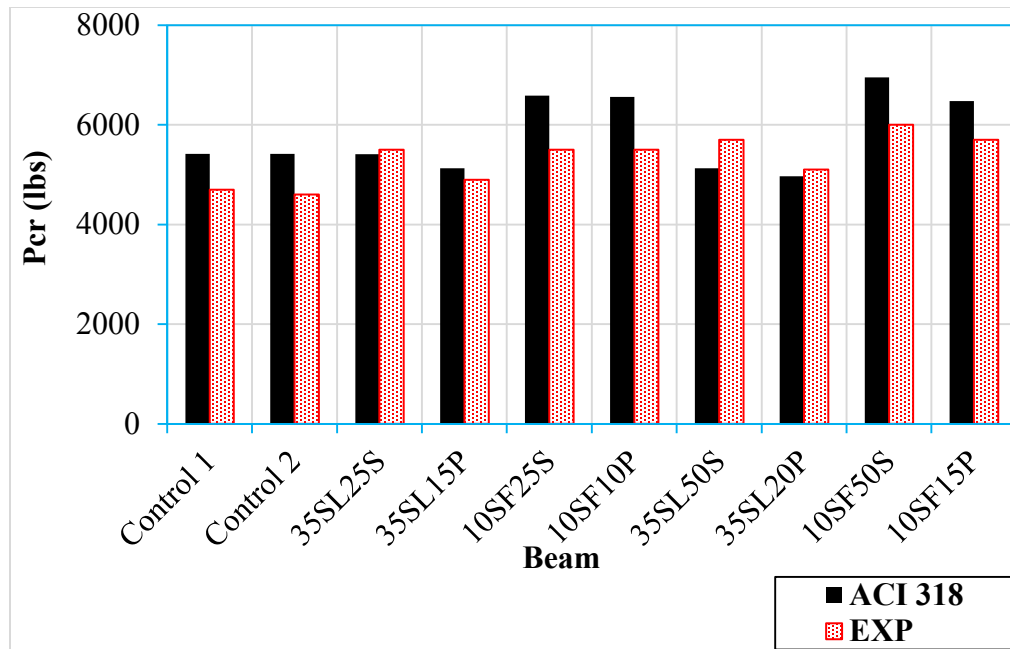


Figure 5.2 Comparison of Prediction of Cracking Load Using ACI 318 [2014] with the Experimental Results

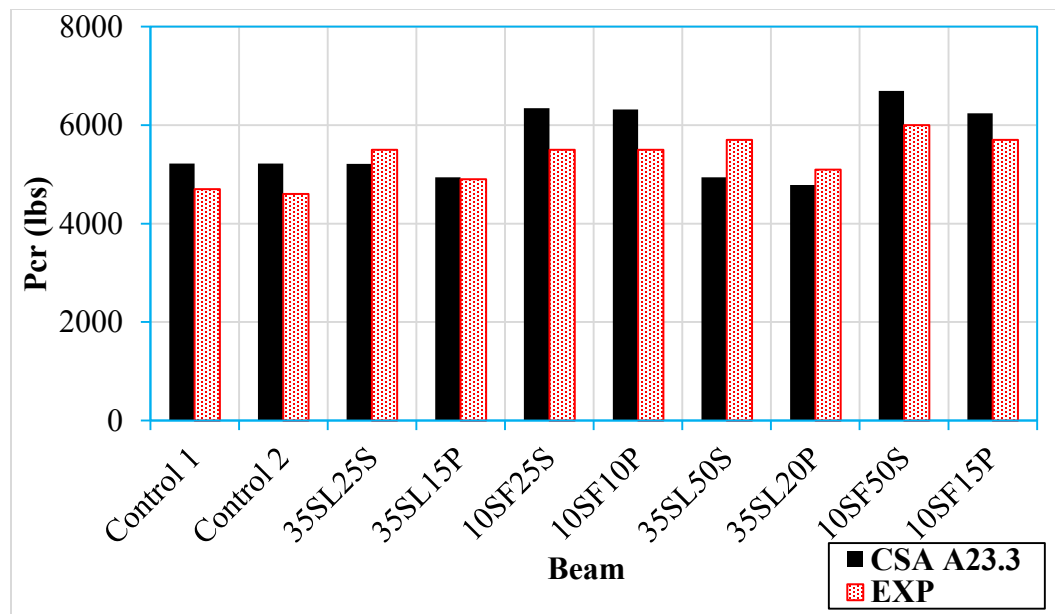


Figure 5.3 Comparison of Prediction of Cracking Load Using CSA A23.3 [2004] with the Experimental Results

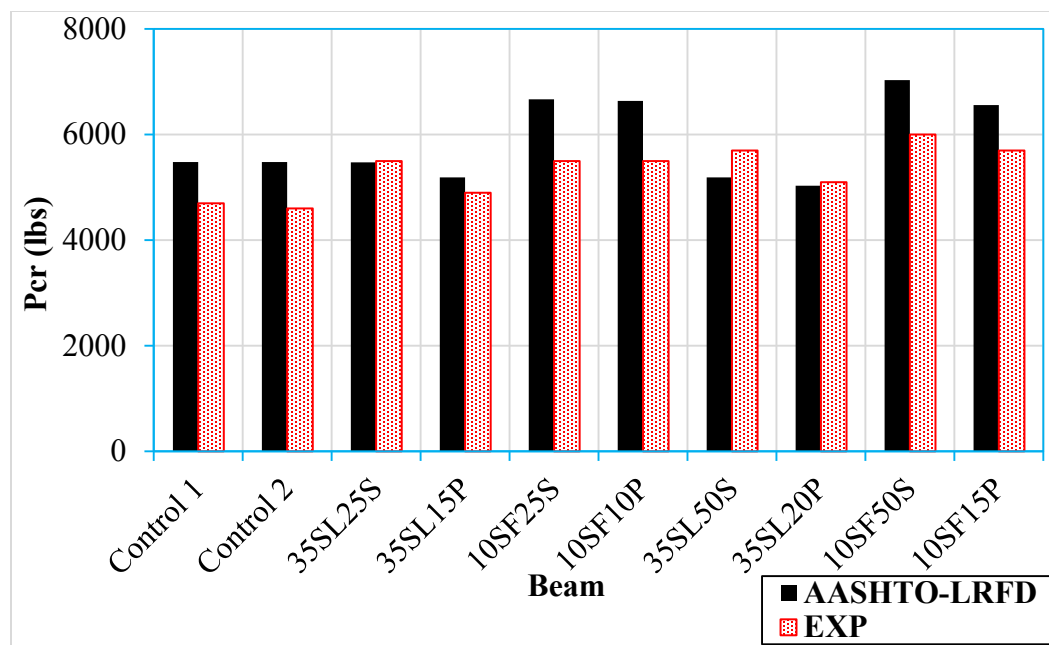


Figure 5.4 Comparison of Prediction of Cracking Load Using AASHTO-LRFD [2012] with the Experimental Results

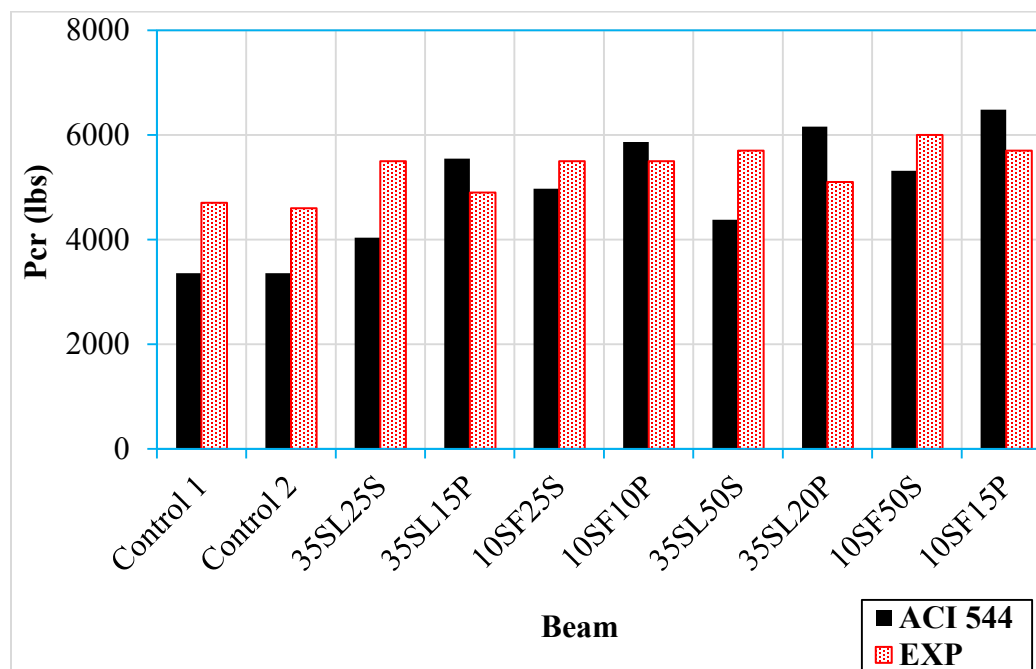


Figure 5.5 Comparison of Prediction of Cracking Load Using ACI 544 [2011] with the Experimental Results

**Table 5.2 Results of the Statistical Analysis of the Predicted Cracking Load by ACI
318 Code**

Results Beam	Error ACI 318 (%)	μ (%)	SD (%)	μ (%)	SD (%)
Control 1	15	17	2	12	7
Control 2	18				
35SL25S	2	11	7		
35SL15P	5				
10SF25S	20				
10SF10P	19				
35SL50S	10				
35SL20P	3				
10SF50S	16				
10SF15P	14				

**Table 5.3 Results of the Statistical Analysis of the Predicted Cracking Load by
AASHTO- LRFD Code**

<div>Results</div> <div>Beam</div>	Error AASHTO- LRFD (%)	μ (%)	SD (%)	μ (%)	SD (%)
Control 1	17	18	2	13	8
Control 2	19				
35SL25S	0	11	8		
35SL15P	6				
10SF25S	21				
10SF10P	21				
35SL50S	9				
35SL20P	1				
10SF50S	17				
10SF15P	15				

Table 5.4 Results of the Statistical Analysis of the Predicted Cracking Load by CSA**A23.3 Code**

Results Beam	Error CSA A23.3 (%)	μ (%)	SD (%)	μ (%)	SD (%)
Control 1	11	12	2	10	5
Control 2	13				
35SL25S	5	10	5		
35SL15P	1				
10SF25S	15				
10SF10P	15				
35SL50S	13				
35SL20P	6				
10SF50S	12				
10SF15P	9				

Table 5.5 Results of the Statistical Analysis of the Predicted Cracking Load by ACI**544 Code**

Results Beam	Error ACI 544	μ (%)	SD (%)	μ (%)	SD (%)
Control 1	29	28	1	18	8
Control 2	27				
35SL25S	27	16	7		
35SL15P	13				
10SF25S	10				
10SF10P	7				
35SL50S	23				
35SL20P	21				
10SF50S	11				
10SF15P	14				

5.2.2 Prediction of Ultimate Load

The theoretical flexural strength of the repair beams can be calculated assuming composite behavior and linear strain distribution in the beam, as shown in Figure 5.6. This

is similar to the ACI 318 [2014] ultimate strength design method considering the extra tensile strength of the fibrous concrete and adding the strength provided by the reinforcing steel to obtain flexural strength. Henager and Doherty [1976] have made this design assumption, and it was adopted by ACI 544 [2011] for fiber reinforced concrete. The ultimate flexural capacity of the beam can be calculated as follows:

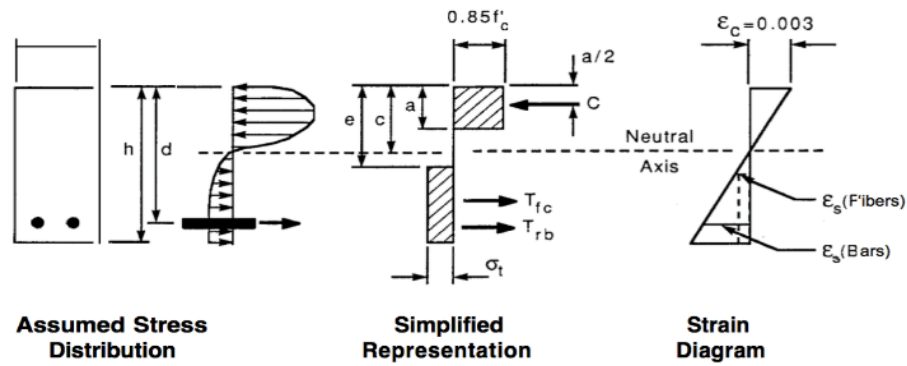


Figure 5.6 Stress and strain variation in FRC [Henager et al., 1976]

$$M_u = A_s f_y \left(d - \frac{a}{2} \right) + A'_s f'_y \left(\frac{a}{2} - d' \right) + \sigma_t b (h - e) \left(\frac{h}{2} + \frac{e}{2} - \frac{a}{2} \right) \quad (5-10)$$

$$\sigma_t = 1.12 \frac{l_f}{d_f} v_f f_{be} \quad (5-11)$$

where:

A_s : area of tension reinforcement;

A'_s : area of compressive reinforcement;

a: depth of rectangular stress block;

b: width of the beam; d: distance from extreme compression fiber to centroid of tensile

steel reinforcement;

d' : distance from extreme compression fiber to centroid of compressive steel reinforcement;

e : distance from extreme compression fiber to the top of fibrous concrete;

F_{be} : bond efficiency of the fiber which varies from 1.0 to 1.2 depending upon fiber characteristics; [Henager et al., 1976] (F_{be} assumed 1)

f_y : yield stress of tensile steel reinforcement;

f'_y : yield stress of compressive steel reinforcement;

h : overall thickness of the beam;

L_f , d_f , and V_f : fiber length, fiber diameter, and fiber volume (%), respectively;

σ_t : is the tensile stress of fibrous concrete.

Equation (5-10) is used to calculate the flexural capacity of the tested beams considering the effect of fibrous concrete of the repair layer, which was (3.5 in) in thickness for all FR-SCC repaired beams. The results of the predicted ultimate capacities and the comparison with the experimental capacities are illustrated in Table 5.6 and Figure 5.7. Equation (5-10) is given consistent conservative ultimate capacities comparing with experimental capacities with a mean ratio of $P_{u \text{ Exp}}/P_{u \text{ ACI 544}}$ equal to 1.4. The predicted ultimate capacities can be considered a reasonable for predicting both control and repaired beams under the study. Table 5.6 also shows the percentage error in predictions, mean, and

Standard Deviation (SD) for prediction the ultimate load using the ACI 544 [2011] code.

The mean of percent error is 30 % with an SD of 11 % considering both control and repaired beams.

Table 5.6 Results of Predicted Ultimate Load

<div>Results</div> <div>Beam</div>	P_u ACI 544 (lbs)	P_u Exp (lbs)	P_u Exp/ P_u ACI 544	Ave. P_u Exp/ P_u ACI 544	% Error	μ (%)	SD (%)	μ (%)	SD (%)
Control 1	25591	32000	1.3	1.4	20	17	4	30	11
Control 2	25591	30000	1.2		15				
35SL25S	16763	24000	1.4		30	33	10		
35SL15P	18416	22700	1.2		19				
10SF25S	16944	26200	1.5		35				
10SF10P	29382	23000	0.8		28				
35SL50S	9171	16000	1.7		43				
35SL20P	11415	15492	1.4		26				
10SF50S	9219	19000	2.1		51				
10SF15P	10852	15500	1.4		30				

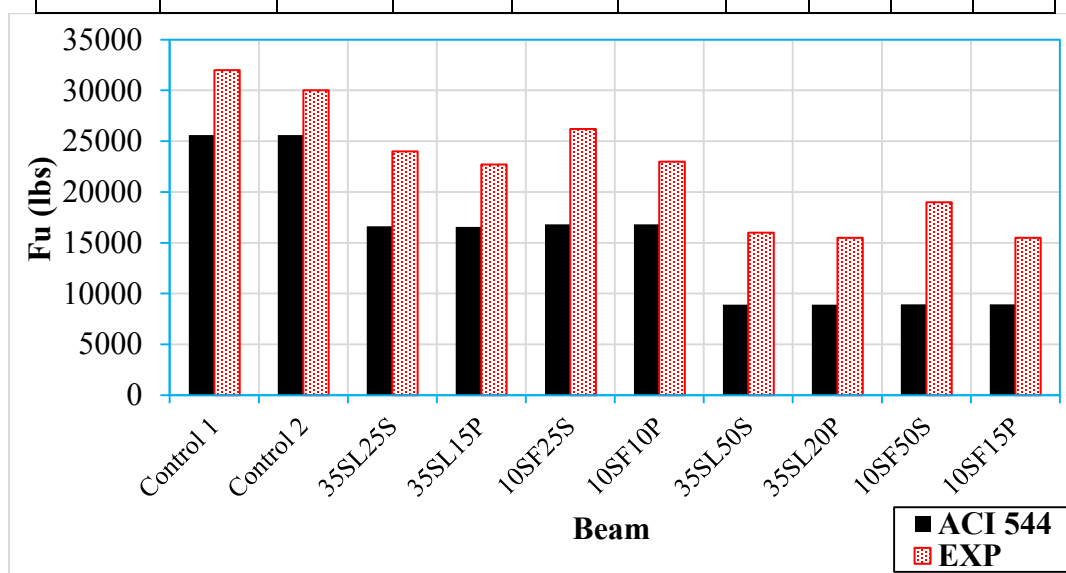


Figure 5.7 Comparison of Prediction of Ultimate Load Using ACI 544 [2011] with the Experimental Results

5.2.3 Prediction of Deflection

Theoretically, the maximal deflection at mid-span of a beam with two identical concentrated loads (Figure 5.8) is given by the following formula:

$$\Delta_{max} = \frac{pa}{48E_c I_e} (3L^2 - 4a^2) \quad (5-12)$$

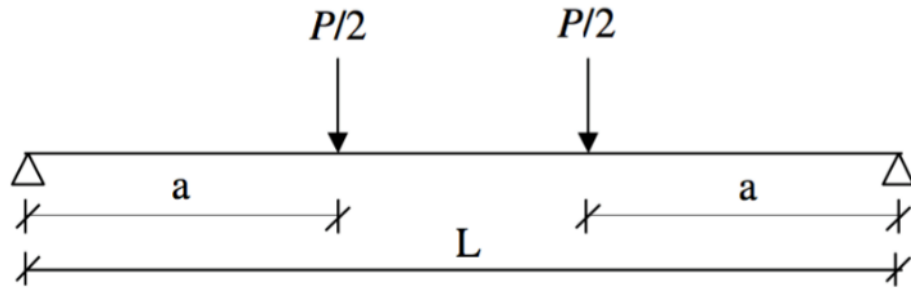


Figure 5.8 Loading Setup Used

where:

P is the total applied load,

E_c is the modulus of elasticity of the concrete,

I_e is the effective moment of inertia of the concrete section, which can be calculated from

Equation (5-13) proposed by Branson [1977] and adopted by the CSA A23.3 [2004]:

$$I_e = \left(\frac{M_{cr}}{M_a} \right)^3 I_g + \left[1 - \left(\frac{M_{cr}}{M_a} \right)^3 \right] I_{cr} \leq I_g \quad (5-13)$$

Where:

M_{cr} and M_a (in N.mm) are the cracking and applied moments, respectively;

I_g and I_{cr} are the moment of inertia of gross concrete section and the moment of inertia of cracked section of concrete, respectively.

The applied moment, M_a (maximum moment in a component at the stage for which deformation is computed) and the cracking moment, M_{cr} , can be given by the following equations:

$$M_a = \frac{P_a}{2} a \quad (5-14)$$

$$M_{cr} = \begin{cases} \frac{f_r I_g}{Y_t} \\ \frac{P_{cr}}{2} a \end{cases} \text{ or} \quad (5-15)$$

The modulus of rupture of concrete can be computed as follows:

$$f_r = 7.5\lambda\sqrt{f'_c} \text{ (psi)} \quad \text{ACI 318 [2014]} \quad (5-16),$$

$$f_r = 0.62\lambda\sqrt{f'_c} \text{ (MPa)} \quad \text{ACI CSA A23.3 [2004]} \quad (5-17), \text{ or}$$

$$f_r = 0.23\sqrt{f'_c} \text{ (Ksi)} \quad \text{AASHTO [2012], (for normal weight concrete)} \quad (5-18)$$

λ is a factor to account for low-density concrete ($\lambda = 1$ for normal-weight concrete);

The moment of inertia of gross concrete section I_g is given by:

$$I_g = \frac{bh^3}{12} \quad (5-19)$$

Where:

h : is the overall thickness or height of member, and b is width of member.

The distance from the centroid (neutral axis) of section to the extreme fiber in tension, Y_t

is:

$$Y_t = \frac{h}{2} \quad (5-20)$$

According to the ACI 318 [2014] and the CSA A23.3 [2004], the following equation gives the moment of inertia of a cracked concrete section (I_{cr}):

$$I_{cr} = \frac{bd^3}{3} k^3 + nA_s d^2 (1 - k)^2 \quad (5-21)$$

where k is effective length factor given by:

$$k = \sqrt{2\rho n + (\rho n)^2} - \rho n \quad (5-22)$$

d : is the distance from the extreme compression fiber to the centroid of the tension reinforcement for the entire composite section.

The ratio of non-prestressed tension reinforcement ρ is:

$$\rho = \frac{A_s}{A_c} \quad (5-23)$$

The surface of concrete, A_c is:

$$A_c = bd \quad (5-24)$$

$$n = \frac{E_s}{E_c} \quad (5-25)$$

E_c : is the modulus of elasticity of concrete measured experimentally or by the codes' equations. In this study, the experimental results for E_c were used.

The deflection at three different service loads was predicted for each beam. These loads were 4000, 9000, 10000, and 11000 lbs. The mean of the ratio of the experimental to

the predicted deflection is summarized in Table 5.7. All three models which are ACI 318[2014], CSA A23.3 [2004], and AASHTO LRFD [2012] did show non-conservative deflection prediction. The mean of $\Delta_{exp}/\Delta_{pred}$ for the control beams were 1.39, 1.36, and 1.42 for ACI 318[2014], CSA A23.3 [2004], and AASHTO LRFD [2012] respectively, while the corresponding values for the repaired beams were 1.76, 1.66, and 1.79 respectively. It can be seen that the all three codes are more non-conservative in predicting the deflection of the control beams comparing with repaired one. This is mainly because these codes were designed for normal concrete and not due to the inclusion of the FR-SCC layer in the repaired beams. The degree of underestimation of the repaired beams was found to be higher by 13-27% comparing to the control beams which can be considered acceptable based on the structural performance of the beams. An example of the correlation between the predicted load-deflection for the studied code with experimental for a repaired beam is shown in Figure 5.9.

Table 5.7 Results of Predicted Deflection for the Three Different Codes

Results Beam	Ave. $\Delta_{exp}/\Delta_{ACI}$ 318 [2014]	Mean $\Delta_{exp}/\Delta_{ACI}$ 318 [2014]	Ave. $\Delta_{exp}/\Delta_{CSA}$ A23.3 [2004]	Mean $\Delta_{exp}/\Delta_{CSA}$ A23.3 [2004]	Ave. $\Delta_{exp}/\Delta_{AASHTO}$ LRFD [2012]	Mean $\Delta_{exp}/\Delta_{AASHTO}$ LRFD [2012]
Control 1	1.45	1.39	1.40	1.36	1.47	1.42
Control 2	1.34		1.31		1.36	
35SL25S	1.14	1.76	1.09	1.66	1.15	1.79
35SL15P	1.37		1.32		1.38	
10SF25S	1.67		1.57		1.70	
10SF10P	2.31		2.16		2.36	
35SL50S	1.47		1.39		1.49	
35SL20P	1.37		1.31		1.38	
10SF50S	2.57		2.37		2.64	
10SF15P	2.20		2.05		2.25	

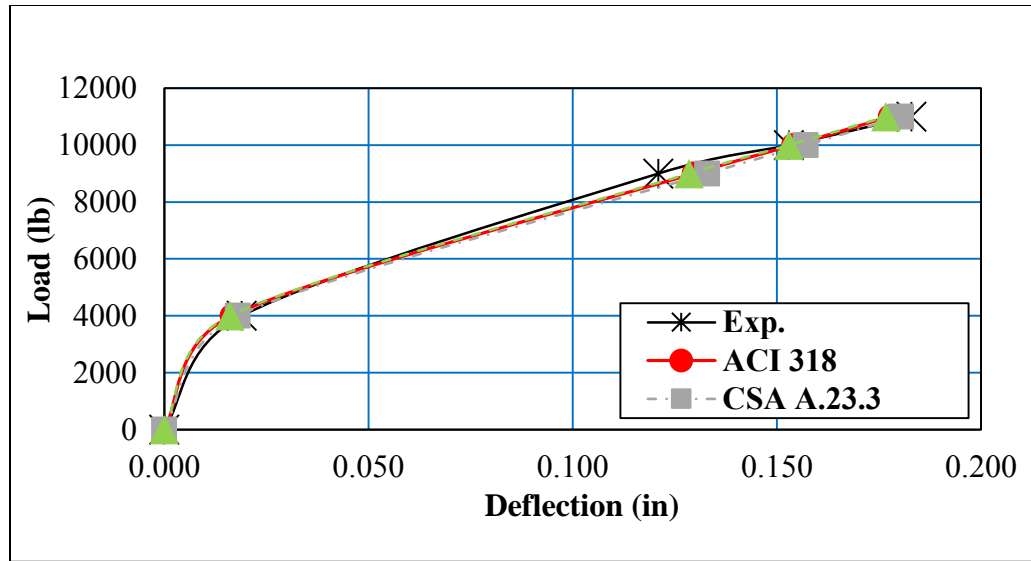


Figure 5.9 An Example of the Correlation between the Predicted Load-deflection for the Studied Code with Experimental for a Repaired Beam

5.3 Finite Element Approach

5.3.1 General

Finite element method is a method of placing the actual structure by a system of finite elements interconnected at the nodal points. This complexity may come from the complex geometry, loading pattern, boundary condition, and material properties. The ABAQUS commercial finite element package [ABAQUS 6.11] was used to model the composite beam and to perform the parametric study. It was used in this study because its concrete model is more compression-oriented, making it a more powerful tool to model the exact elastic-plastic behavior of the concrete. ABAQUS is a general-purpose finite element program designed specifically for advanced analysis of structural problems. A wide variety of problems can be addressed with the available modeling tools. ABAQUS includes a

variety of routines that allow for the implementation of specific material models such as concrete and steel, boundary conditions, and bond behavior.

Nassif and Najm [2004] conducted an experimental and analytical investigation of the use of ferrocement laminates to enhance the structural performance of the concrete beams. The results showed that using ferrocement plates is an effective in increasing cracking capacity and the developed model using ABAQUS is an effective tool to predict the flexural behavior of the composite beams.

5.3.2 Building the Finite Element Model

A Finite Element Model (FEM) was developed in this research for both of the repaired and control beams. Micro-modeling analysis level was used in which both the substrate and the repair are modeled using continuum approach as an elastoplastic damage to capture the true behavior when subject to loading. The accuracy of the analysis is highly dependent on the stress-strain relationships of the material constituents. Since the properties of the material used are available, actual material properties will be used in the model analysis.

In this study, the loading case is symmetrical. Therefore, only one-half of the system was modeled to reduce the number of equations as shown in Figure 5.10. The substrate and the repair layers were assumed to be perfectly bonded along their interface by constraining the same number of nodes in each of the two corresponding layers. Thus, both nodes would have the same degrees of freedom (i.e., displacements and rotations). Practically, the tested beams showed a full bond up to failure, and additional bond was achieved by the stirrups which were acting as shear studs along the interface layer between

the substrate and the repair layers. The loading was applied by displacement control in the vertical direction. The displacement recorded value from the experimental reached 1.5 inches because around that point the LVDTs were removed. The details of the increment of the displacement step are shown in Figure 5.11.

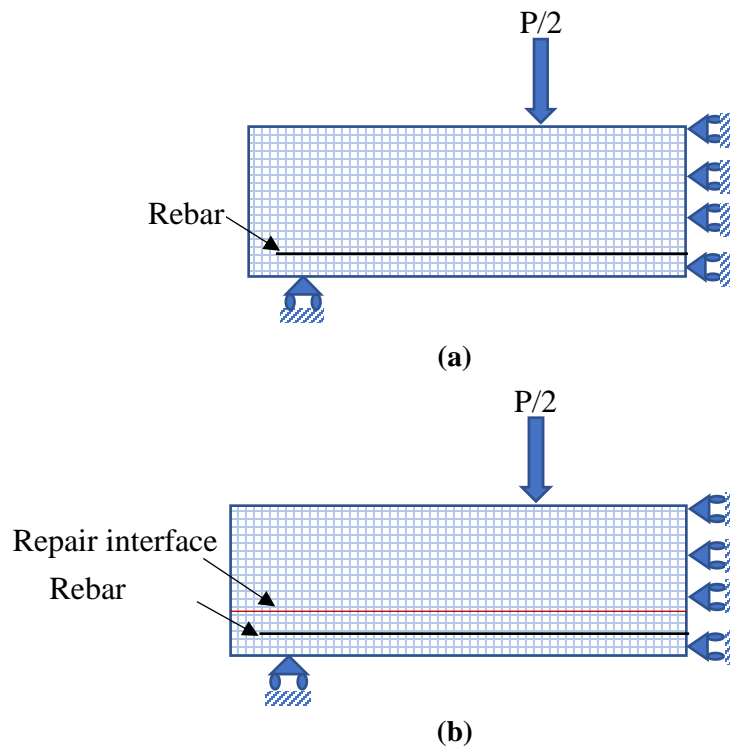


Figure 5.10 Finite Element Model of a Half Concrete Beam: a) Control Beam, b) Repaired Beam

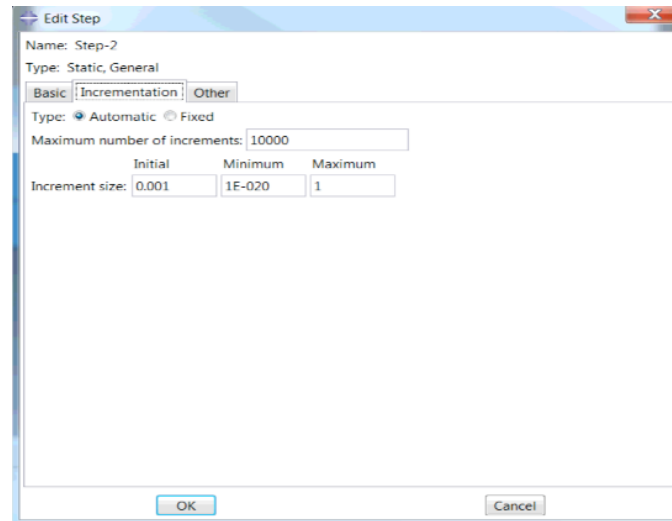


Figure 5.11 Details of the Incrementation limits

5.3.2.1 Types of Elements Used

Different element families are available to be employed in ABAQUS. One of the major distinctions between the various element families is the geometry type that each family assumes. Truss elements are rods that can carry only tensile or compressive loads. These elements have no resistance to bending; therefore, they are useful for modeling pin-jointed frames. When a beam is very slender (such as the steel rebar), it can be modeled as a truss. A truss element ‘‘T2D2’’ which is a 2-node linear displacement was chosen to simulate the rebar (steel reinforcement).

Quadrilateral elements are the recommended solid (continuum) elements. For both substrate and repair layers, the ‘‘CPS4R’’ element which is a 4-node bilinear plane stress quadrilateral, reduced integration, hourglass control was used. The first advantage of the reduce integration is to overcome the problem associated with using the first order elements. These elements use linear interpolation to obtain the nodal displacements.

Therefore, the edges are not able to curve under bending leading to a shear rather than bending deformation [ABAQUS, 2011]. This is known as a shear locking. The second advantage of the reduced integration elements is that the strains and stresses are calculated at the locations that provide optimal accuracy, the so-called Barlow points [Barlow, 1976]. A Third advantage is that the reduced number of integration points decreases CPU time and storage requirements. The disadvantage is that the reduced integration procedure can admit deformation modes that cause no straining at the integration points. These zero-energy modes make the element rank-deficient and cause a phenomenon called “hourglassing,” where the zero-energy mode starts propagating through the mesh, leading to inaccurate solutions. This problem is particularly severe in first-order quadrilaterals and hexahedra. To prevent these excessive deformations, an additional artificial stiffness is added to the element. In this so-called hourglass control procedure, a small artificial stiffness is associated with the zero-energy deformation modes. [ABAQUS, 2011]. Figure 5.12 shows the two types of element used.

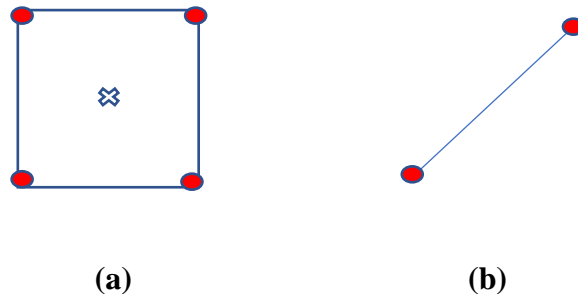


Figure 5.12 Types of Element Used

a) Four-node plane stress element and b) 2D-truss element

5.3.2.2 Material Models

This section essentially follows the development given in the ABAQUS 6.11 manual work to explain the constitutive material model used briefly. The Concrete Damage Plasticity (CDP) was used for both substrate and repair layers. The CDP is a continuum, plasticity-based, damage model for concrete. It assumes that the main two failure mechanisms are tensile cracking and compressive crushing of the concrete material. Two hardening variables control the evolution of the yield or failure surface, $\tilde{\varepsilon}_t^{pl}$ and $\tilde{\varepsilon}_c^{pl}$, linked to failure mechanisms under tension and compression loading, respectively. $\tilde{\varepsilon}_t^{pl}$ and $\tilde{\varepsilon}_c^{pl}$ as tensile and compressive equivalent plastic strains, respectively. The model assumes that the uniaxial tensile and compressive response of concrete is characterized by damaged plasticity, as shown in Figure 5.13.

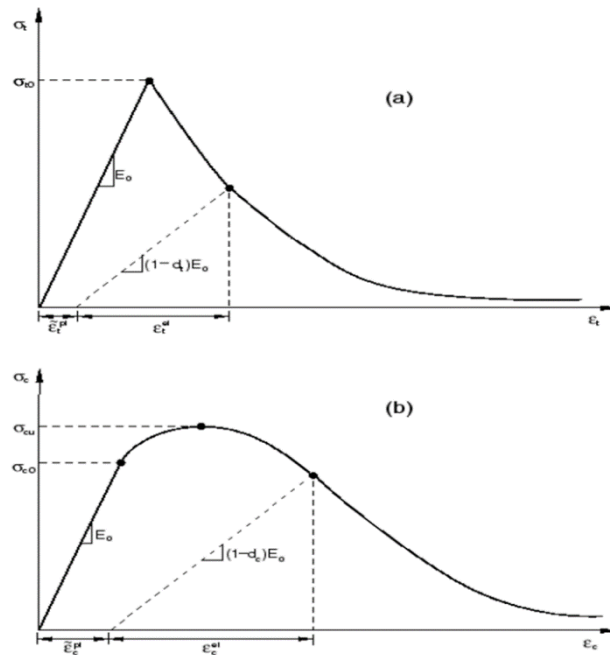


Figure 5.13 Response of concrete to uniaxial loading in tension (a) and (b) compression [ABAQUS, 2011]

Figure 5.13 also shows when the concrete specimen is unloaded from any point on the strain softening branch of the stress-strain curves, the unloading response is weakened. The elastic stiffness of the material appears to be damaged or degraded. The degradation of the elastic stiffness is characterized by two damage variables, d_t and d_c , which are assumed to be functions of the plastic strains, temperature, and field variables. The damage variables can take values from zero, representing the undamaged material, to one. Which represents total loss of strength. The stress-strain relations under uniaxial tension and compression loading are shown in Equations 5.26 and 5.27, respectively:

$$\sigma_t = (1 - d_t)E_0(\varepsilon_t - \tilde{\varepsilon}_t^{pl}) \quad (5-26)$$

$$\sigma_c = (1 - d_c)E_0(\varepsilon_c - \tilde{\varepsilon}_c^{pl}) \quad (5-27)$$

where,

E_0 : initial undamaged elastic stiffness of the material,

$\tilde{\varepsilon}_c^{in}$: compressive inelastic strain, and

$\tilde{\varepsilon}_t^{in}$: tensile inelastic strain

In ABAQUS, concrete behavior is considered independently of the rebar. Effects associated with the rebar/concrete interface, such as bond slip and dowel action, are modeled approximately by introducing some “tension stiffening” into the CDP model. The post-failure behavior (stress-strain relation) for direct straining is also modeled with tension stiffening, which allow to define the strain-softening behavior for cracked concrete. This behavior also allows for the effects of the reinforcement interaction with concrete to be simulated simply.

When there is no reinforcement in significant regions of the model, the tension stiffening approach described above will introduce unreasonable mesh sensitivity into the results. Hillerborg [1976] proposed a fracture energy approach that can be used to resolve this concern. He defines the energy required to open a unit area of crack, G_f , as a material parameter, using brittle fracture concepts. This fracture energy cracking model can be invoked by specifying the post-failure stress as a tabular function of cracking displacement (i.e. stress-displacement instead of stress-strain response), as shown in Figure 5.14a. The fracture energy, G_f , can also be specified directly as a material property. In this case, the failure stress, σ_{t0} , should be defined as a tabular function of the associated fracture energy. This model assumes a linear loss of strength after cracking, as shown in Figure 5.14b.

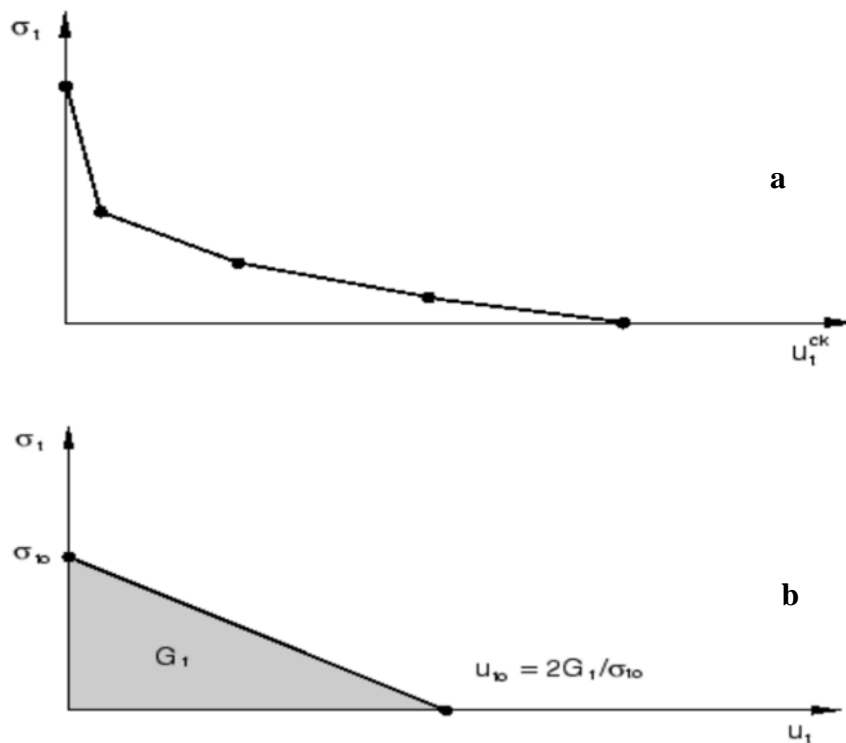


Figure 5.14 Post-failure Stresses Relationship: a) Post-failure Stress-displacement Curve; b) Post-failure Stress-fracture Energy Curve [ABAQUS, 2011]

The effective uniaxial cohesion stresses $\bar{\sigma}_t$ and $\bar{\sigma}_c$ can be calculated from Equation 5-28 and Equation 5-29. It determines the size of the yield (or failure) surface as shown in Figure 5.15.

$$\bar{\sigma}_t = \frac{\sigma_t}{(1-d_t)} = E_0(\varepsilon_t - \tilde{\varepsilon}_t^{pl}) \quad (5-28)$$

$$\bar{\sigma}_c = \frac{\sigma_c}{(1-d_c)} = E_0(\varepsilon_c - \tilde{\varepsilon}_c^{pl}) \quad (5-29)$$

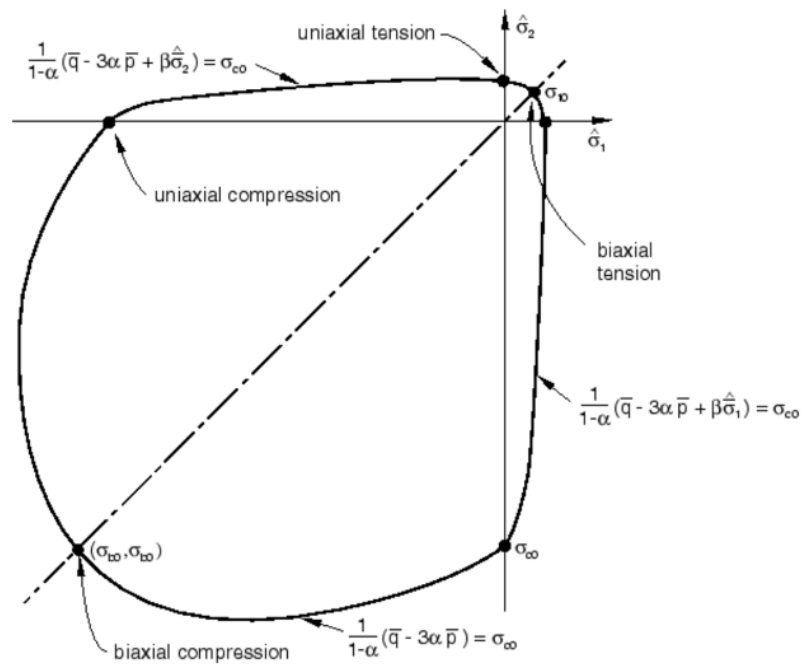


Figure 5.15 Yield Surface in Plane Stress [ABAQUS, 2011]

To define the yield surface, four constitutive parameters need to be defined in the CDP model. The first parameter is known as the dilation angle (ψ). Kmiecik and Kamiński [2011] defined the dilation angle as “the angle of inclination of the failure surface towards the hydrostatic axis, measured in the meridional plane”. (the default value is 36). The second parameter is the eccentricity (ϵ), which is defined as the eccentricity of the plastic

potential surface, (the default value is 0.1). The eccentricity can be also calculated as the ratio of tensile strength to compressive strength [Jankowiak et al., 2005]. The third parameter is σ_{b0}/σ_{c0} , which is the ratio of initial equibiaxial compressive yield stress to initial uniaxial compressive yield stress (the default value is 1.16). The fourth and last parameter is Kc, it can be defined as the ratio of the second stress invariant on the tensile meridian to that on the compressive meridian. The Kc value should be greater than 0.5, but less or equal. The default value Kc is 2/3. In this study, the default CDP parameters' values were used as illustrated in Table 5.8.

Table 5.8 Parameters Used in the Plastic Damage Model

Dilation angle (ψ)	Eccentricity (ϵ)	σ_{b0}/σ_{c0}	Kc	Poisson's Ratio
36	0.1	1.16	0.67	0.2

In addition to the constitutive parameters, there are other parameters that were needed to input into the ABAQUS program. As mentioned previously, the stress plastic strain for concrete material is also needed to be input in the finite element simulation. Figures 5.16 and 5.17 show the typical stress-strain used for concrete. While for steel, the stress-strain for grade 60 steel is shown in Figure 5.18.

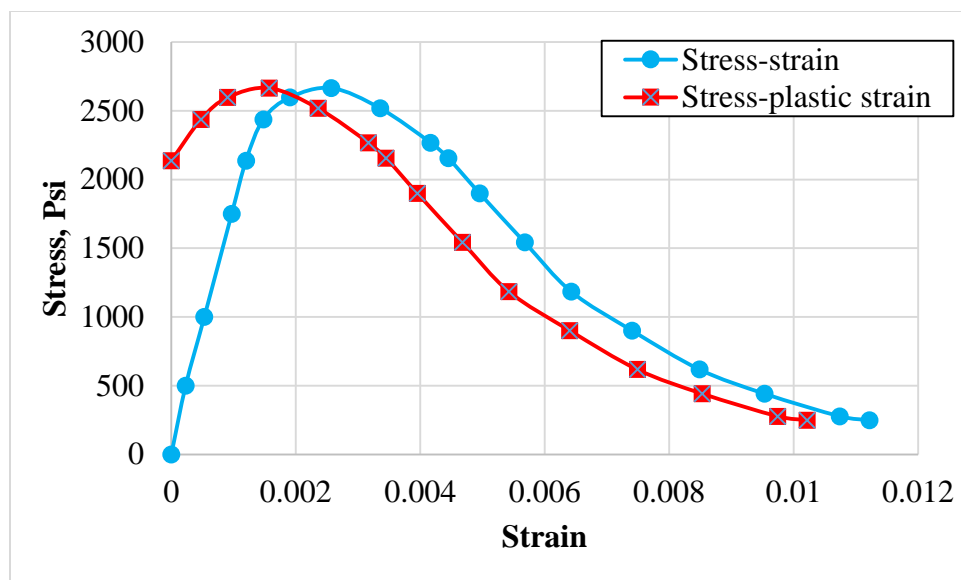


Figure 5.16 Stress- Strain for Concrete in Compression

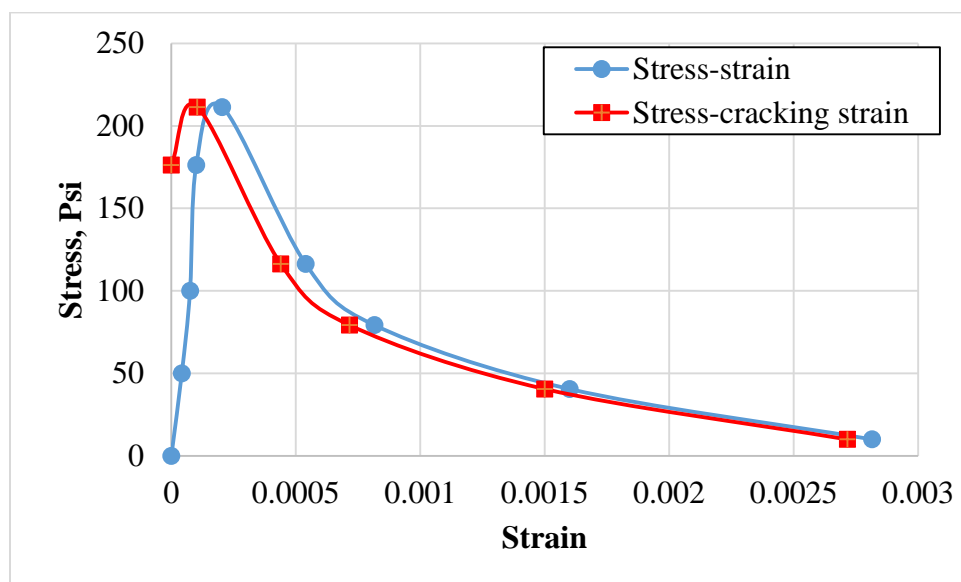
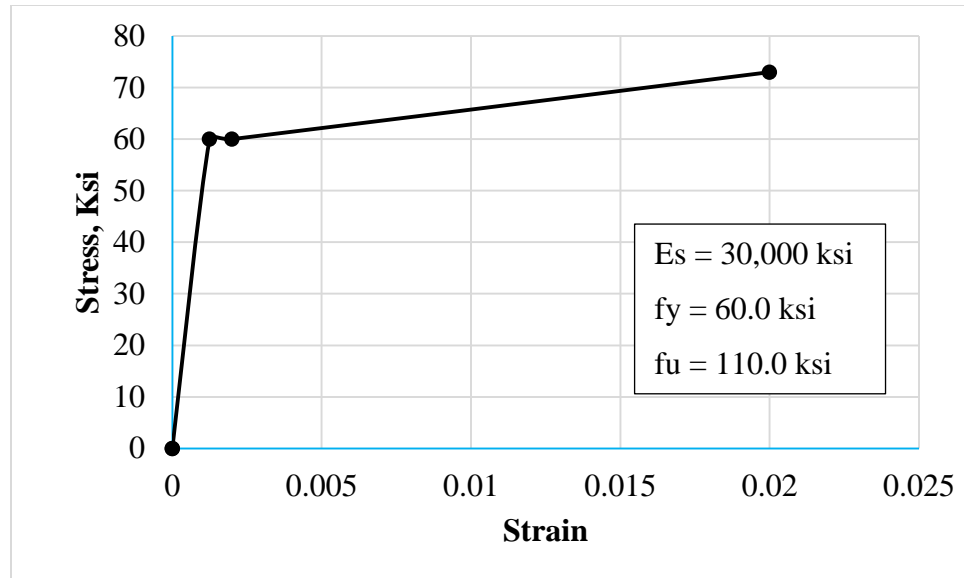
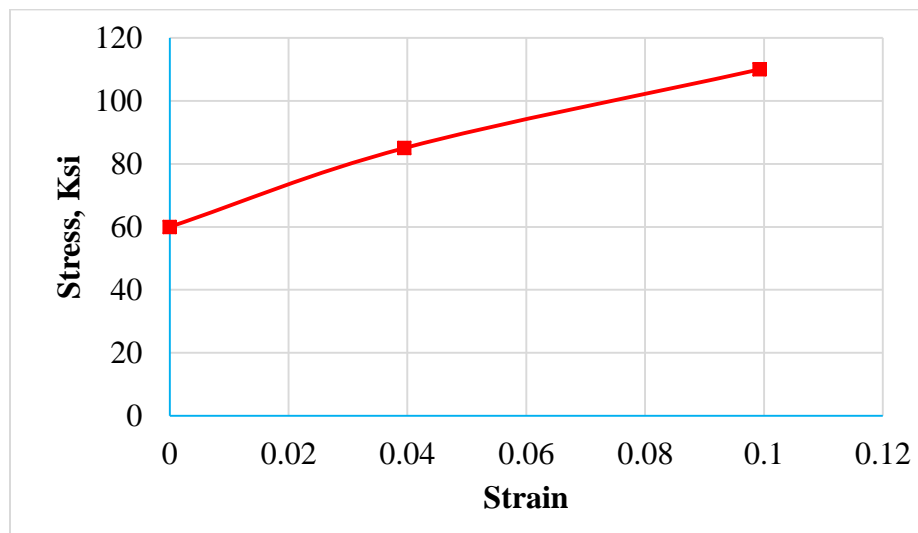


Figure 5.17 Stress- Strain for Concrete in Tension



(a)



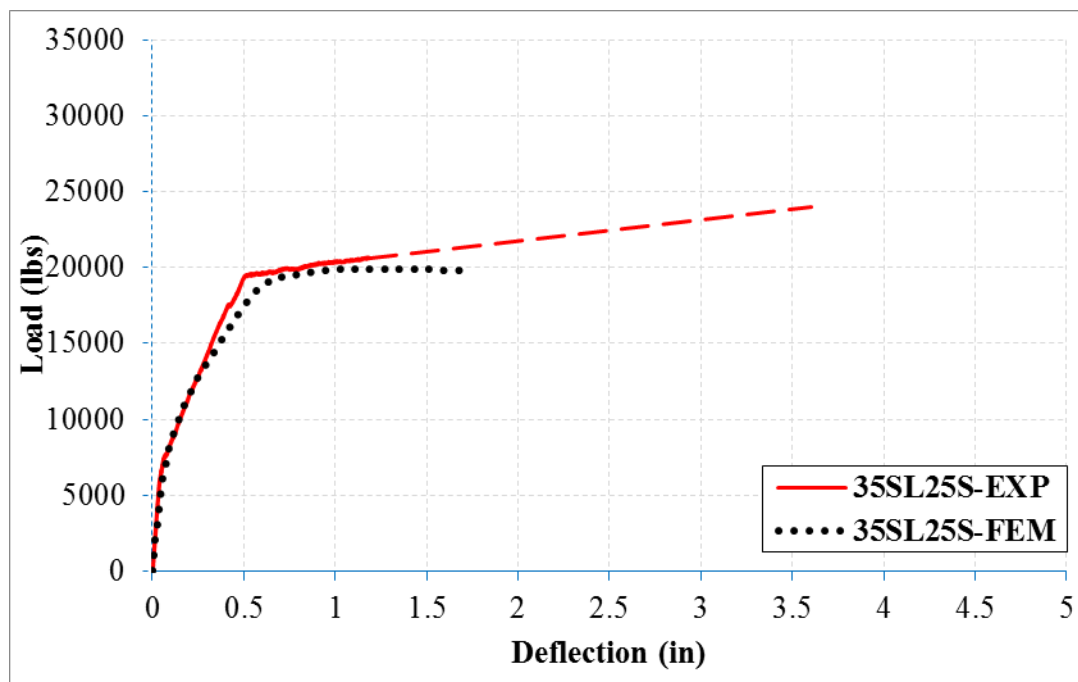
(b)

Figure 5.18 Stress-Stain for Steel: a) Stress-Strain; b) Stress-Plastic Strain

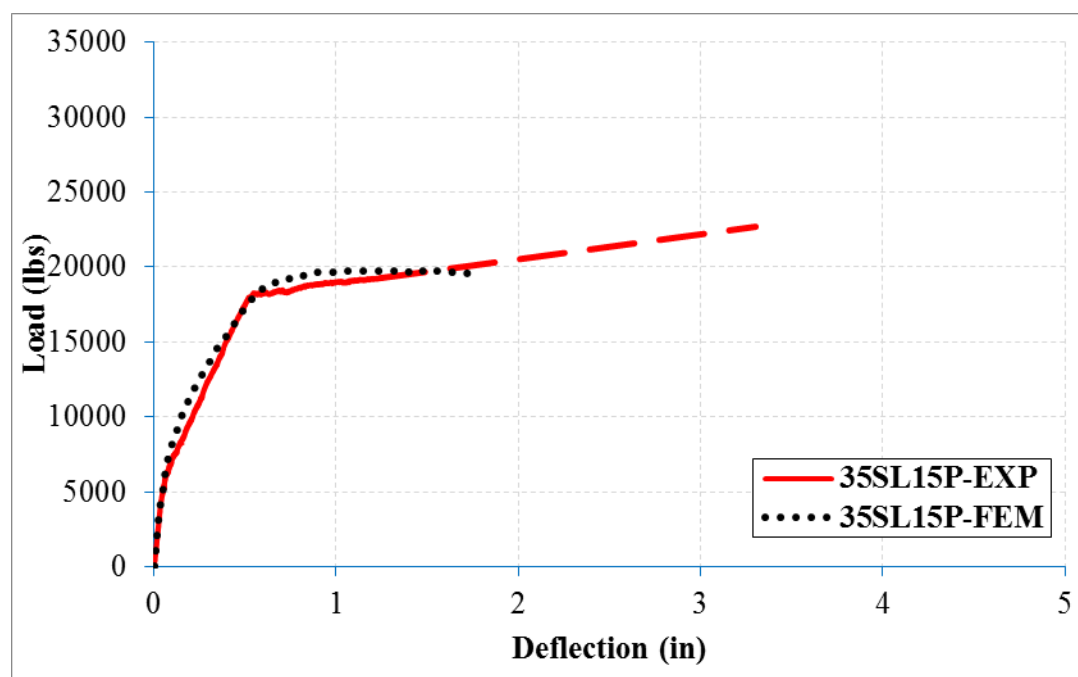
5.3.3 Results and Model Validation

The FE models' predictions are compared with the experimental results. Figures 5.19 through 5.21 show the predicted load-deflection response and the measured experimental for both control and repaired beams. Also, Figures 5.22 through 5.24 show the predicted steel tension strain in the middle at the center and the measured experimental for both control and repaired beams. The experimental data is shown with solid line while the dashed line is connecting the ultimate load and the deflection measured the taken video as explained previously. It is clear that there is a good correlation between the predicted models and experimental results. Hence, the finite element models are validated and capable of predicting the load-carrying capacity of the tested beams accurately.

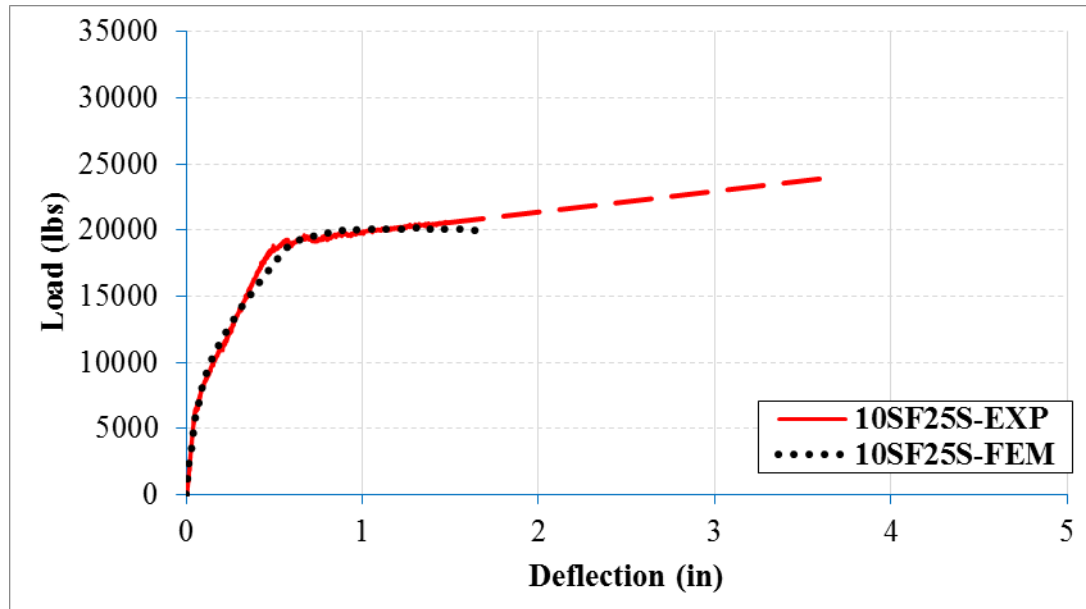
Figure 5.25 shows the comparison between the applied load and deflection for the best performing beams and the corresponding control one. The comparison demonstrates that the repaired beams have a higher cracking load and strain than to the control one. Such increase is expected to contribute to extending the life of the corroded member or structure at the service load which is the main point of this research. The nodal displacement value in the y direction for each beam specimen at failure is shown in Figure 5.26. As expected, the maximum displacement was reached at the middle beam (right edge of the half FEM beam).



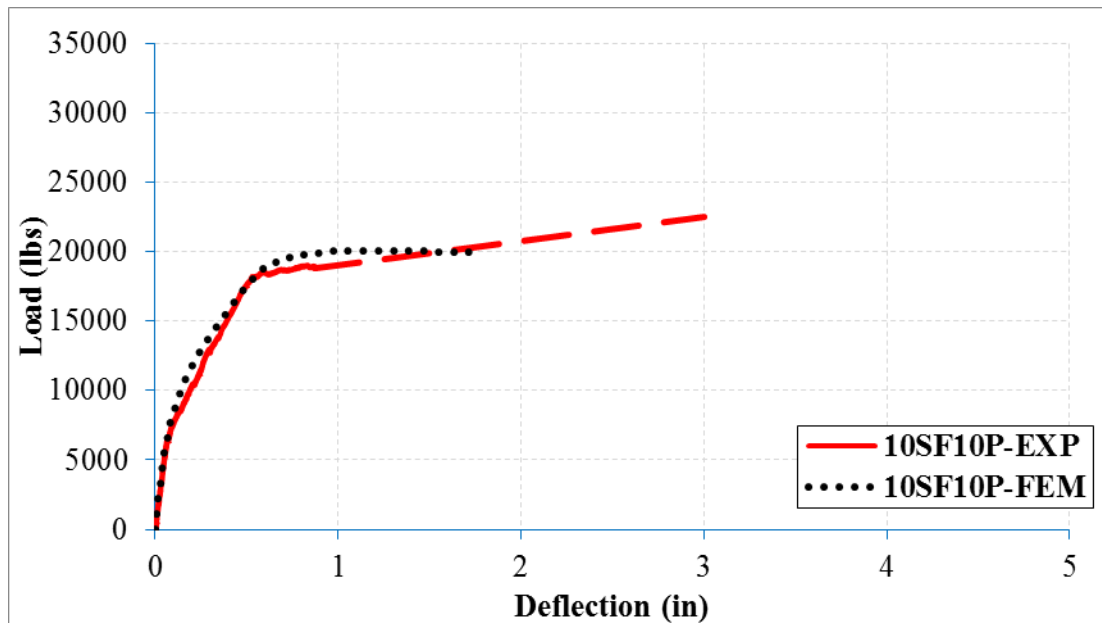
a) Beam Repaired with 35SL25S



b) Beam Repaired with 35SL15P

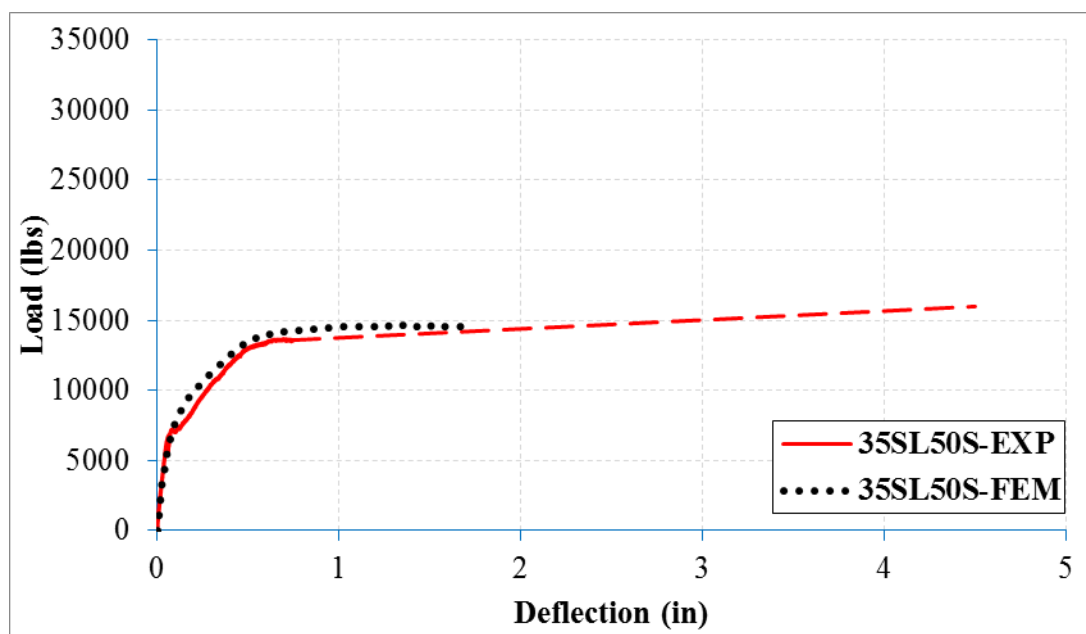


c) Beam Repaired with 10SF25S

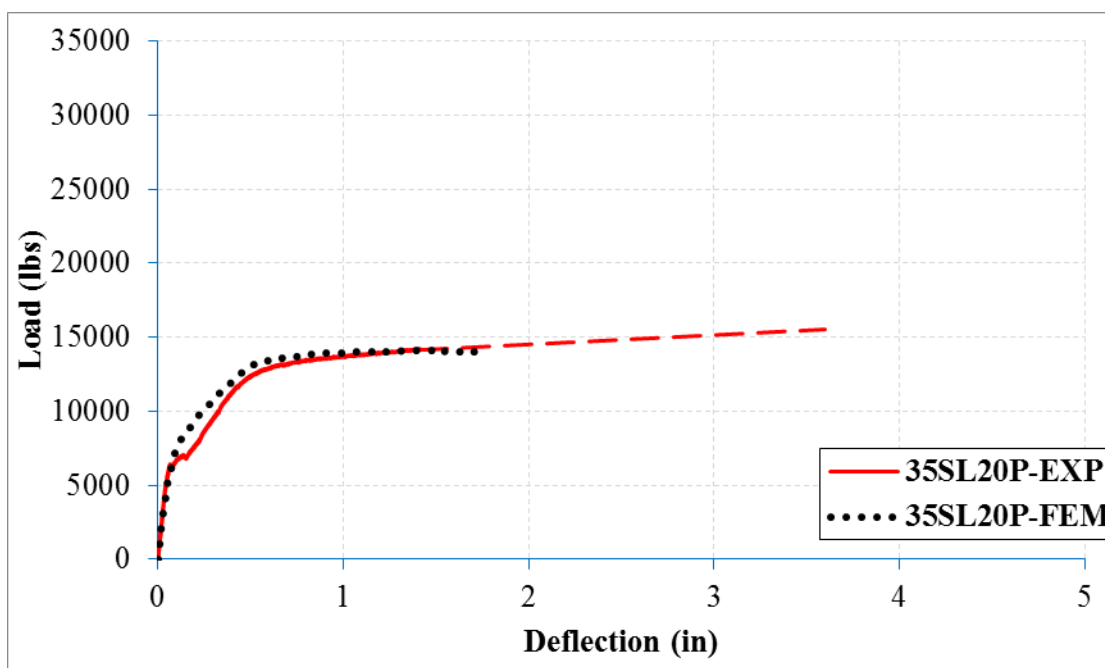


d) Beam Repaired with 10SF10P

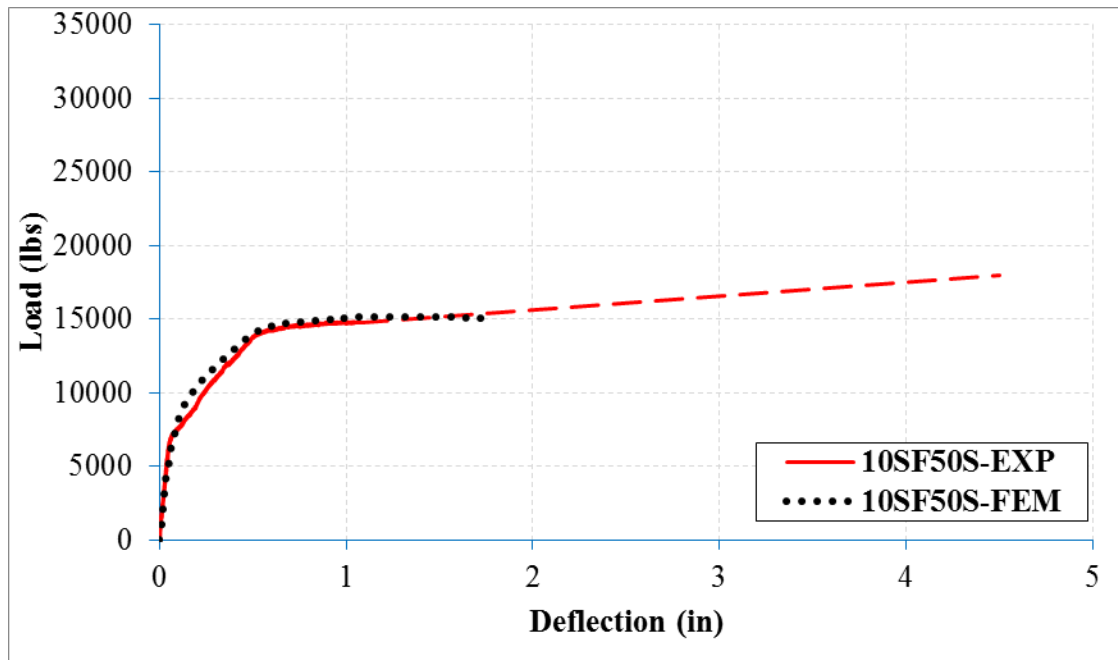
Figure 5.19 Applied Load and Deflection Relationship for the Repaired Beams Contain #4 Rebars ($A_s = 0.6 \text{ in}^2$): Comparison between FEM and Experimental Results



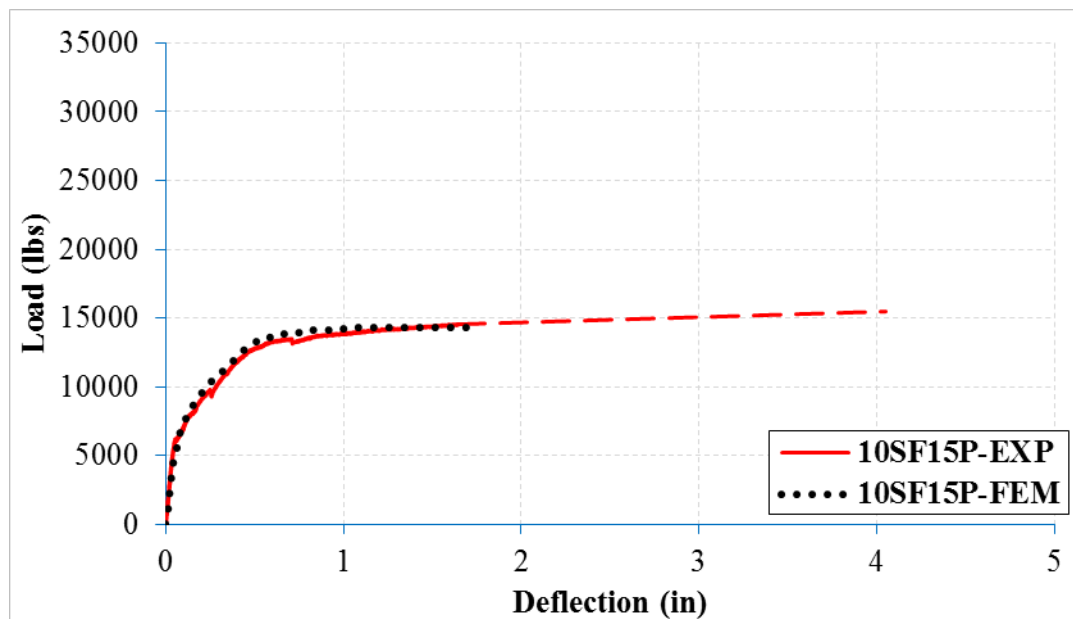
a) Beam Repaired with 35SL50S



b) Beam Repaired with 35SL20P

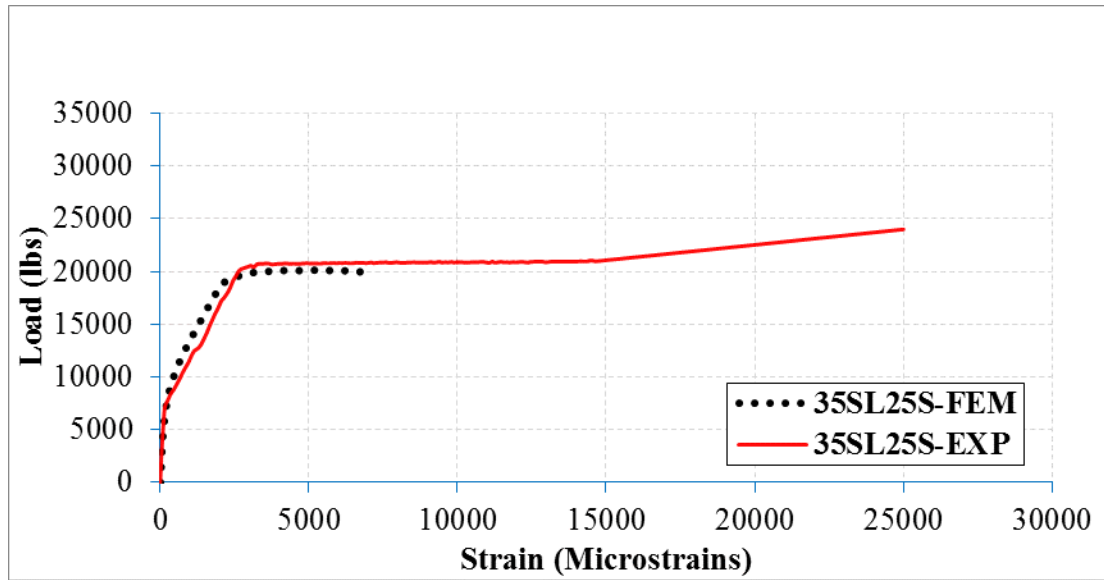


c) Beam Repaired with 10SF50S

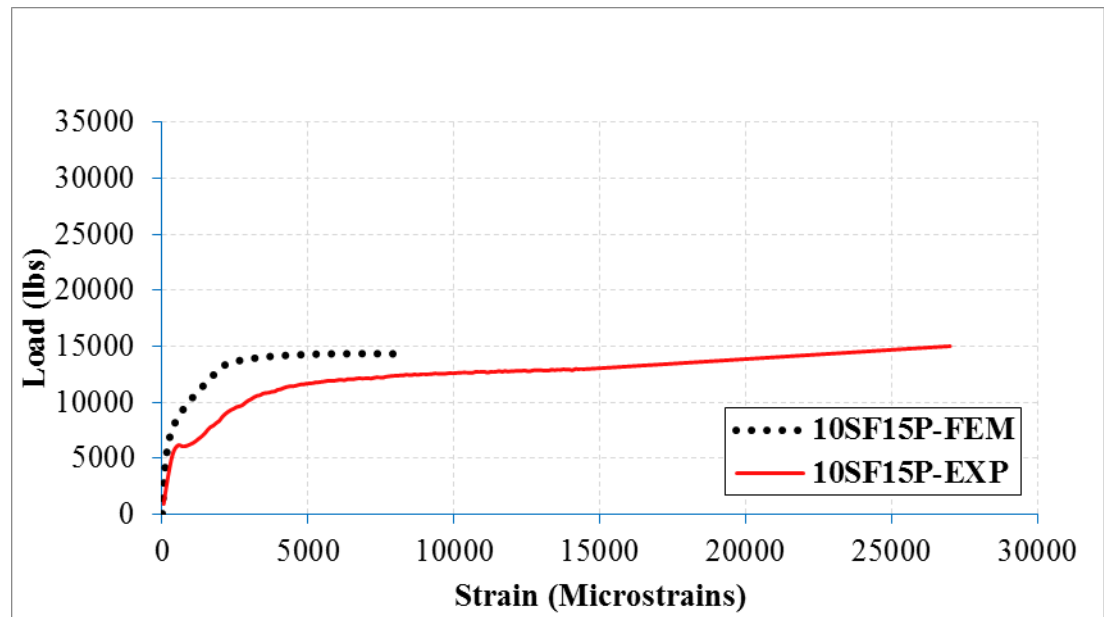


d) Beam Repaired with 10SF15P

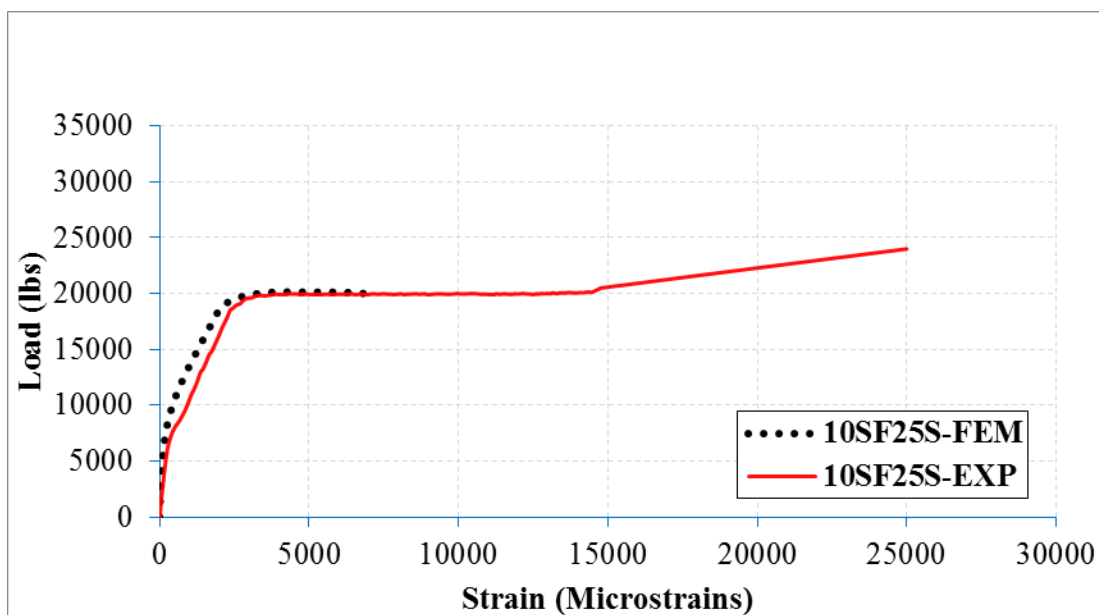
Figure 5.20 Applied Load and Deflection Relationship for the Repaired Beams Contain #3 Rebars ($A_s = 0.33 \text{ in}^2$): Comparison between FEM and Experimental Results



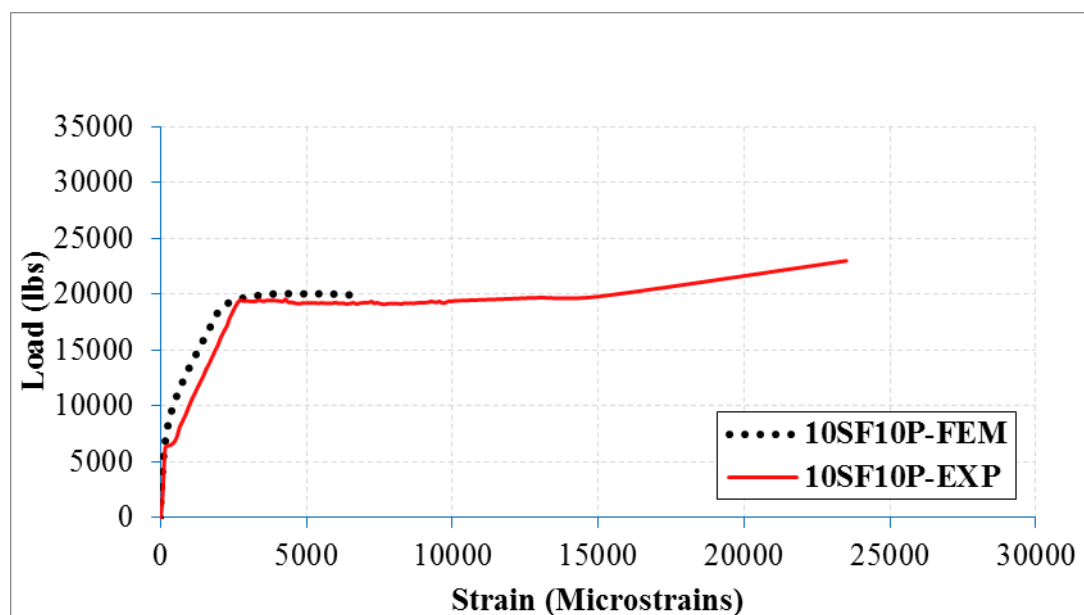
a) Beam Repaired with 35SL25S



b) Beam Repaired with 35SL15P

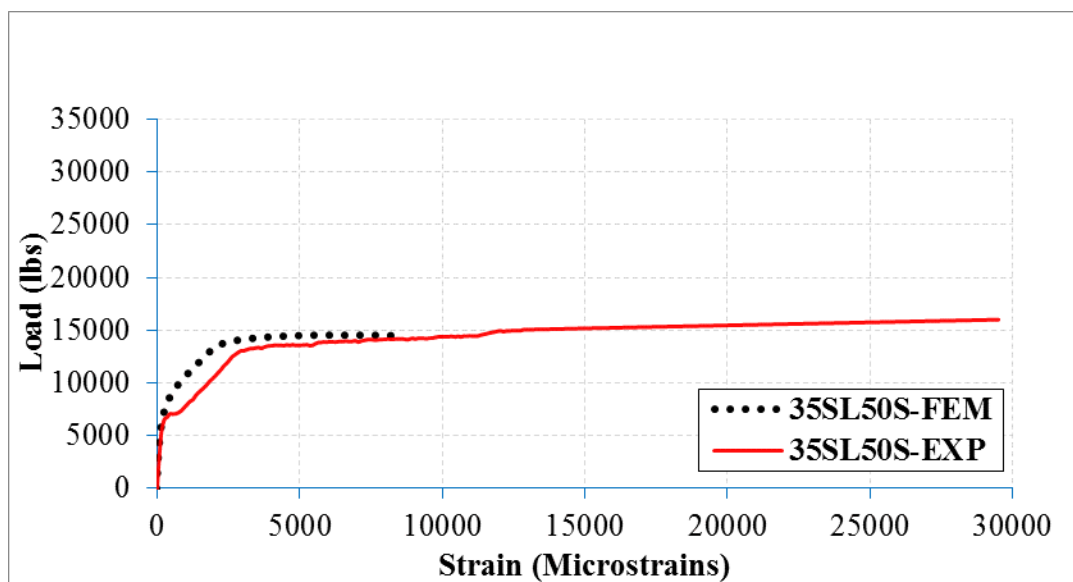


Beam Repaired with 10SF25S

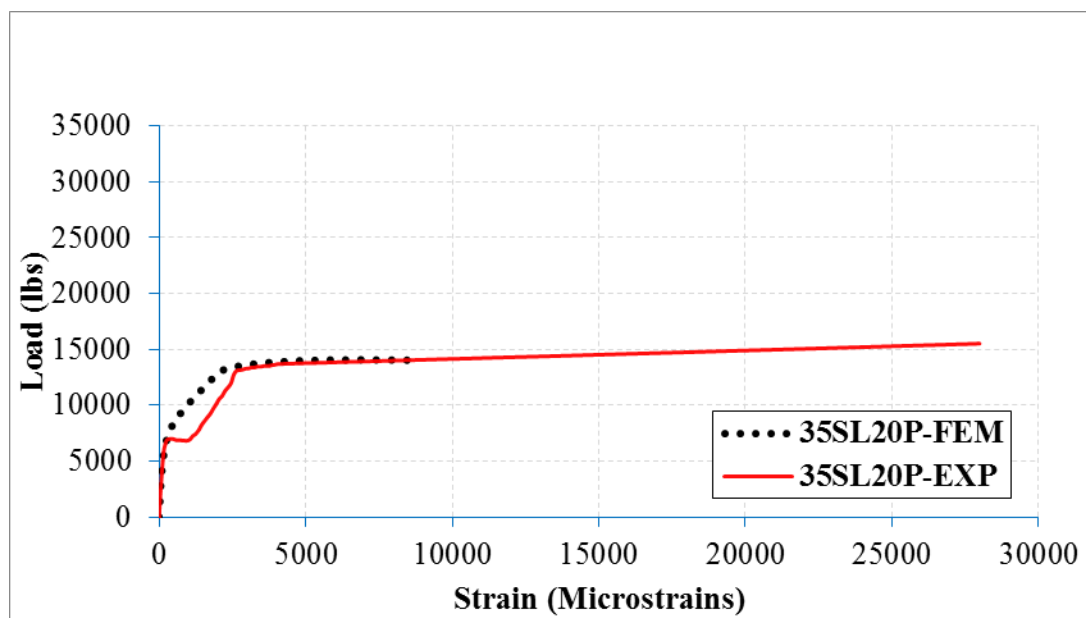


Beam Repaired with 10SF10P

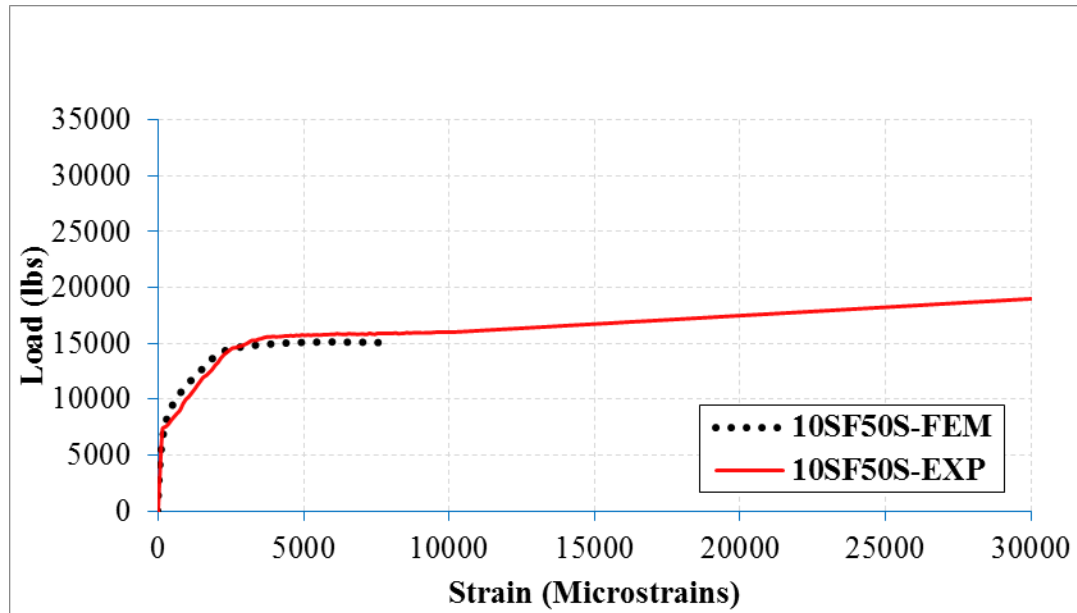
Figure 5.21 Applied Load and Rebar Tension Strain Relationship at Middle at Center for the Repaired Beams Contain #4 Rebars ($A_s = 0.6 \text{ in}^2$): Comparison between FEM and Experimental Results



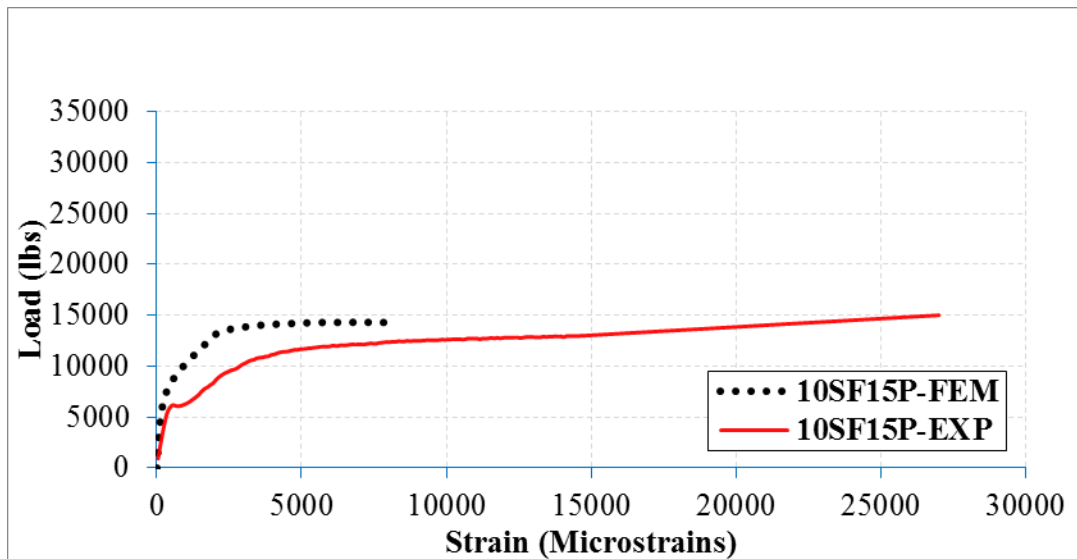
a) Beam Repaired with 35SL50S



b) Beam Repaired with 35SL20P



c) Beam Repaired with 10SF50S



d) Beam Repaired with 10SFL15P

Figure 5.22 Applied Load and Rebar Tension Strain Relationship at Middle at Center for the Repaired Beams Contain #3 Rebars ($A_s = 0.33 \text{ in}^2$): Comparison between FEM and Experimental Results

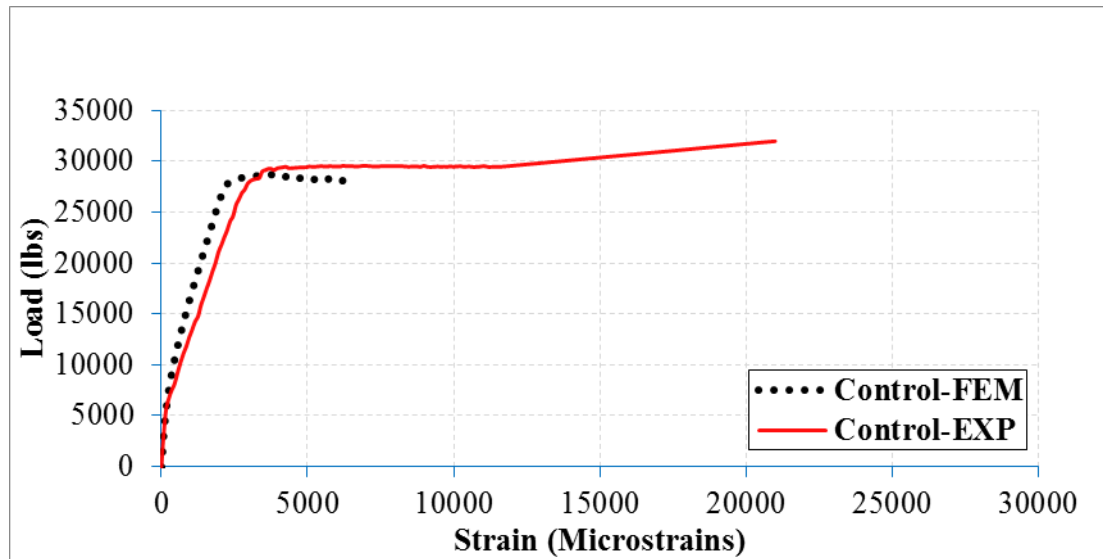


Figure 5.23 Applied Load and Rebar Tension Strain Relationship at Middle at Center for Control Beam Contains #5 Rebars ($A_s = 0.93 \text{ in}^2$): Comparison between FEM and Experimental Results

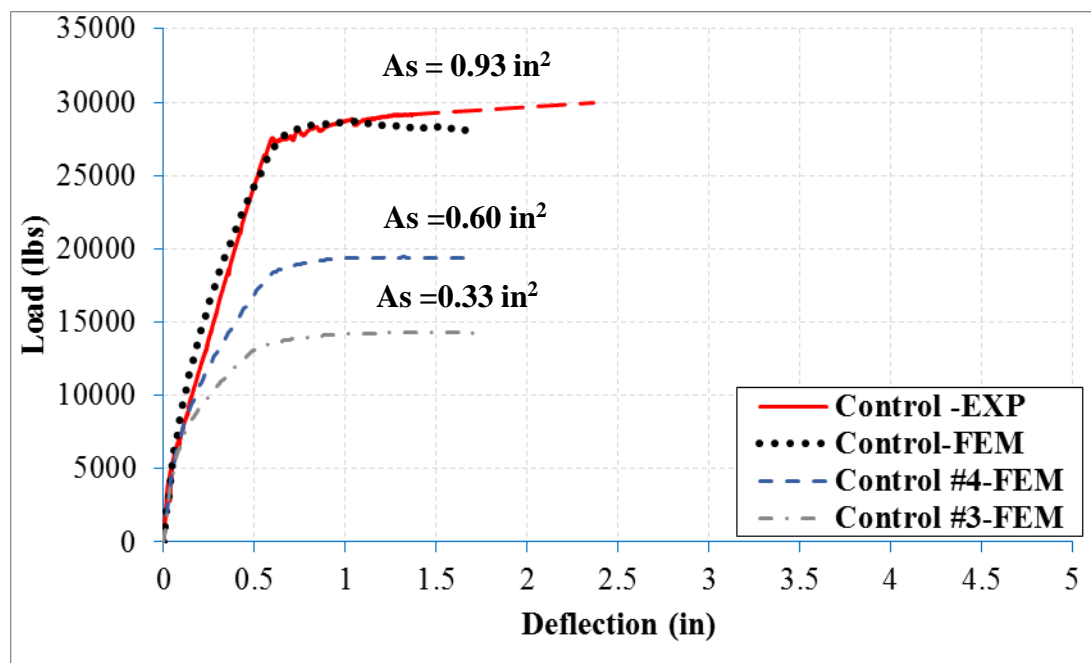


Figure 5.24 Applied Load and Deflection Relationship for the Control Beams: Comparison between FEM and Experimental Results

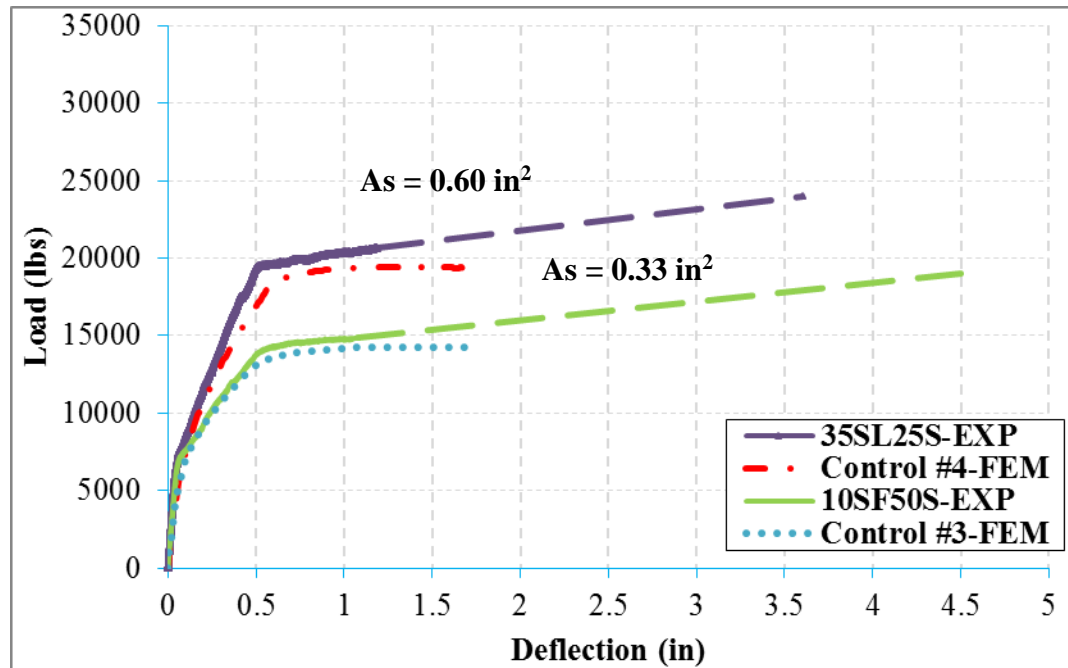
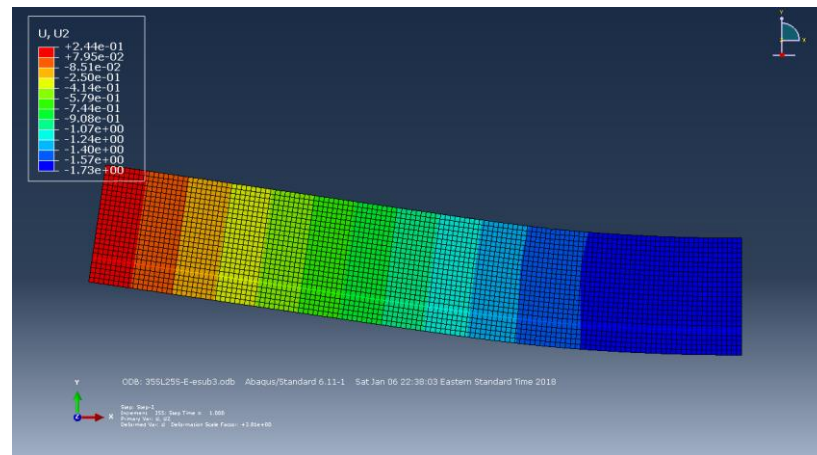
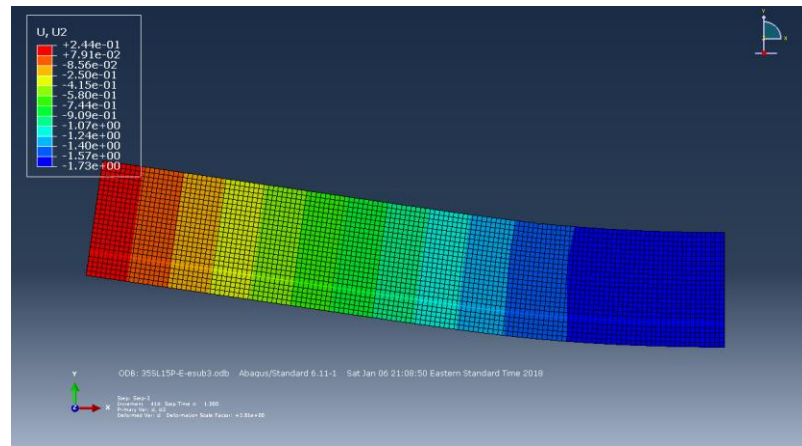


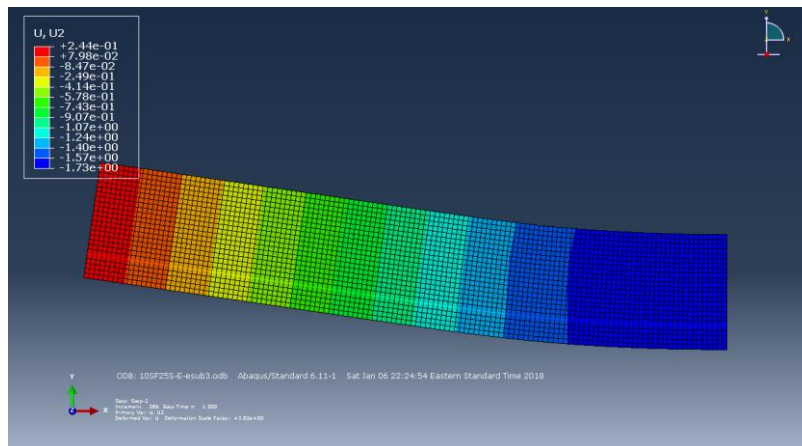
Figure 5.25 Applied Load and Deflection Relationship: Comparison between the Best Performing Beams and the Corresponding Control One



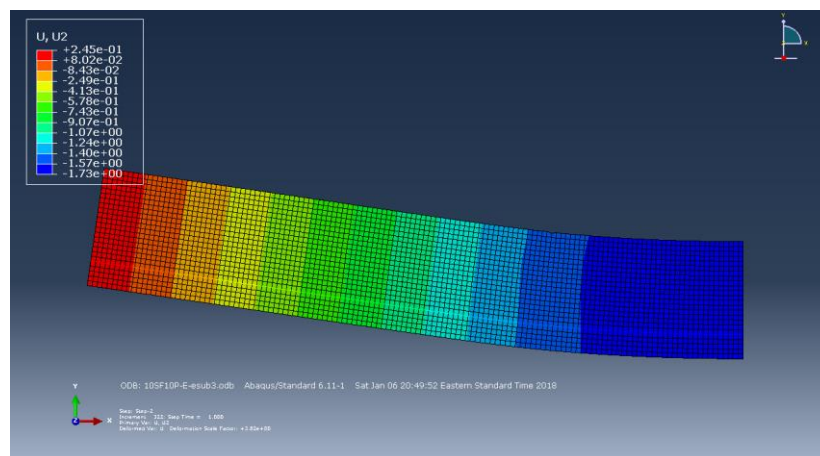
a) Beam Repaired with 35SL25S



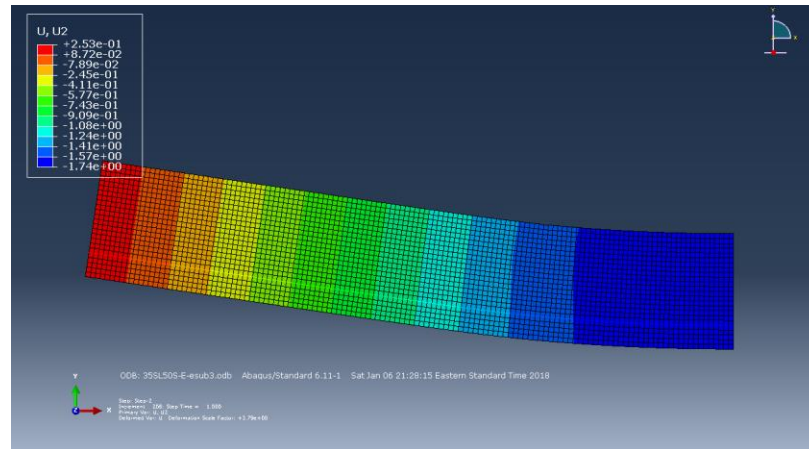
b) Beam Repaired with 35SL15P



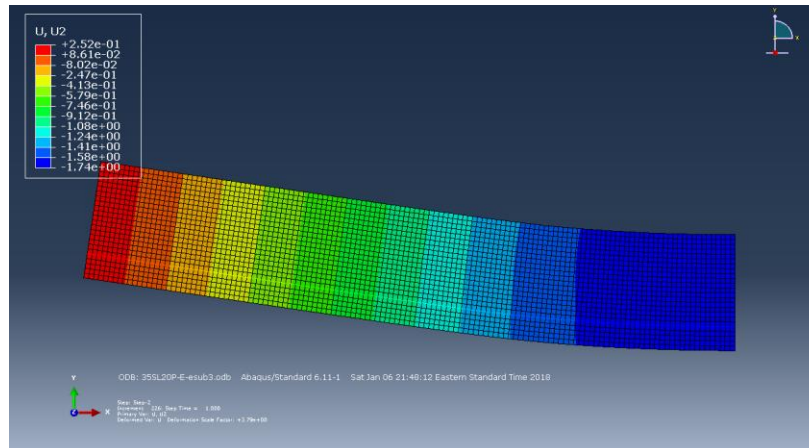
c) Beam Repaired with 10SF25S



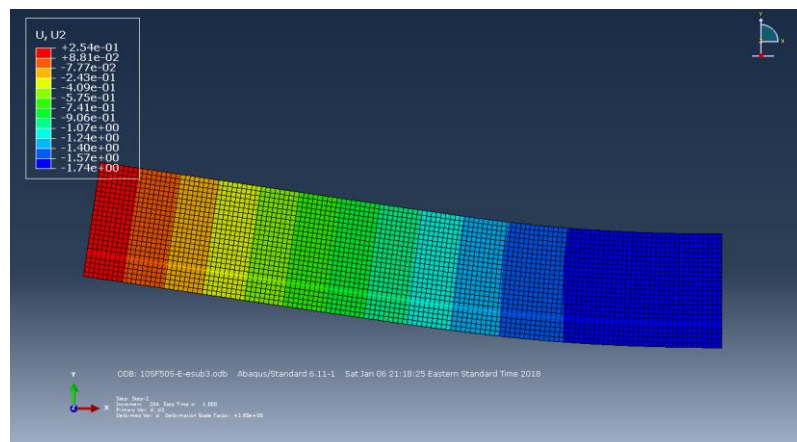
d) Beam Repaired with 10SF10P



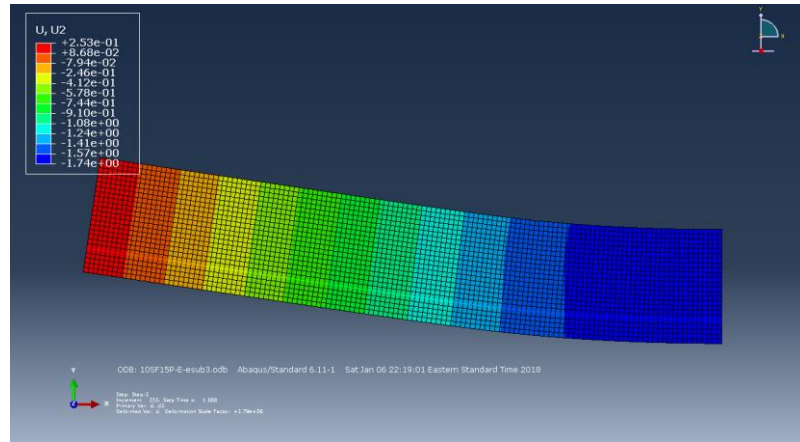
e) Beam Repaired with 35SL50S



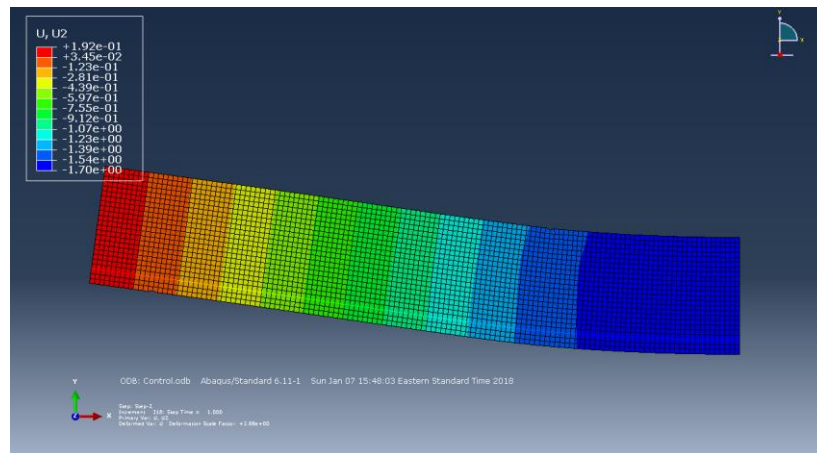
f) Beam Repaired with 35SL20P



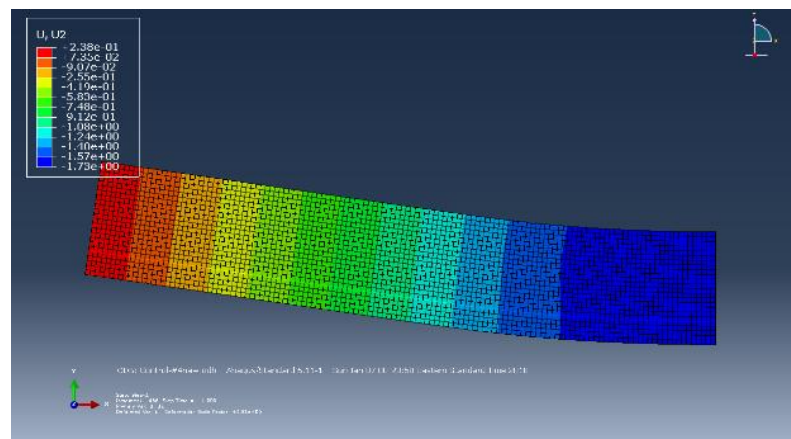
g) Beam Repaired with 10SF50S



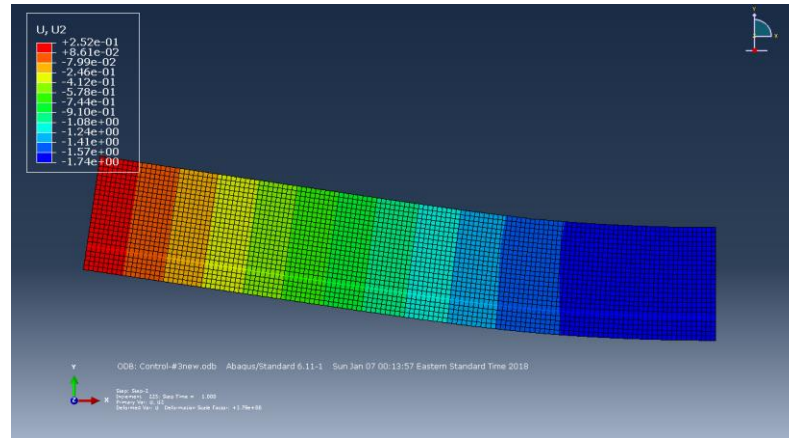
h) Beam Repaired with 10SF15P



i) Control Beam (#5 rebar)



j) Control Beam (#4 rebar)



k) Control Beam (#3 rebar)

Figure 5.26 Nodal Displacement (Deflection) in Y-Direction (U_y)

5.4 Parametric Study

5.4.1 Introduction

Having a model that accurately predicts the behavior of the beam, a parametric can easily performed which save time and money compared to the experiment. A parametric study was carried out to determine the sensitive parameters affecting the behavior of the repaired composite beams and the repair success using a number of simply supported composite. The investigated parameters are; the main steel reinforcement (A_s), the thickness of the repair layer (h_r), the concrete compressive strength of the repair layer (f'_{cr}), and the main steel reinforcement depth (d), as shown in Figure 5.27.

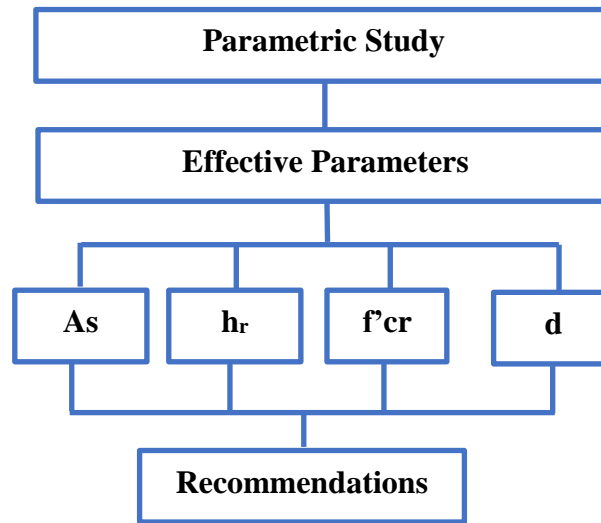


Figure 5.27 Flowchart for the Parametric Study

5.4.2 Main Steel Reinforcement (A_s)

Different rebar sizes (areas of steel reinforcement) were examined during this parametric study. Table 5.9 shows the properties and results of the beams. Increasing the area of main steel reinforcement (A_s) from 0.33 to 1.32 in² (from #3 to #6 rebar size) significantly increased the ultimate loads by 103 % as shown in Figure 5.28. While, such increase couldn't be established in the cracking load. Figure 5.28 also shows that the percentage increase in the cracking load was only 8 %.

5.4.3 Thickness of the Repair Layer (h_r)

In the experimental work, the thickness of the repair layer (h_r) was selected to be same for all the beams for comparison purposes. There is a need to study the behavior of the repaired beam with different thickness of the repair layer. During repairing process, the unsound concrete needs to be removed as an important step of the repair. In the case of corroded reinforcement, all surrounded concrete needs to be removed in order to clean the

corroded rebars. Hence, the thickness of the repair layer may vary and needs to be investigated. Different beams with different h_r were studied. The beams properties and results are also in Table 5.9. The results showed that increasing the thickness of the repair layer (h_r) from 1.5 to 4.5 in, significantly increased the cracking load by 36 % as demonstrated in Figure 5.29. On the other hand, there is no such enhancement in the ultimate load due to the increase in h_r .

5.4.4 Concrete Compressive Strength for the Repair Layer (f'_{cr})

Due to the availability of different repair materials, different compressive strength values of the repair layer can be obtained. Emmons et al. [1994], showed that the disparity in materials properties such as compressive strength could result in crack the concrete repair that leads to de-bonding at the interface between the substrate and the repair material. Thus, an investigation of using different concrete compressive strength for the repair layer (f'_{cr}) was carried out. The properties and results of the beams are shown in Table 5.9 and Figure 5.30. Increasing the f'_{cr} by 75 % (from 2600 to 4550 psi) increased the cracking capacity by 23 %. The increase of the f'_{cr} did not show any significant effect on the ultimate load as shown in Figure 5.30.

5.4.5 Main Steel Reinforcement Depth (d)

The effect of changing the depth of the main steel reinforcement (d) on the cracking and ultimate loads was studied as shown in Table 5.9. The results showed that increasing or decreasing d has no significant effect on the cracking load (Figure 5.31). While increasing (d) by 22 % (from 9 to 11 in) increased the ultimate load by 22 %.

Table 5.9 Properties and Results of the Studied Beams

Beam	As (in²)	hr (in)	f'cr (psi)	d (in)	Pcr (lbs)	Pu(lbs)
B1.1	0.33	3.5	2600	9.5	5100	14567
B1.2	0.60	3.5	2600	9.5	5300	19625
B1.3	0.93	3.5	2600	9.5	5400	26340
B1.4	1.32	3.5	2600	9.5	5500	29640
B2.1	0.60	1.5	2600	9.5	4500	19611
B2.2	0.60	3.0	2600	9.5	4800	19620
B2.3	0.60	3.5	2600	9.5	5300	19625
B2.4	0.60	4.5	2600	9.5	6100	19767
B3.1	0.60	3.5	2600	9.5	5300	19625
B3.2	0.60	3.5	3250	9.5	5600	19617
B3.3	0.60	3.5	3900	9.5	5900	19744
B3.4	0.60	3.5	4550	9.5	6500	19762
B4.1	0.60	3.5	2600	9	5100	18597
B4.2	0.60	3.5	2600	9.5	5300	19625
B4.3	0.60	3.5	2600	10	5300	20736
B4.4	0.60	3.5	2600	11	5400	22607

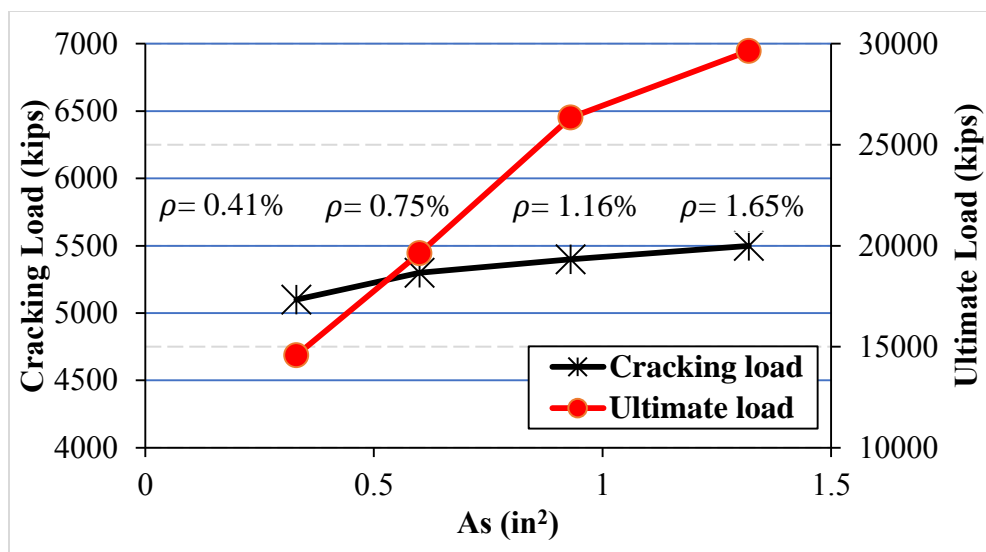


Figure 5.28 Effect of Variation of (A_s) on Cracking and Ultimate Loads

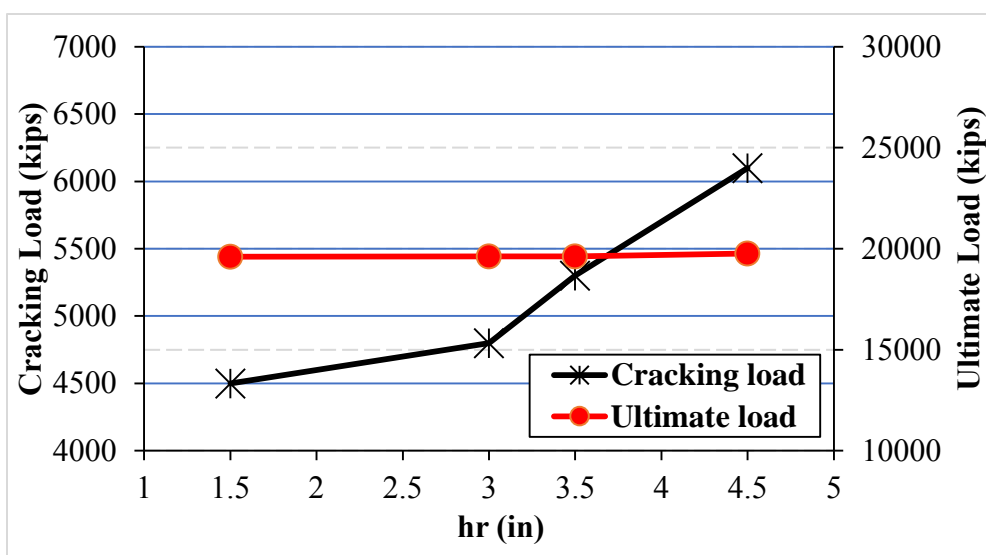


Figure 5.29 Effect of Variation of (h_r) on Cracking and Ultimate Loads

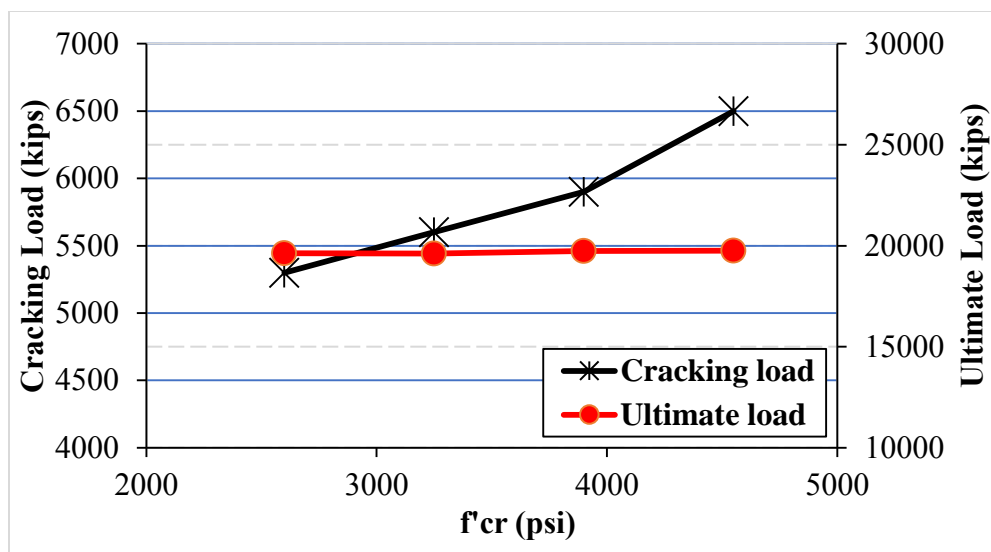


Figure 5.30 Effect of Variation of (f'_{cr}) on Cracking and Ultimate Loads

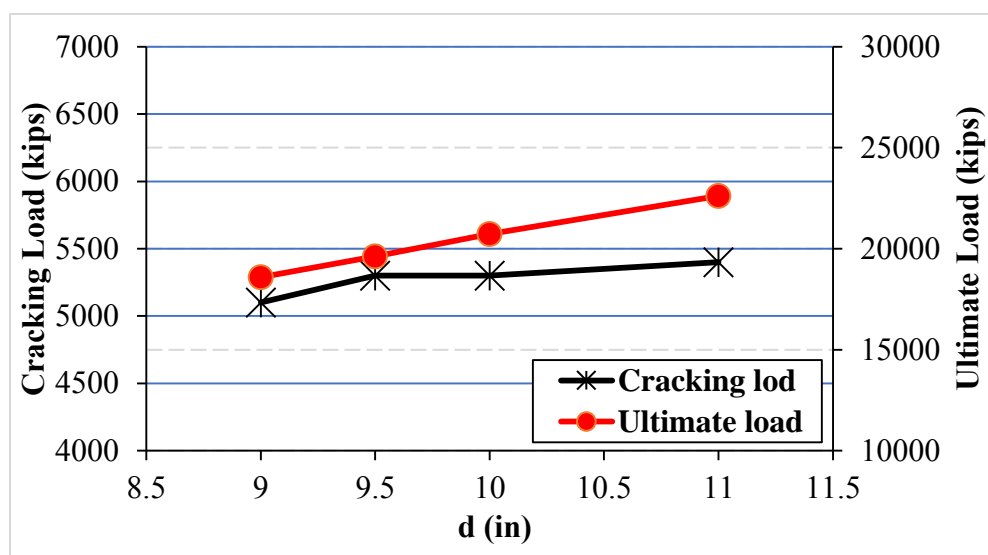


Figure 5.31 Effect of Variation of (d) on Cracking and Ultimate Loads

5.5 Summary

5.5.1 Code Predictions

From the prediction results, it can be seen that all of the three codes (ACI 318 [2014], CSA A23.3 [2004], and AASHTO-LRFD [2012]) were non-conservative in estimation the cracking load in both control and repaired beams. The average of ($P_{cr \text{ exp}}/P_{cr \text{ pred}}$) for the ACI 318 [2014], CSA A23.3 [2004], and AASHTO-LRFD [2012] were 0.93, 0.96, and 0.91, respectively. It can be concluded that the CSA A23.3 [2004] provides the best prediction. On the other hand, the ACI 544 [2011] code was conservative and underestimated the cracking load for both control and repaired beams.

The results of the predicted ultimate capacities and the comparison with the experimental capacities were shown a consistent conservative and safe compared with experimental capacities with a mean ratio of $P_{u \text{ Exp}}/P_{u \text{ ACI 318}}$ equal to 1.4.

All three models, ACI 318[2014], CSA A23.3 [2004], and AASHTO LRFD [2012] did underestimate the deflection. These codes were more non-conservative in predicting the deflection of the repaired beams comparing with control one. The degree of underestimation of the repaired beams was found to be higher by 13-27 % comparing to the control beams.

5.5.2 Finite Element Model and the Parametric study

In this study, eleven FEMs were developed to simulate the response and predict the behavior of the control and repaired beams with FR-SCC. These models were validated by comparing the FE results with the obtained experimental data that was discussed in chapter 3. The model results have shown good agreement up to the measured experimental deflection. Finally, the developed and verified FEMs could be used as a tool to further

investigate the behavior of repaired and unrepaired concrete beams under static loading and as an alternative to experimental testing, which is usually more expensive and time-consuming.

From the parametric study, it was observed that the parameters that affect the cracking load are h_r and f'_{cr} . It was found that increasing the h_r from 1.5 to 4.5 in, significantly increased the cracking load by 36 %. While increasing the f'_{cr} from 2600 to 4450 psi, increased the cracking capacity by 23 %. On the other hand, the effective parameters that enhancing the ultimate load are A_s and d . Increasing the area of main steel reinforcement A_s from 0.33 to 1.32 in² (from #3 to #6 rebar size) significantly increased the ultimate loads by 103 %. While increasing d from 9 to 11 in, increased the ultimate load by 22 %.

CHAPTER 6 CONCLUSIONS

The following are the main findings that can be drawn from the experimental results in this research:

1. The incorporation of PPF would largely affect the concrete workability and passing ability in comparison with STF. Therefore, the maximum fiber percent for the designed mixtures should not exceed 0.5 and 0.2 for STF and PPF, respectively.
2. The type of fiber, fiber content, and type of pozzolanic materials has impacted the mechanical properties of the concrete mixtures. For example, the use of fiber in FR-SCC has increased the compressive strength by a maximum increase of 71.7 % for 10SF50S mixture at 28 days in comparison with 10SF mixture. The compressive strength was also slightly increased with the increase of fiber content. Mixtures with SF showed higher compressive strength compared to mixtures containing SL. The addition of STF increases the splitting tensile strength of concrete significantly. The percentage increase in splitting tensile strength was found to be increased with the increase in fiber content. At 28 days, the percentage increase in splitting tensile strength of 10SF50S concrete mixture over its reference (10SF) was 70.4 %. The modulus of rupture also increased with the increase of fiber percentage. The results also show that mixtures with SF exhibited better flexural strength than mixtures with SL. The addition of fiber resulted in a slight increase in the modulus of elasticity. SF mixtures showed slightly higher results than SL mixtures.
3. A reduction of 37 % in free shrinkage obtained when using 0.5 % of STF in the 35SL50S mixture comparing to 35SL mixture which is the control (without fiber) at 56 days. Mixtures with SL exhibited lower shrinkage than mixtures with SF. This is mainly

attributed to the high fineness of the SF material. The results also showed that the incorporation of both types of fiber reduced the shrinkage significantly comparing with mixtures without fibers. By reducing the shrinkage crack sizes and the distribution, the repaired structural element will be more durable.

4. In general, all optimized FR-SCC mixtures passed the compatibility test. The failure location was in the middle which indicates a good compatibility.

5. All the FR-SCC mixtures showed a good bond with the substrate which is a very important factor for the successful repair. In general, the bond strength found to be increased with the increase of the fiber content and the maximum percentage increase was 59 % for mixture 10SF15P compared to 10SF10P mixture.

6. The flexural cracking load ranged between 4,900 and 6,000 lbs for repaired, and 4,600 and 4,700 lbs for the reference control beams. The maximum increase in cracking load is 29 % for the repaired beams comparing to control beams. While, the ultimate load ranged between 15,492 and 26,200 lbs for repaired, and 30,000 and 32,000 lbs for the reference control beams. The 10SF25 mixture that used for repairing the beams with 35 % lost in reinforcement area due to corrosion resulted in 84.5 % of the ultimate strength of the control beams. This proves that the repair material markedly improves the repaired area properties especially the tensile strength and such improvement is vital in extending the life of the repaired structure under the service loads.

7. The ACI 318 [2014], CSA A23.3 [2004], and AASHTO-LRFD [2012] were non-conservative in estimation the cracking load in both control and repaired beams. While, ACI 544 [2011] code underestimated the cracking load for both control and repaired beams; hence, provides much safer in prediction the cracking load for the repaired beams

comparing to the other codes. On the other hand, the ACI 544 [2011] showed a conservative safe prediction for the ultimate load.

8. All three codes, ACI 318 [2014], CSA A23.3 [2004], and AASHTO-LRFD [2012] underestimated the deflection. These codes were more non-conservative in predicting the deflection of the repaired beams comparing with control beams. The degree of underestimation of the repaired beams was found to be higher by 13-27 % comparing to the control beams.

9. The developed models were effective in producing good prediction in the elastic and plastic ranges of the applied load.

10. The most effective parameters on the cracking load are h_r and f'_{cr} . While, the effective parameters that enhancing the ultimate load are A_s and d .

REFERENCES

- AASHTO (2012) *AASHTO LRFD Bridge Design Specifications*, Customary U.S. Units, American Association of State Highway and Transportation Officials.
- Abaqus (2011) Version 6.11, *Theory Manual*, Dassault Systems Simulia Corporation.
- Abdul-Hameed, H. (2010) *Evaluation of Pozzolanic Repair Materials by Different Test Methods*, Iraqi Journal for Mechanical and Materials Engineering. Special Issue (A), pp. 1-17.
- ACI 318 (2014) *Building Code Requirements for Structural Concrete and Commentary*, ACI Manual of Concrete Practice, American Concrete Institute, Farmington Hills, Michigan.
- ACI 363 (2011) *Report on High-Strength Concrete*, ACI Manual of Concrete Practice, Part 3, American Concrete Institute, Farmington Hills, Michigan.
- ACI 544 (2011) *Fiber Reinforced Concrete*, ACI Manual of Concrete Practice, Part 6, American Concrete Institute, Farmington Hills, pp. 11.
- Alsayed, S.H. (2005). *Durability of the Repair Materials and Repaired Structures*, Senior Project, King Saud University, pp. 1-8.
- American Concrete Pavement Association (ACPA). (1998), *Guidelines for Partial-Depth Repair*, Technical Bulletin TB-003P, American Concrete Pavement Association, Arlington Heights, Illinois.
- ASCE (2017) *Infrastructure Report Card*. (<http://www.infrastructurereportcard.org/>).
- Barlow, J. (1976). *Optimal stress locations in finite element models*. International Journal for Numerical Methods in Engineering, 10(2), 243-251.
- Blaga, A., and Beaudoin, J. (2005). *Polymer-Modified Concrete*, National Research Council, Canada, pp. 1-2.
- Branson, D.E. (1977). *Deformation of concrete structures*. McGraw-Hill Companies. New York, 546 p.
- Brain, L.L., David, W.F., and Ramon, L.C. (1998), *Material Selection Guideline for Structural Concrete Repair*, Center for Transportation Research, The University of Texas at Austin, pp.97-98.
- Brown, M.C., Ozyildirim, C., & Duke, W. L. (2010). *Investigation of fiber-reinforced self-consolidating concrete* (No. FHWA/VTRC 10-R8).
- Buchanan, A. H. (2001). *Structural design for fire safety* (Vol. 273). New York: Wiley.
- CSA A23.3 (2004) *Design of Concrete Structures*, Canadian Standards Association, 3rd Edition, Rexdale, Ontario, 240 p.
- Cusson, D. and Mailvaganam, N. (1996), *Durability of Repair Materials*, Concrete International, 18(3), pp 34-38.

- Czarnecki, L., Garbacz, A., Lukowski, P., and Clifton, J.R. (1999). Polymer composites for Repairing of Portland Cement Concrete: Compatibility project, NISTIR 6394, Building and Fire Research Laboratory, NIST, Gaithersburg, MD 20899
- Danish Standards Association. (2004). *Repair of concrete structures to EN 1504*. Elsevier. pp. 214.
- Ehlen, M.A. (1997). *Life-Cycle Costs of New Construction Materials*, Journal of Infrastructure Systems, 3(4), pp. 129-133.
- Emberson, N.K., and Mays, G.C. (1990), Significance of Property Mismatch in the Patch Repair of Structural Concrete Part 1: Properties of Repair Systems, Magazine of Concrete Research, 42(152), pp. 147-160
- Emmons, P.H. (1993), Concrete Repair and Maintenance Illustrated, Construction Publishers and Consultants, Kingston, MA, pp. 100-136.
- Emmons, P.H. (2006). Vision 2020 Repair. *Protection Council, Strategic Development Council, American Concrete Institute's Concrete Research and Education Foundation (Jul. 1, 2006)* http://www.concretesdc.org/_pdfs/Vision2020-Version1.0_%20May2006.pdf
- Gergely, P., & Lutz, L. A. (1968). *Maximum crack width in reinforced concrete flexural members. Causes, mechanism, and control of cracking in concrete*, SP-20, American Concrete Institute, Farmington Hills, Mich., p. 87-117.
- Hassan, M. S., Mansi, A. S., and Abdul-Hameed, H. A. (2010). *Factors Affecting Compatibility between (S.B.R) Polymer Repair Materials and Concrete Substrate*, Engineering & Technology, the scientific journal of the University of Technology – Baghdad 28(14), pp4853-4865.
- Henager, C. H., & Doherty, T. J. (1976). *Analysis of reinforced fibrous concrete beams*. Journal of the Structural Division, 102(1), 177-188.
- Hillerborg, A., Mod  er, M., & Petersson, P. E. (1976). *Analysis of crack formation and crack growth in concrete by means of fracture mechanics and finite elements*. Cement and concrete research, 6(6), 773-781.
- Hilsdorf, H., & Kropp, J. (Eds.). (2004). *Performance criteria for concrete durability* (Vol. 12). CRC Press. Pp 200.
- Hwang, S. D., & Khayat, K. H. (2009). Durability characteristics of self-consolidating concrete designated for repair applications. *Materials and Structures*, 42(1), 1-14.
- James. D., (2009) *Evaluation and Repair of Concrete Structures*”, ASCE Construction Research Congress, Seattle, U.S. Army Corps of Engineers, Washington, pp. 6-17.
- Jankowiak, T., & Lodygowski, T. (2005). *Identification of parameters of concrete damage plasticity constitutive model*. Foundations of civil and environmental engineering, 6(1), 53-69.
- Kassimi, F. (2013). *Development and performance of fiber-reinforced self-consolidating concrete for repair applications*. Ph.D. Dissertation, University of Sherbrooke, Canada.

- Kassimi, F., El-Sayed, A. K., & Khayat, K. H. (2014). Performance of Fiber-Reinforced Self-Consolidating Concrete for Repair of Reinforced Concrete Beams. *ACI Structural Journal*, 111(6).
- Khayat, K.H. (1998, August). Use of Self-Consolidating Concrete in Canada. *In International Workshop on Self-compacting concrete* (Vol. 23, p. 26).
- Khayat, K.H. (1999). Workability, testing, and performance of self-consolidating concrete. *ACI Materials Journal*, 96(3).
- Khayat, K.H. (2006) GCI340: Technology of Concrete, Graduate and Undergraduate course (in French), Université de Sherbrooke, Québec, Canada.
- Khayat, K.H., Kassimi, F., & Ghoddousi, P. (2014). Mixture Design and Testing of Fiber-Reinforced Self-Consolidating Concrete. *ACI Materials Journal*, 111(2).
- Khayat, K.H., Petrov, N., Morin, A. J. R., & Thibault, M. (2005). Performance of SCC used in the repair of retaining wall elements. *SCC 2005*, 1003-1013.
- Kamal, M.M., Safan, M. A., Etman, Z. A., & Kasem, B. M. (2014). Mechanical properties of self-compacted fiber concrete mixes. *HBRC Journal*, 10(1), 25-34.
- Steven, H.K., Beatrix, K., & William, C. P. (2003). Design and control of concrete mixtures. *PCA: Portland Cement Association*, 153.
- Kosmatka, S.H., & Panarese, W. C. (2002). Design and control of concrete mixtures.
- Kumar, V., Agrawal, R., Nautiyal, B.D. and Sigal, D. (1993). *Structural Properties of SFRC*. International Symposium of Innovative World of Concrete (ACI-IWC-93), Part 3, pp. 99-108.
- MacGregor, J. G. (2012). *Reinforced concrete: mechanics and design*.
- Marchand, J., Odler, I., & Skalny, J. P. (2003). *Sulfate attack on concrete*. CRC Press. pp. 217.
- Mangat, P.S., & Limbachiya, M. K. (1995). Repair material properties which influence long-term performance of concrete structures. *Construction and Building Materials*, 9(2), 81-90.
- Mansi, A.S., (2010). *Bond Strength Assessment for Different Types of Repair Materials*, Engineering & Technology, the scientific journal of the University of Technology –Baghdad 28(21), pp. 6325-6336.
- Mehta, P.K., & Monteiro, P. J. (2006). *Concrete: microstructure, properties, and materials* (Vol. 3). New York: McGraw-Hill.
- Nassif, H.H., & Najm, H. (2004). Experimental and analytical investigation of ferrocement–concrete composite beams. *Cement and Concrete Composites*, 26(7), 787-796.
- Nawy, E.G. (Ed.). (2008). *Concrete construction engineering handbook*. CRC press.
- Newman, J., & Choo, B.S. (Eds.). (2003). *Advanced concrete technology 1: Consistent Materials*. Butterworth-Heinemann.

- Newman, J., & Choo, B.S. (Eds.). (2003). *Advanced concrete technology 2: Concrete Properties*. Butterworth-Heinemann. P. 8/3-8/4.
- Newman, J., & Choo, B.S. (Eds.). (2003). *Advanced concrete technology 3: Processes*. Butterworth-Heinemann.
- Newman, J., & Choo, B.S. (Eds.). (2003). *Advanced concrete technology 4: Testing and Quality*. Butterworth-Heinemann.
- Neville, A. M., & Brooks, J.J. (2010). *Concrete technology*. Harlow: Longman Scientific & Technical.
- Ozyildirim, C., *Use of SCC for the Repair of Bridge Substructures*, Presentation, ACI Spring Convention 2013.
- Pattnaik, R. (2006). *Investigation into Compatibility between Repair Material and Substrate Concrete Using Experimental and Finite Element Method*. Ph.D. Thesis, Clemson University
- Portland Cement Association (2002). *Concrete information: Types and causes of concrete deterioration*, PCA R&D Serial No. 2617.
- Poston, R. W., Kesner, K., McDonald, J. E., Vaysburd, A. M., & Emmons, P. H. (2000). Selecting Durable Repair Materials: Performance Criteria Laboratory Results. *Concrete International*, 22(11), 21-29.
- Poston, R.W., Kesner, K., McDonald, J. E., Vaysburd, A. M., & Emmons, P. H. (2001). Concrete Repair Material Performance-Laboratory Study. *ACI Materials Journal*, 98(2).
- Robins, P.J., & Austin, S. A. (1995). A unified failure envelope from the evaluation of concrete repair bond tests. *Magazine of Concrete Research*, 47(170).
- Scrivener, K.L. (2003). *Advanced Concrete Technology: Constituent Materials* [M]. Butterworth-Heinemann, pp. 2/19
- Swathi, P. (2004) *Investigating the Role of Material Properties and Their Variability in the Selection of Repair Materials*, M.Sc. Thesis, Purdue University, August, pp. 77-79.
- Jenq, Y. S., & Shah, S. P. (1986). Crack propagation in fiber-reinforced concrete. *Journal of Structural Engineering*, 112(1), 19-34.
- Vandewalle, L. (2002). Design of steel fibre reinforced concrete using the sigma-w method: principles and applications. *Materials and Structures*, 35(249), 262-278.
- Zia, P., Leming, L., & Ahmad, S. (1991). *High Performance Concretes*, A State of the Art Report, Strategic Highway Research Program, SHRP-C/FR, DC, Washington, pp. 91-103.